2013

Numerical evaluation and analysis of the adhesion phenomena in thermal barrier coating systems through bio-mimicking plasma process

Naser Imran Hossain
Louisiana State University and Agricultural and Mechanical College

NUMERICAL EVALUATION AND ANALYSIS OF THE ADHESION PHENOMENA IN THERMAL BARRIER COATING SYSTEMS THROUGH BIO-MIMICKING PLASMA PROCESS

A Thesis

Submitted to the Graduate Faculty of the
Louisiana State University and
Agricultural and Mechanical College
in partial fulfillment of the
requirements for the degree of
Master of Science in Mechanical Engineering

in

The Department of Mechanical Engineering

by
Naser Imran Hossain
B.Sc. Bangladesh University of Engineering and Technology, 2011
August 2013

ACKNOWLEDGEMENTS

I acknowledge that part of the work presented in this dissertation is scheduled to be published in the proceedings of the ASME 2013 International Mechanical Engineering Congress & Exposition, IMECE2013, November 13-21, 2013, San Diego, California, USA

It pleasures me immensely to recount the people, the figures of flesh and blood, who have helped me through my endeavor, sometimes by just “being a friend or a dedicated ear that listened”, sometimes by helping me technically or philosophically to overcome the hurdles in my research. First and foremost, I would like to thank my major professor, Dr Muhammad A. Wahab, who has been almost like a father figure throughout my time in LSU, lending his valuable time and knowledge to my research work whenever it was possible. This research work would not have been possible without his patronage.

Next up, I’m highly obliged for PhD candidate Jiandong Liang (William) for his help with the experimental part of my thesis and for showing me the ropes around the lab at the first few months. I’m also grateful to my committee members, Dr Shengmin Guo and Dr Ayman M. Okeil for spearheading the research initiative. Dr Guo has been a very dedicated teacher and instructor who has constantly pushed me to understand and master the delicate science of Finite Element Analysis and also helped me with its implementation through the COMSOL FE interface.

I thank all my colleagues and friends, Washim, Jasem and others for guiding me through the annals of Louisiana State University and the Department of Mechanical Engineering, without their help my additional academics would have been a nightmare.

I express my final gratitude to my desist parents Sufia Sultana and Dr.A.A Mainul Hossain and my three sisters, Musarrat Sultana, Kishoare Sultana and Aeysha Nusrat Sultana who have inspired me through the tantrum of brainstorming, in those caffeine empowered nights of simulation run and through all the falls and rises I've gone through in USA reminding me what the science fiction writer Jim Butcher once said "When everything goes to hell, the people who stand by you without flinching - they are your family.".

This work was made possible by the NASA EPSCoR program (NASA/LEQSF(2009-12) Phase 3-03 , LSU Acct. No: 127-85-4117 & 127-85-4118) which supported the effort monetarily and philosophically.

TABLE OF CONTENTS

LIST OF TABLES

LIST OF FIGURES

LIST OF SYMBOLS AND ACRONYMS

η	Efficiency of the turbine
Gc	Adhesion energy coefficient
JKR	Johnson-Kendall-Roberts Theory
DMT	Derjagin-Muller-Toporov Theory
μ	Co-efficient of friction
ε	Depth of the potential well
$\Delta\gamma$ or W_{ad}	Work of adhesion
v	Poisson's ratio
E	Young's Modulus
P_c	Pull off force

ABSTRACT

Thermal Barrier Coatings or TBCs when abbreviated are an imperative part of the thermal protection system of expensive equipment and machinery in the automobile and aeronautics industry. They provide protection to expensive alloy materials upto a temperature of 2700° C without expensive metallurgical additions. Unfortunately, the problem of coating adhesion has plagued the TBC field for years, leading to catastrophic failures in critical TBC systems. Efforts to chemically improve bond strength has not been entirely successful, so the only other efficient way to do this would be some kind of mechanical interlocking that occurs at micro/nano scales. This research work deals with the improvement of adhesion in TBC systems by numerical simulation and bench-marking of micro-geometric surface features that has been synthesized or reproduced in laboratory environment through electrochemical operations. For this, several geometries that benefit mechanical interlocking, and consequently improvements in mechanical 'adhesion' in TBCs has been compared. To simulate the mechanical and thermal loading on the micro geometries and to observe their effect, the commercial finite element software COMSOL was used. An analogy was drawn between the biological, Van der Waals dry adhesion mechanism in Gecko feet and that in the top surface of the thermally grown oxide (TGO) layer in TBC whereas the 'mushroom head geometry' in the Gecko feet provides improved adhesion (as much as 10 folds) compared to other geometries (spatular head, spherical head, or plain triangular crevices). An affordable synthesis process, termed “Electrolytic Plasma Processing (EPP)" for recreating this specific geometry, is also proposed and its utility briefly entertained. The work ends with recommendations and suggestions for future works on this topic.

CHAPTER 1. INTRODUCTION

1.1 Motivations

It is often said that an engineer's job is never quite finished, because the motivation behind an engineer's work is to optimize a scientific observation or phenomenon so that it becomes economically and technoically viable. The more a person, as an engineer or as a technical visionary, achieves proximity to the goal that was envisioned when he/she started out with, the more successful the achievements can be christened as.

That is why to find its raison d'être in the world of scientific investigations and analytical studies these days, a research work must incorporate justification and support from as many branches of science as possible, and what better place to look for unanswered questions than the grand architect, mother nature herself?

Adhesion of protective coatings is a very real and fatal problem in the preservation of expensive mechanical equipments which is often exposed to harsh environmental and operating conditions. It is of the utmost importance in the current trend of research in these extreme conditions. When this research work was first given the impetus, very little had been investigated about the mystified parallelism that existed between mother tature and the manmade scientific processes in the fields of thermal protection and adhesion mechanisms. So at first it was very hard to see a semblance between the two. On one hand, adhesion was a very common and masterfully controlled phenomenon in nature; on the other hand scientists and engineers have struggled heavily on the topic of adhesion of coatings on mechanical systems without the usage of expensive metallurgical methods or corrosive chemical processes. To tie these two together in a systematic, mathematical study supported by proven hypothesis- literature reviews and numeric

models were needed. The underlying driver of the locomotion that has been generated by the mechanical properties of natural contact surfaces is the surprising range of surface mechanical properties such as adhesion, friction and compliance that are mostly attained by the design of near-surface architecture using generic material properties [Jagota, 2011]. This field is a vibrant new entry in adhesion mechanics. Thus the motivation behind this thesis is to provide both a qualitative and a quantitative summation from the point of view of scientists and engineers on the issues of adhesion, friction, and compliance in Thermal Barrier Coatings (TBC) systems and how bio-mimicry, or adaptations from mother nature can be harnessed to give an acceptable solution to one of the greatest problems facing the field of industrial thermal protection.

1.2 TBC, its Use and the Dilemma Within

Thermal barrier coatings (TBCs) are widely used in turbines, propulsion and power generation. They comprise of thermally insulating materials having sufficient thickness and durability that they can sustain gradients in the presence of adequate back-side cooling. Reducing the temperature of the metal substrate (the mechanical part in consideration) prolongs the life of the component, from environmental attack, creep, rupture or fatigue. In addition to this, by reducing the thermal gradients in the metal, the coating eliminates the driving force for thermal fatigue as well. All of these can contribute to the improvement of component durability, reduction in cooling air and thus improve system efficiency. As a result, TBCs has been extensively used in turbine engines due its high temperature applications in the ranges above 1000°C.

The efficiency, η of gas turbines or thermal engines is improved by increasing the turbine/engine inlet temperature. This can be achieved by using air cooling techniques combined with thermal barrier coating (TBC). A TBC combined with air cooling will reduce the metal

temperature and lead to higher inlet temperature to the gas turbine engine; then durability and efficiency of the engine will be improved.

The development of this technology leads to the synthesis and fabrication of thermal barrier coatings capable of providing thermal insulation of about 1650°C to 1700 °C. According to Pratt & Whitney, one of the three major jet engine manufacturers, TBCs were first introduced on the burner in the JT8D engines in 1963. This TBC consisted of zirconia stabilized with 22 wt% MgO (22 MSZ) [Bose et al., 1977]. Later on they incorporated other materials in order to achieve higher temperatures in the combustor chamber. In current systems, the 22MSZ was replaced by 7 % wt Yttrium partially stabilized Zirconium (7YSZ). This was due to the susceptibility to destabilization and low temperature capability of MSZ.

Thermal barrier coatings are routinely used in the engine hot sections. A typical TBC system has four primary constituents comprising of the TBC itself, an aluminum containing bond coat (BC) between substrate and TBC, a thermally grown oxide (TGO), predominantly alumina that forms between the TBC and the BC; and finally the super-alloy substrate (Jagota, 2011)

The major problem that has to be addressed with TBCs is the spalling from the substrate. The quality and further performance of TBC, likewise all thermally sprayed coatings or any other kind of coating, is strongly dependent on the adhesion between the coating and the substrate as well as the adhesion (or cohesion) between the metallic bond coat and the ceramic top coat layer. The debonding of the ceramic layer or of the bond coat layer will lead to the collapse of the overall thermal barrier system. Though several possible problems can occur in coating applications as residual stresses, local or net defects (like pores and cracks), one could say that a satisfactory adhesion is the first and intrinsic need for a good coating. The coating

adhesion is also dependent on the pair substrate-coating materials, substrate cleaning and blasting, coating application process, coating application parameters, and environmental conditions.

Thermal barrier coatings' characterization is an important technique used to provide a better understanding of the relationship between the microstructure and thermal properties of the plasma spray coatings. The thermal properties of the TBC depend strongly on the microstructure and porosity. The Atmospheric Plasma Spray (APS) technique used to make the coatings usually leads to lamellae microstructure comprised of the stacking of lamellae separated by imperfect interfaces. This microstructure enhances the thermal resistance. Therefore it is imperative to study and analyze the different failure and delamination phenomena in a thermal barrier coating system in order to understand or improve their lifecycle. The durability of a thermal barrier system is governed by a sequence of crack nucleation, propagation, and coalescence events that accumulate prior to a final failure by large scale buckling and spalling. The TBC is the main insulator, the BC provides the oxidation protection, and the alloy sustains the structural load. The TGO is a reaction product that mostly forms afterwards. The degradation of the TBC can occur in different layers, but the point of failure in most cases is the bond between the TBC and the BC where a thin layer of TGO is formed during the thermal operations. In order to understand the degradation of the TBC system better, we must look into aspects like the adhesion energy (G_c) of the different layers, its evolution during the cycling oxidation, and how the mechanics of adhesion is affected by factors.

1.3 Adhesion in Mother Nature and the Challenges to Mimic in Real-Life

Whenever we are faced with the overwhelming odds of finding solutions to an apparently helpless engineering conundrum, Mother Nature is always there to provide guidance. In case of

adhesion, there is no exception. Nature provides inspiration for enhanced control of adhesion through numerous examples ranging from the “Geckos” to “Jumping Spiders”. The primary strategy in these examples is the incorporation of patterns, specifically high-aspect ratio topographic features to ingeniously *maximize adhesion forces while maintaining ease of release.* Recently, considerable research efforts have been devoted towards the understanding, development, and optimization of a synthetic analogues to these examples in nature [Chan, 2007].

Over the millennia, it has not occurred to human designers and engineers that a material could be designed to meet the needs of locomotion and at the same time, of adhesion. By locomotion what is meant is the need to move the very animal whose appendages form the moving mechanism. From an engineering point of view it might mean the need to pick up and place an object. By adhesion, we typically mean the ability to adhere, supportless to a surface, i.e., with sufficient strength or energy. Often, it is implied that the requirement is for one-time adhesion; ease of removal is not an issue. The joint purposes of strong adhesion and fast, energy-efficient locomotion, impose seemingly contradictory requirements on the material at the contacting surfaces of the organ. In nature, the material must additionally meet restrictions such as, the ability to avoid soiling by particles, to be self-cleaning, that the adhesion mechanism not be surface-specific, and to use natural materials that can be synthesized easily. Faced with these challenges, animals such as lizards and insects have evolved a class of interfaces that share the common motif of hierarchical fibrillar design [Gorb et al., 2009, 2011]. Typically, the hierarchy has features that range in scale from millimeters to nanometers. Chan shows such a hierarchy in the case of the Gecko [Chan et al., 2007]. Natural fibrils, termed setae, typically end with a thin-plate-like contact surface (shown in Figure 1-1). Broadly, there are two classes: mechanically

independent fibrils terminated by a flattened structure, dubbed the ‘mushroom’ for its likeness to the familiar shape of the well-known member of the fungi family, and continuous films.

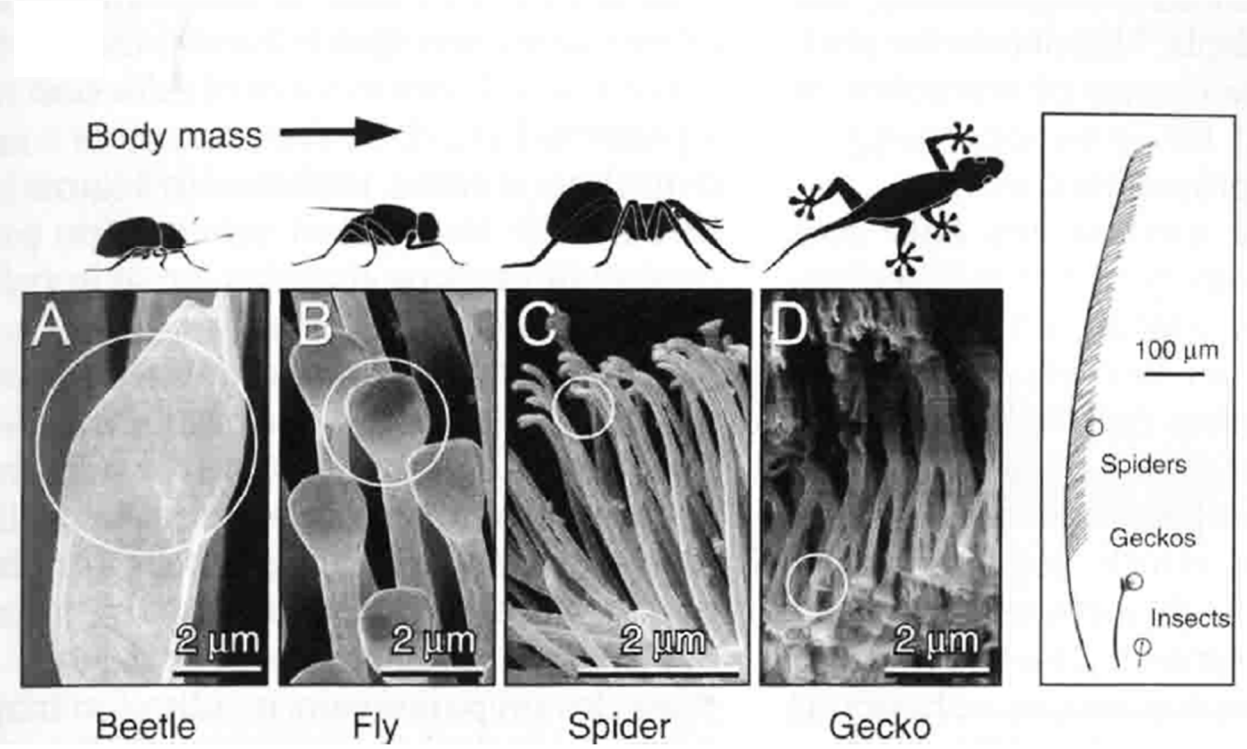

Figure 1-1 : Hierarchical arrangement of fibrillar structure in animals in the nature [Gorb , 2009]

In lizards, the material itself is keratinous, a stiff glassy polymer, and the contact surfaces appear to have no particular or specific adhesive characteristics. In insects, the material is a chitin composite, likewise a stiff glassy polymer. The wonder of these materials is that with this modest collection of features the structure is capable of adhesion to a remarkable variety of surfaces, and is re-usable, anisotropic, self-cleaning, flaw-tolerant, and compliant at the contact interface.

Given their reliance on non-specific inter-surface interactions, desired functionality resides essentially in the basic (generic) materials properties and, most importantly, in the

fibrillar architecture and its contact and detachment mechanics. For this reason, recently there has been considerable interest both in studying these structures and in developing and understanding the surface mechanical properties of synthetic mimetic. Materials scientists and engineers have not really captured this sort of functionality previously. Generally, if one desires repeated attachment/detachment, one looks to fasteners rather than adhesives. Perhaps the classes of materials that come close are pressure-sensitive adhesives (PSAs) , which work on a variety of surfaces and have some limited re-usability as in the Post- It pads, and hook-loop fasteners, such as the bio-mimetic Velcro, that require a mating architecture. It seems natural to designate as fastener any attachment mechanism that relies on structures we would all recognize as the macro-scale—say, with characteristic length scale of a few hundred microns or larger. When the attachment is due to bonds or intermolecular interactions between the surfaces at the molecular length scale, the term adhesive appears.

1.4 Thesis Outline

Understanding and manipulating surface interaction in forces in microscale devices has become an increasingly important design concept for a variety of applications. Examples include surface engineering of MEMS components to alleviate stiction (the static friction that needs to be overcome to enable relative motion of stationary objects in contact) problems [Sylves et al., 2008]. In this thesis work, one such proposition to improve the adhesion properties in TBC devices is given, discussed, fabricated, and finally numerically and analytically supported.

Beyond the initial literature review, in order to address the problem, this thesis work is divided into three main sections. These three parts address three different sides of the process. The first part comprises of the technology and fabrication methods behind the current field of thermal protection using thermal barrier coatings. To do that, the methodology, modeling

methods and measurement techniques are discussed in Chapter 3. The proposed surface modification technique known as “Electrolytic Plasma Processing” is introduced for the first time in the next section in Chapter 4. This process known as EPP is a homebrewed method of surface treatment developed as a part of a NASA/EPSCoR grant at Louisiana State University that partially funded the research. The next chapter, chapter is devoted to the comparison of the many ways of TBC fabrication with EPP and compared on the basis of adhesion strengths attained.

The third and final part of the thesis is devoted to providing a solution to the adhesion problem by a policy of “leading by example from nature.” In Chapter-5 an analogy is drawn between the micro-texture of the surface that can be produced by EPP and that of the mushroom head geometry seen on Gecko setae’s. The improvement proposed is further evaluated by two well-known finite element models (JKR and DMT models); and their validation carried out with state of the art multiphysics FEA software, COMSOL. Different experimentally attainable geometric features are compared and their feasibility in terms of adhesion justified. Subsequent modifications are done to the model with modeling software (SolidWorks) and synched with the finite element analysis window via a feature called ‘live link’ where any changes made in a CAD window is automatically reflected in the FEA engine. The analytical and experimental results are finally compared in Chapter-6 that sums them up to give a theoretical and numerical analysis that ties all the loose ends together. The thesis work ends with recommendations on future works and limitations of the approach adopted

CHAPTER 2. LITERATURE REVIEW

2.1 History of Thermal Barrier Coatings

Thermal Barrier Coating or TBC for short is a branch of emerging technology in the aeronautical and turbine industry (Figure 2-1). It is also used in many of today's high performance automobiles and concept cars, helicopter engines, and exhaust manifolds of power equipment to protect expensive alloy parts from thermal failures.

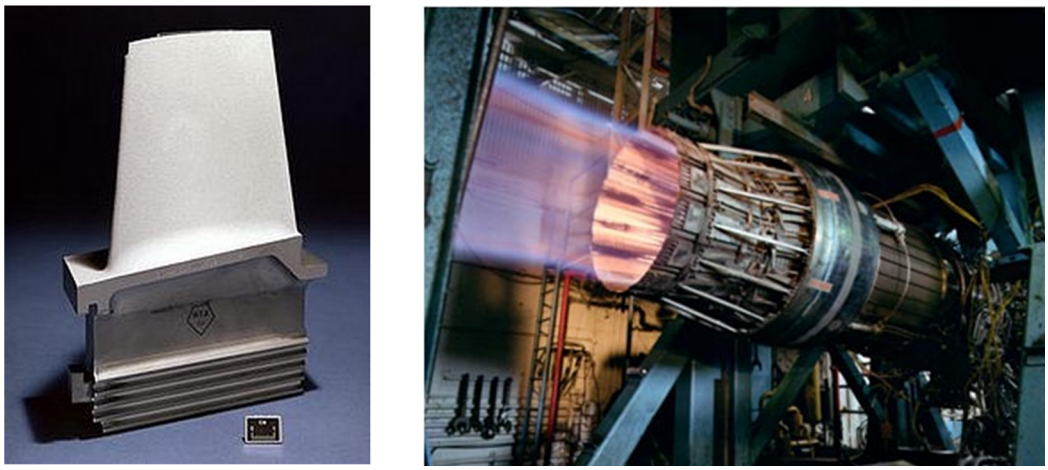

Figure 2-1: Application of Thermal Barrier Coating-Protection of super alloys [John Hopkins University, Microscale Experimental Techniques for Thermal Barrier Coating Development, 2002]

Thermal Barrier Coatings (TBC) surged as a method to reduce high temperatures on thermally loaded combustion process components and increase efficiency linked to heat transfer processes by combining properties from both super alloys and ceramic insulators. The first work on TBC was developed back in 1942 were Harrison and More developed the first Aero Ceramic Coating, the NBS Frit Enamel coating which consisted on a blend of minerals smelted in much the same manner as common glass. During this process (known as "fritting"), the red-hot, molten mixture is poured from a smelter and quenched between water-cooled rollers. This quick-cooled ribbon of glass is then shattered forming a particulate known as "frit" and then apply to metal

using either a wet or dry method and fired at very high temperatures - generally ranging from 1100 to 1600 degrees Fahrenheit [Gupta et al., 2007; Kim et al., 2010]. However, durability questions followed Al -ceramic coatings for decades partly due to popular images of enameled kitchenware and possibly from negatives results on engines tested during the following two decades.

After overcoming durability problems as a safety feature, new TBC technologies were developed, such as the ROKIDE ^{TM} which was efficiently tested on XLR99 rocket nozzle on the X-15 in 1960 since Rokide's insulating properties prevented the liquid ammonia circulating through the nozzle and cooling structure to boiled and oxidation of tube assembly. This process mainly involves ceramic rods melted, atomized and sprayed at high velocity on the surface to be protected; moreover, forming an extremely hard, flexible and chemically inert coating that can be used as sprayed or finish-ground to a specified tolerance. Rokide coating is especially suited and nowadays widely used for applications requiring extreme dry abrasion wear resistance. Industries such as paper, petrochemical, oil, wire, and aviation/aerospace benefit tremendously from Rokide ceramic coatings [Kim et al., 2010].

In addition, graded Rokide were tested and compared to conventional processed Rokide, finding significant results. Grading improve coating adhesion which resulted on higher durability and insulating qualities [Kang et al., 2003].

In the 60's and early 70's Dr. Sal Grisaffe [Grisaffe, 1962] performed basic research on Materials-Oriented Thermal Sprayed sponsored by NASA/NACA and founded the first coating's group. Among his work can be found the " Simplified Guide to Thermal-Spray Coatings" and "Hydrogen Plasma Test of Dome Insulating Coating System for The Nuclear Rocket Thrust

Chamber"; However, Grisaffe's major accomplishment was the used of Alumina, Zirconia (possibly Yttria stabilized) and Hafnia coatings which open a wide door of opportunities in the development of Modern Thermal Spray Coatings [Heimann, 1998].

Eventually, when the TBC of Zirconia -12% Yttria on NiCrAIY survived J-75 engine test in mid-70, it was first demonstrated that the blade of TBC's were feasible and could be used on major aeronautic industries (Figure 2-2).

Key endeavors that lead to this accomplishment:

- The use of Yttria as Zirconia stabilizer.
- The use MCrAIY as a type of bond coat.
- The demonstration that a graded region is not required.

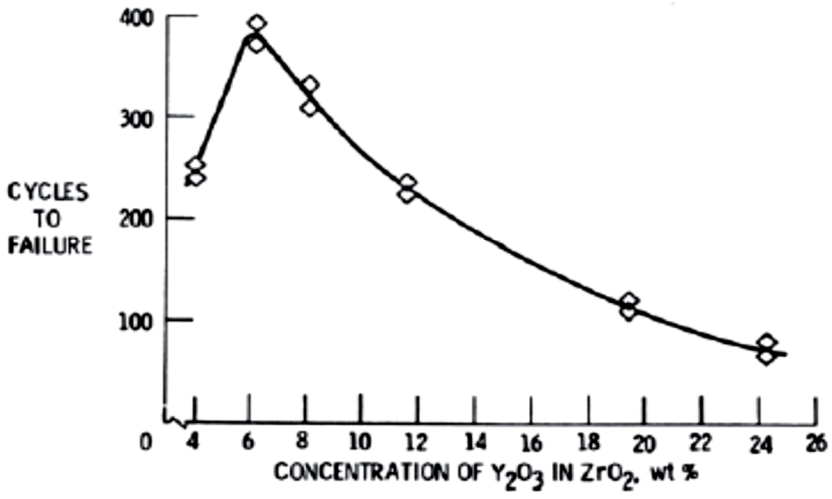

Figure 2-2 : Effects of Compositional Changes on the Performance of a Thermal Barrier Coating [Heimann, 1998]

S. Stecura [Stecura, 1980] reported optimum Zirconia- Yttria TBC composition when conducting furnace (Figure 2-3), natural gas torch and burner rig test in 1978. Stecura's later work reported 2X life for Ytteria-Stabilized Zirconia on a Yb-Containing bond coat.

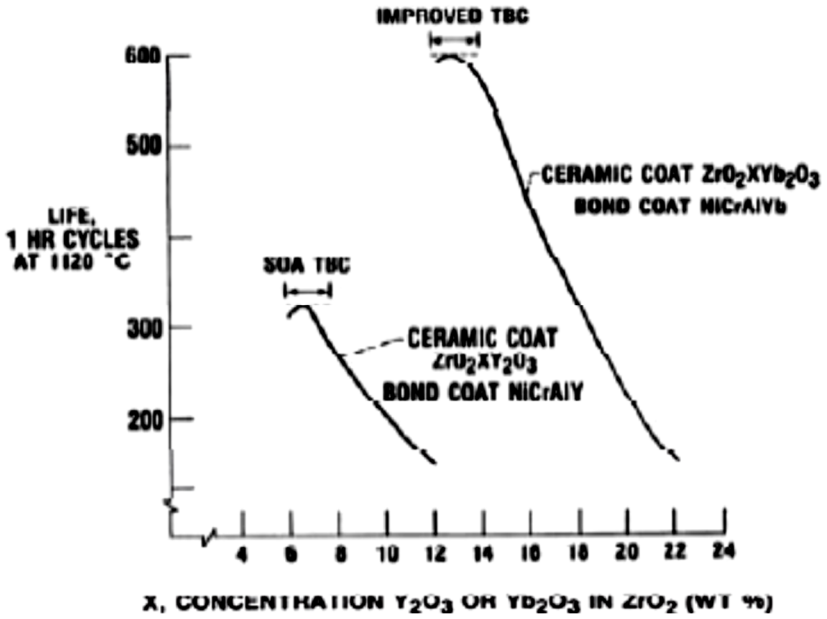

Figure 2-3 : New ZrO2 Plasma Sprayed Coating Concentration. [Heimann, 1998]

In addition, Stecura also recommended bond coats with lower CTE's and his eventual favorite MCrAlY was Ni-35Cr-6Al-Yb or Y which is a more ductile bond coat due to low aluminum and lower expansion coefficient.

Arguments persisted in early 80's over the role of heat flux vs. the thermal expansion mismatch and environmental effects linked to TBC process; in 1980's some believed that failure occurred due to residual stress resulting from heating and cooling. However, R. A. Miller and C. E. Lowell [S.bose, 1997] research showed in 1982 that: Cracks link up at the interface prior to visible surface cracking or spalling, due primarily to thermal expansion mismatch between ceramic/metal.

A few cycles after the cracks link up to form a delaminated region (visible as hot-spot on heating), the rapidly heated unattached portion of the coating spalls on heating. Failure is influenced by bond coat plasticity and oxidation at the irregular bond coat/ceramic interface.

Also, coating life was time and cycle dependent.

Paul Siemers of General Electric CR&D was another researcher to recognize the importance of bond coat oxidation and plasticity who states that “the durability of thermal barrier coatings is limited by degradation of adhesion by environmental interactions rather than by mechanical stress per se.” [Gupta et al., 2007; Kim et al., 2010].

Besides Miller’s research, NASA, Pratt & Whitney (P&W), and GE developed two major projects [P.bose, 1997], both contracts involved analytical assessment of the value of TBCs and its relation to energy efficient. Pratt & Whitney used Zirconia-Yttria TBC to fix a Vane platform endurance issue; moreover, increasing service life and eliminating distress formed on the Vane; P&W shared these results with NASA leading to TBC task in HOST Life Prediction Program which identified the failures modes on TBCs and subdivided them in :

- Mechanical (major mode).
- Oxidation (major mode). Hot Corrosion (minor mode).
- Erosion (minor mode).
- F/BMOD not identified situations in service (minor mode).

In 1989, EB-PVD (electron-beam physical-vapor deposition) TBCs were introduced for the first time onto turbines blades in revenue service, on South African Airways B747; however, results were not as exceptional as anticipated since the high altitude airport and the high mean

ambient temperature resulted in unexpected airfoil distress, but still results were comparatively a lot better than No-TBC treated as shown in Fig 2.4.

Figure 2-4 : Comparison between non thermal coated turbine blade and a thermal coated. [Théry, 2007]

However, TBCs properties continued to improve when EB-PVD (electron-beam physical-vapor deposition) was introduced for more demanding rotating, as well as stationary turbine components. The superior performance of EB-PVD applied TBCs compared to plasma sprayed TBC is due to their columnar microstructure (Figure 2-5) which exhibits very high levels of stress compliance. Where, it is clearly noticed that spallation and oxidation seem diminished.

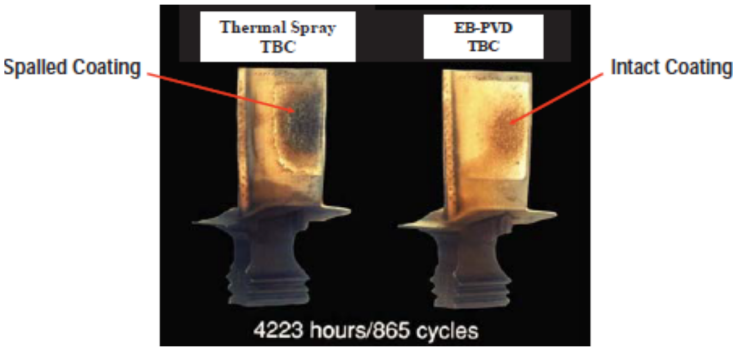

Figure 2-5 : Spallation behavior comparison between thermal sprayed and EB-PVD thermal barrier coatings

In conclusion, enhancing combustion engines efficiency is a major issue in mechanical engineering, where research on TBCs has to date developed new strategies to ameliorate it. In this research, many efforts have focused lately on understanding adhesion properties since it is has been demonstrated that most of the failures occur on the substrate and bond coat interphase; and that satisfactory adhesion is the first intrinsic need for a high quality coating. Moreover, NASA's efforts have redirected their scope to high speed research and aimed at Supersonic missions and high force, frequency, and capability applications.

2.2 Technology Behind Thermal Barrier Coatings

2.2.1 Thermal Barrier Coating Composition

The four layers [Figure 2-6] in the current TBC system are made of different materials with specific properties and functions. Below is a brief description of each layer and its common composition [Kang et al., 2003]

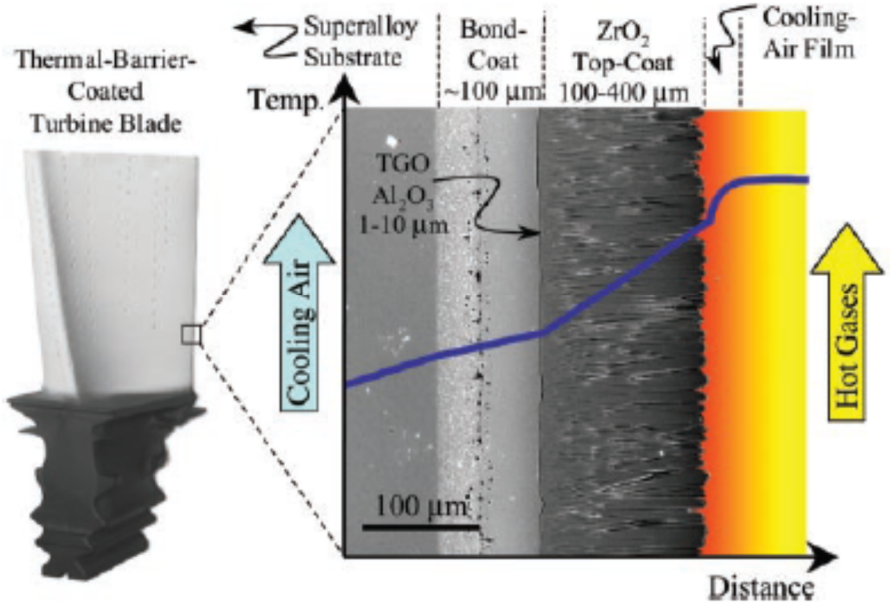

Figure 2-6 : Anatomy of Thermal Barrier Coating [Gupta, 2007]

Substrate**:** Consisting basically in a super-alloy nickel or cobalt-based structure, substrate layer contains as many as 5 to 12 additional elements to enhance high temperature properties such as strength, ductility, oxidation resistance, hot-corrosion resistance, and castability; however, such elements may diffuse between the super-alloy and the bond coat since constantly changing properties are experienced during operation. Therefore, TBCs must be considered an engineering system whose properties change with time and cycles during service.

Bond-Coat: The Bond-Coat having an average thickness of 75 µm to 150 µm, the bond coat is an oxidation resistant metallic layer which is typically made of a NiCrAIY or NiCoCrAIY alloy and is applied by using plasma spray or the electron-beam physical vapor deposition methods. However, other types of bond coats can be found, and made of aluminide of Ni and Pt and are deposited by electroplating in conjunction with diffusion-aluminizing or chemical-vapor deposition.

Thermally Grown Oxide (TGO): When operating over 700 ^{0}C an inevitable bond coat oxidation layer starts forming between the bond coat and the ceramic top layer, called thermally grown oxide layer (TGO) which has a thickness within the 1 µm to 10 µm. even though the formation of the TGO can be avoided, the ideal TGO is ensure to form as an α-Al_20_3 and that its growth is slow, uniform, and defect-free. Since TGO has a low oxygen ionic diffusivity, it can retard further bond-coat oxidation [Kim et al., 2010].

Ceramic Top-Coat: Made of Y_2O_3- stabilized ZrO_2, this layer provides the thermal insulation. It has the lowest thermal conductivity at elevated temperatures of all ceramics (2.3 $W.m^{-1}.K^{-1}$ at 1000 ^{o}C) because of its high concentration of point defects, which scatter heat-conducting phonons. The YSZ has a high thermal expansion coefficient which helps to reduce

stress form as consequence from the thermal expansion mismatch between the ceramic coat and the underlying metal. YSZ has relatively low density, which is important for parasitic-weight consideration in rotating engines and also has a hardness of 14 GPa (or 1428 HV) which makes it resistant to erosion and body impact.

The usage of YSZ as top coat refers to the following properties shown in Table 2-1 :

Table 2-1 : Mechanical & Thermal Properties of some TBC's & Ceramics

Mechanical & Thermal Properties	Units	Al_2O_3 (Coors AD-99.5)	MSZ (3 wt.% MgO)	YSZ (~8 wt.% Y_2O_3)	YSZ (>12 wt.% Y_2O_3)
Density	g/cm^3	3.89	5.75	6.02	5.6
Elastic Mod.	GPa	372	200	200	173
Compressive Strength	MPa	2620	1750	N/A	N/A
Thermal Conductivity	W/m-°K	35.6	2.2	2.2	2.2
CTE	$10^{-6}/°C$	8.2	10.1	10.3	10.5
Specific Heat	J/kg-°K	880	486		
Thermal Shock Resistance	°C	200	350	350	150
Max. Use Temp.	°C	1750	500	2400	2400

In addition, YSZ has a high melting point (around 2700 ^oC) which is its major advantage over other materials considered for possible applications.

2.2.2 Deposition Methods of TBCs

Ceramic Coatings: Although there are various methods for depositing ceramic coatings, the two most important and used are the Air-Plasma Sprayed (APS) and Electron-Beam Physical-Vapor Deposition (EB-PVD).

Air-Plasma Sprayed (APS): Plasma spray deposition is one of the most important technologies available for producing the high–performance surfaces required by modern industry (as shown in Figure 2-7). Over the past two decades, there have been significant advances in the understanding of plasma physics and in the development of spraying equipment and techniques. This has enabled a range of materials including metals, alloys and ceramics to be plasma sprayed on to a great variety of substrate types and geometries. During this period, the uniquely aggressive environment within the gas turbine engine has provided not only some of the greatest challenges to plasma spraying technology, but also some of its most successful applications.

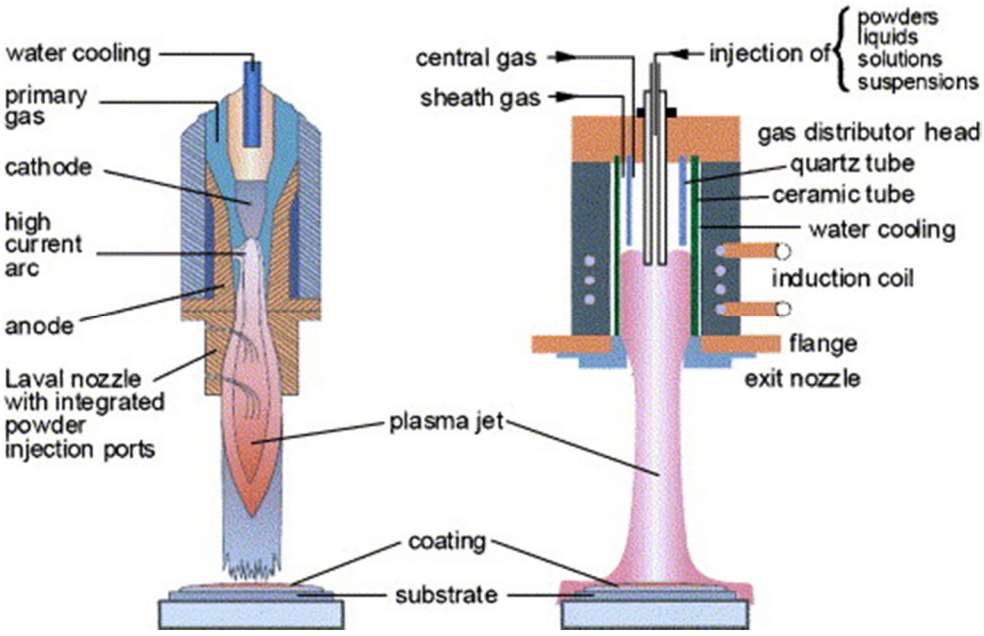

Figure 2-7 : Schematic diagram of DC and RF plasma spraying apparatus [Lima, 2007]

Versatility and low production cost make APS- TBCs attractive commercially; however, because of the proliferation of microstructural defects parallel to the interface and the roughness of the interface, APS TBCs generally have shorter thermal cycling lives than EB-PVD TBCs. Therefore, APS TBCs are suitable for less exacting applications.

Electron Beam Physical Vapor Deposited (EB-PVD): Besides APS, another commonly used deposition process for the ceramic top coat is the EB-PVD process (Figure 2-8); Electron Beam Physical Vapor Deposition or EB-PVD is a form of physical vapor deposition in which a target anode is bombarded with an electron beam given off by a charged tungsten filament under high vacuum. The electron beam causes atoms from the target to transform into the gaseous phase. These atoms then precipitate into solid form, coating everything in the vacuum chamber with a thin layer of the anode material.

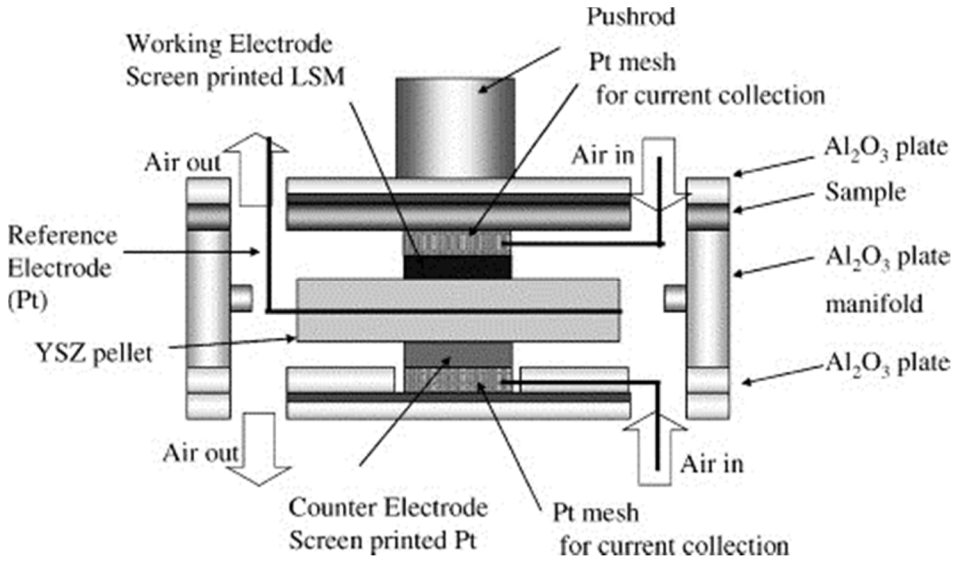

Figure 2-8 : Schematic diagram of Electron Beam Physical Vapor Deposition apparatus [Miller, 1989]

In contrast to the APS case, here the bond –coat surface can be smooth before deposition. Typically, EB-PVD top coat has the following microstructural features: a thin region of Polycrystalline YSZ with equiaxed grains (size 0.5 to 1 μm) at and near the metal/ceramic interface. Second, columnar YSZ grains (2 to 10 μm diameter) growing out of the equiaxed-grain region to the top-coat surface. Third, it has nanometer-scale porosity within the columnar grains, and channels separating the columnar grains, normal to the metal/ceramic interface [Chen et al., 1999].

These disconnected columns impart "strain tolerance" to the TBC since thermal expansion mismatch stresses can be accommodated when the columns separate at high temperature. The porosity and the cracks help reduce the thermal conductivity, but to a lesser extent than APS TBCs because the channels are parallel to the direction of heat flow. In addition, EB-PVD TBCs costs are considerable higher compare to APS; however, such downside can be afforded when comparing their durability which makes them suitable for the most severe applications, such as turbine blades and vanes in aircraft engines.

Bond Coat: The bond coat is applied using the same method explained before for the ceramic layer; however, more recently, High Velocity Oxygen Fuel (HOVF) spraying has been used as an alternative method due to its low cost and high quality deposits which present oxidation rates at high temperature at the same level of similar VPS (Vacuum Plasma Sprayed) coatings.

High Velocity Oxygen Fuel (HVOF): First developed during the 1980s, HOVF spraying consists in a mixture of gaseous or liquid fuel and oxygen is fed into a combustion chamber and then ignited and combusted continuously (Figure 2-9). The resultant hot gas comes out through a

converging-diverging nozzle and travels through a straight section; afterward, a powder feed stock is injected into the gas stream and directed towards the surface to be coated; the powder partially melts, and deposits on the substrate; resulting in a low porosity and high bond strength coat.

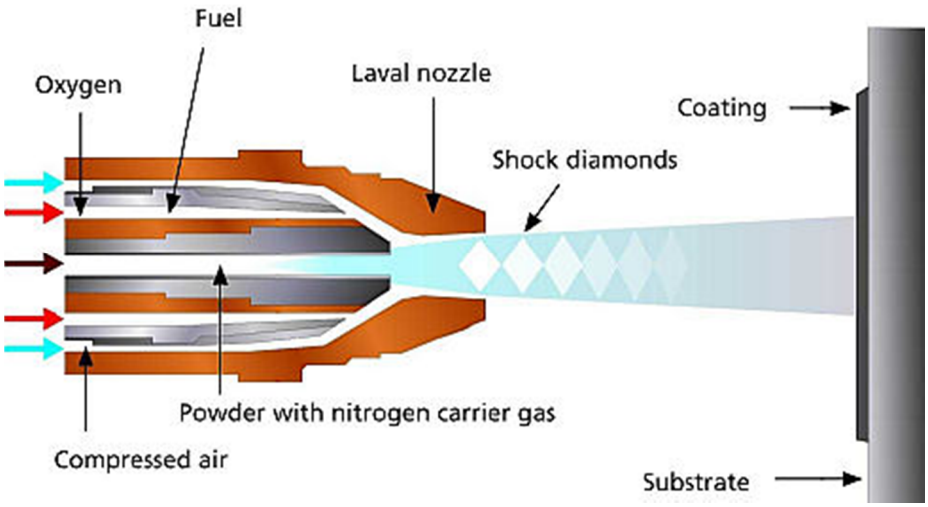

Figure 2-9 : Schematic diagram of High Velocity Oxygen Fuel Deposition apparatus [Hass, 2000]

HVOF coatings are very dense, strong, and show low residual tensile stress or in some cases compressive stress, which enable very much thicker coatings to be applied than previously possible with the other processes.

2.3 Applications of Thermal Barrier Coatings

2.3.1 Thermal Barrier Coatings for Aircraft Turbines

This field stands where the majority of research has focused on since TBCs where first developed. The greatest efficiency benefits of TBCs in an aircraft engine come from their use on the stator vanes and the turbine blades which are the hottest components in the engines. Prior conditions that must be taken into account when designing TBCs are high temperature oxidizing gases and thermal cycling.

According to Miller [Miller et al, 1989, 2007] the current best bond coats on aircraft technologies, developed through extensive investigation, are MCrAlYs compositions significantly better in terms of top coat life than NiCrAlY compositions used for overlay coatings. However, the oxidation resistance of these bond coatings is not as good as that provided by overlay coatings; thus, additional factors possibly involving bond coat yield strength, modulus, and thermal expansion must affect life. This is an area currently under investigation at NASA.

2.3.2 Thermal Barrier Coatings for Diesel Engines (Low Heat Rejection (LHR) Engine)

Low Heat Rejection Engines (LHR) is one of these ground breaking designs, engine that has been conceived basically to improve fuel economy by eliminating the conventional cooling system and converting part of the increased exhaust energy into shaft work using the turbocharged system [Barnes, 2012]. The effect of insolation on LHR engines performance can be described as follow:

Volumetric Efficiency (VE): The VE is an indication of the breathing ability of the engine which basically depends on operating conditions. Reducing heat rejection with the addition of ceramic insulation causes an increase in the temperature of the combustion chamber walls on an LHR engine; therefore, the volumetric efficiency should drop, as the hotter walls and residual gas decrease the density of the inducted air. To prevent VE from dropping out a turbocharging system can be adapted in order to effectively use the exhaust gas energy.

Thermal Efficiency (TE): TE is the true indication of the efficiency with which the chemical energy input in the form of fuel is converted into useful work. Improvement in engine

TE by reduction of in-cylinder heat transfer is the key objective of LHR engine research. Insulation effects on TE have divided into two different approaches; one side reported improvements in TE on LHR engines based on the heat transfer reduction and lower flux in an insulated cylinder. In the other hand, claims that TE decreases as a result of the increase in the convective heat transfer coefficient, higher heat flux and deteriorated combustion. Fuel Consumption: analysis on fuel consumption in LHR engine have reported an improvement ranging 2 to 12 % attributed to insulation of in-cylinder and reduced friction due to increased wall temperature.

A significant number of theoretical analysis of LHR engines state that an increase of insulation properties directly resulted in an improvement in TE; however, the combustion model used in simulations cannot sufficiently simulate a stratified combustion process of a diesel engine. Furthermore, the use of reduced heat rejection in diesel engines is least useful in naturally aspirated engines, and more useful in turbo-charged engines; therefore, in order to obtain better performance it becomes necessary to match the engine with a turbo charger. The addition of these new elements implies higher costs of production, costs that are being evaluated to assure that fuel consumption and efficiency are higher enough to apply this technology.

2.4 Electrolytic Plasma Processing (EPP)-A Novel Surface Modification Technique

2.4.1 Plasma Phenomenology

By definition, plasma is a gas, in which a certain portion of its particles are ionized. The presence of the charge carriers makes plasma electrically conductive so that it has properties unlike those of solids, liquid, or gases; and is considered to be an almost unique state of matter. Like gases, plasma does not have a distinct shape but under influence of a magnetic field will

form filament like structures. Although plasma contains ions and electrons in about equal numbers, if present very close to an electrode, the ions specie will dominate and plasma will be characterized by its ion content. Temperature controls the degree of plasma ionization, and is a measure of the thermal kinetic energy per particle. In particular, plasma ionization is determined by the electron temperature relative to the ionization energy. Under an applied potential, the particles are accelerated and the plasma temperature will increase, and this property is taken advantage of in plasma processing techniques, weather it takes place in vacuum or aqueous electrolytes (atmospheric plasma).

Electrolytic Plasma Processing (EPP) is an emerging technology for surface modification. The EPP process is based on electrolysis of an aqueous electrolyte by application of an electrical potential between the work-piece and counter-electrode, and the production of plasma (micro-arc discharges on the workpiece surface). The plasma micro-arcs provide a heat source for surface modification via localized surface melting and rapid cooling (cleaning process) and, if desirable, enhance ion deposition on a given substrate [Cionea, 2010] . Being a hybrid process of conventional electrolysis and atmospheric plasma process, it has been a field of research for many years. First works on this area were performed by Kellogg, and more recently by Gupta and Tenhundfeld [Gupta et al., 2007] who introduce its application linked and benefits for surface engineering.

In 1981, Sengupta [Sengupta et al., 1991] conducted work on the high voltages required for a normal electrolysis to switch over to a phenomenon called contact glow discharge electrolysis (CGDE). He also looked into the anode-cathode relative distance, electrolyte influence and polarity of the electrode on the growth of a stable vapor envelope during normal electrolysis. Later on, the same author published an analysis of the chemical products obtained at

the anode during CGDE in inert electrolytes at various applied voltages and electrolyte compositions and found that the main products, H_2 and O_2 from the dissociation of water molecules are the result of plasma around the anode when the glow discharge is maintained constant (Figure 2-10) .

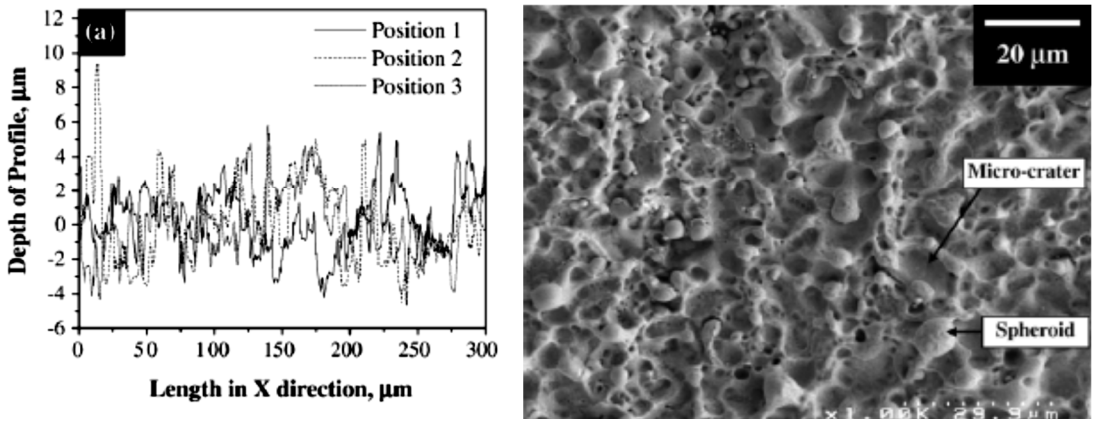

Figure 2-10 : Micro roughness profile- (shown left) and SEM micrograph showing typical surface morphology (Right) [Liang, 2012]

A comparative study of the chemical yields of anodic and cathodic CGDE indicates that the breakup of water molecules occurs entirely in the plasma during cathodic CGDE, but primarily in the liquid (electrolyzed water) and partly in the plasma during the anodic phenomenon. It can be observed that different phenomena occur depending on the evolution of the discharge, anodic or cathodic.

2.4.2 Application and Utility

Electrolytic Plasma Processing is a novel technique that has shown great promise for its application on commercial scale for cleaning and coating metal surface. Surface morphology after treated with EPP is characterized by the presence of two unique features, micro-craters and spheroids which make them and excellent site for mechanical interlocking, and at the same time

exhibits an interesting micro roughness depth profile; therefore, a combination of unique surface morphology and micro roughness makes the EPP- treated surface favorable for adhesion to lubricants, paints, coatings, etc. [Liang et al., 2012].

In addition, EPP cleaned steel has shown resistance to general corrosion from days to weeks in an enclosed environment; such improvement is attributed to the formation of a layer of pure α-iron after the application. The Nano-sized grain structure of the EPT-treated surface layer may also contribute to the improved of corrosion resistance. This particularity has also been reported for nano-crystaline -304 stainless steel when compared to conventional-304 stainless steel.

EPP coatings exhibit excellent bonding with substrate with an adhesion strength higher than 70 MPa, this benefit is more than likely due to the diffusion bonding formed with the substrate, due to high localized temperatures; moreover, a deposition rate with Zn coating, as high as 1µm/s, has been achieved by EPP which is comparatively higher than other deposition processes.

2.4.3 Development of the EPP process

Several studies have been conducted on plasma electrolysis, on issues regarding the basic science [Yerokhin et al., 1999] and practical applications [Sengupta,1991]. All such studies have in common, the observation that for a certain voltage applied between the two electrodes, and a significant deviation from the Faraday‘s normal electrolytic regime occurs. The conclusion of the studies was that several factors may influence the formation and evolution of the continuous plasma surrounding the electrodes: applied potential, temperature and properties of the electrolyte medium, flow dynamics, electrodes material and geometry.

Others, such as applied current (DC or pulse), processing time or gap between electrodes are also presently investigated. Figure 2-11 shows a simplified representation of the electrochemical processes taking place at the electrodes in an aqueous solution during Plasma Electrolysis.

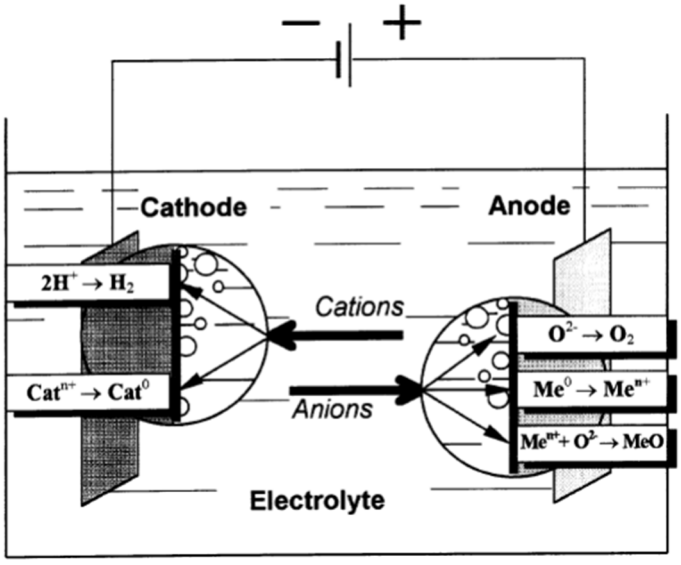

Figure 2-11 : Electrode processes in the electrolysis of aqueous solutions [Cionea, 2010]

The activity of gaseous oxygen and hydrogen as byproducts of water electrolysis is of particular importance. At the anode, made of metals which exhibit anodizing behavior (Al, Mg, Ti), the oxygen promotes oxide formation. At the metallic cathode, atomic hydrogen assists in the formation of plasma envelope while the cations from electrolyte are accelerated toward the electrode for coating formation.

A review on plasma electrolysis published in 1999 by Yerokhin et al. [Yerokhin, 1999] summarized most of the known fundamental knowledge on the process applied to surface engineering, from the point of view of the anodic process. The study left open the extent of fields of applications, which is only at its incipient stage. While PEO (Plasma Electrolysis Oxidation) has become a well-developed technology over the past 10 years [Meletis et al.,

2002], applications for the cathodic process (referred in this work from now on as EPP) were only starting to emerge in the early 2000. Among the first to be mentioned are: plasma electrolytic nitro-carburizing treatments for stainless steel and cleaning and coating of metallic surfaces (most common used on steel surfaces) Recent works [Liang et al., 2012] were published on the application of pulsed DC current during EPP processing. Initially, the pulse source was considered for the anodic process and only recently 4340 steel was cleaned [Cionea, 2010] and Zn-Ni-Cd coatings were deposited with the cathodic process. The applied pulse current theoretically allows more control of discharges used in various surface treatments and coatings. Also, thermal impact from the treatment is virtually insignificant on the surface hardness of steel compared to the DC approach and cleaning of the surface is more effective with increased duty cycle and frequency [Liang et al., 2012]. More work is needed to evaluate the influence of pulse potential on the microstructure and mechanical properties of deposited coatings.

2.5 Bio-Adhesion and Bio-Mimicry

2.5.1 Phenomenology

Bionics and Bio-Mimicry has increasingly attracted attention in recent years. Some animals, such as beetles, flies, spiders, geckos, could move freely and rapidly on smooth vertical surfaces and hang from a ceiling [Patano et al., 2011]. Inspired by this phenomenon, scientists have extensively studied the adhesion mechanisms of these animals and insects. As the largest of these animals, geckos were paid more attention to (Figure 2-12). Many studies showed that Geckos' extraordinary adhesive capability can be ramified into two parts [Varenberg et al., 2006]: an adaptation of a hierarchical structure [Varenberg et al., 2006; Chen et al., 2012] of

their toe's to a natural, rough surface, and the mechanics of adhesion of a single contact[Li et al., 2010] with surfaces.

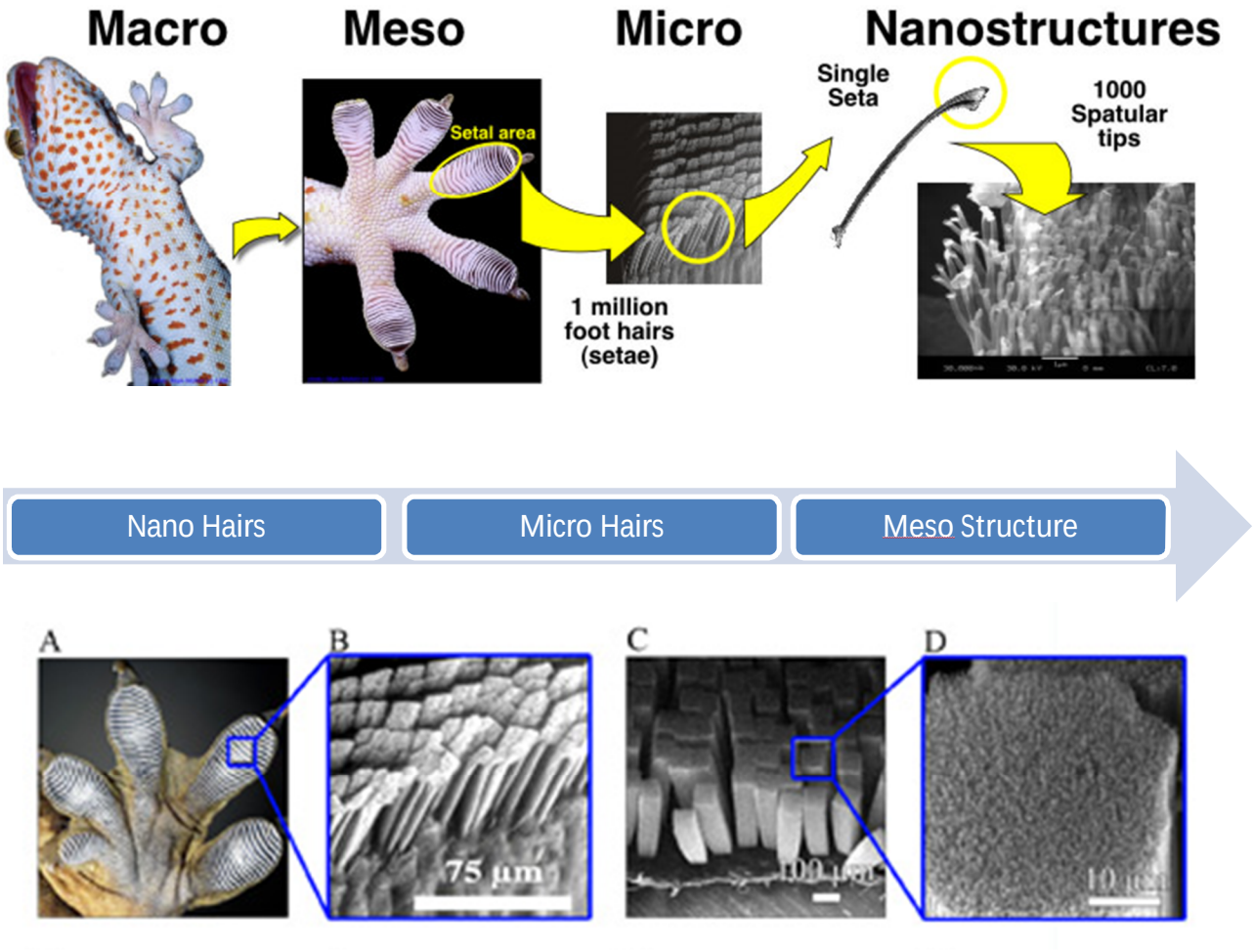

Figure 2-12 : Contact splitting and micro/nano geometric features responsible for adhesion [UC Berkeley, Poly-Pedal Lab, 2012]

As showed in Fig.2-12, the hierarchical structure contains a series of regular arrangements, almost identically orientated lamellae. General electronic microscopy has shown that the lamella is composed of uniform hair-like fibers (setae) which branch at the tips into finer fibrillae (spatulae). These structures allow for intimate contact between the spatulae and surfaces to obtain high adhesion (via the van der Waals force [Autumn et al., 2002]) on almost any

surfaces. The adhesive force of a single gecko seta was measured by Autumn [Autumn et al., 2002]. Their experimental results showed that a single seta can make a maximum adhesive force of nearly 20 μN and a maximum shear adhesive force equivalent of 200 μN . This means that a contact area of 1 cm^2 could produce a normal adhesive force of 10 N and a shear adhesive force of 100 N, on the basis of a Tokay gecko (Gekko gecko) pedal parameters which has about 5000 setae per mm^2 [Li et al., 2010]. Zhang measured an adhesive force of about 10 nN of a single gecko spatula [Zhang et al., 2010].

2.5.2 Underlying Mechanism

The adhesion of solid elastic bodies has been extensively studied in the past. Two general models of the contact behavior have been proposed: the Derjagin-Muller-Toporov or DMT approach [DMT, 1975] for small, stiff, and low surface energy systems and the Johnson-Kendall-Roberts [JKR, 1971] theory for large, soft, and high surface energy systems. The DMT model for sphere-on-flat contact predicts that the local contact stress transforms from compression to tension at the edge of contact area and attractive forces arise in the zone of molecular separation just outside the contact area. In the JKR model, on the other hand, the attractive forces are assumed to act inside the contact area, and tensile stresses are again exerted close to the contact edge. Thus, it might be expected that adhesion is rather correlated with the contact perimeter than the contact area. A consequence is that splitting up a large contact into finer subcontacts or, alternatively, subtracting finer subareas from this large contact, thus increasing the contact perimeter, should increase adhesion.

These adhesive contact models have been successfully used to study contact behavior and interfacial adhesion in many fields, but when the contact pairs decrease toward nano-scale, a primary limitation in these models becomes obvious for a full understanding of the details of

adhesive contact [Zhang, 2010]. This comes from an ideal simplification assumption of the contact geometry as an equivalent contact radius in all the models. So it is difficult to simulate the contact behavior on patterned surfaces or rough surfaces. When the contact objects fall into nano-scale, the contact geometry and interfacial clearance falls into the range of the intermolecular forces, which even become dominant.

To explain this, nano-scale adhesive contact mediated by Van Der Waals forces and the resulting interfacial forces (especially the pull-off force when separated) are typical fundamental problem involved in many areas such as stiction failure in micro electromechanical systems (MEMS) [Chen 2012], tip micro mechanics in atomic force microscopy (AFM) [Zhang, 2010], bionics, and mechanism investigation of bio-adhesive pads [Autumn, 2002; Gao, 2006]. For instance in the nature, the nano-scale adhesive contact resulted from Van Der Waals interaction has been utilized quite well by the hairy adhesive pads of insects and geckoes to achieve high dry adhesive efficiency on various surfaces. Infact, examples from the nature have revealed that many bio systems including insects and geckoes have utilized the nano-scale adhesive contact quite well by the fibril tip on their bio-pads [Crosby, 2007]. They are discovered to utilize contact splitting (a division of a contact area into a number of finer contact elements) and different nano-scale tip shapes of fibril on their pads to enhance separation strength or adhesive efficiency. The principle of contact splitting has been demonstrated by an optimization of fibrillar density observed in a variety of insects (beetles, flies, and spiders) and geckos. Larger animals have a higher density of fibrils since pull-off strength increases as fibril radius decrease [Gorb et al., 2009].

2.5.3 Prospect of Adoption in Engineering Applications

Bio-adhesion and Bio-mimicry are ingenious way to look into solving many engineering problems plaguing the industries these days. The amazing adhesive ability of geckos to climb and detach from ceilings and vertical walls at will have been studied extensively since the micro-mechanism of the attachment was shown to be predominantly due to intermolecular surface forces. Almost anyone and everyone who has worked in offices have used post-it/stick-em notes that are backed by tiny acrylic spheres that stick when they are tangent to surfaces. The adhesive's light touch enables it to be reused repeatedly. In recent decades, biological adhesion and bio-mimicry has risen above the technology behind ubiquitous office supplies and started to appear in engineering applications [Bhushan, 2012]. Understanding how naturally occurring surfaces function has inspired scientists and engineers to attempt to replicate those functions in engineering surfaces. A man-made fibrillar structure capable of replicating gecko adhesion has the potential for use in dry, super-adhesive tapes and surfaces that would be of use in a wide range of applications. These adhesives could be synthesized using micro/nanofabrication techniques or self-assembly.

As we master the understanding of how these natural surfaces work and how to replicate them artificially, more and more such materials, some with seemingly miraculous properties will reach the market. Study of the nature has already led to efficient adhesion and repulsion technologies being developed in research labs. For example hydrophobic surface texture discovered in lotus leaves by Wilhelm Barthlott and Christoph Neinhuis of the University of Bonn in Germany [Barthlott, 2011] can lead to the development of "space dust/debri repulsive" coatings for spacecrafts going on interstellar missions. The geometric feature dependent, highly adhesive characteristics of some of the surfaces found in nature can be replicated in metals,

ceramics, and composites and even state of the art alloy materials to enhance adhesion of protective and cosmetic coatings.

The emerging field of biomimetics is already gaining a foothold in the scientific and technical center stage. Over billions of years of evolution, Nature has used basic material to provide a breathtaking array of functionality to its creations, and we're discovering that one means for doing this is the clever use of hierarchical structures. As we understand the underlying mechanisms, we can begin to harness them for commercial applications. Significant advancements in nanofabrication has allowed engineers to replicate structures of interest in biomimetics using smart materials and shape memory alloys. The commercial applications include nanomaterials, nanodevices, and processes that may enable self-cleaning surfaces or pads that hang pictures without hooks or wires. Some of these applications may at first seem magical, but they are simply the results of applying science and engineering to the uncovering of the secrets of Nature. A nanostructured engineered material based on gecko-foot reusable adhesive would have a wide range of applications, from everyday objects such as adhesive tapes and fasteners to exotic items such as wall-climbing robots. But engineering such a material isn't straightforward. The design has to ensure that the fibrils are compliant enough to easily deform when pressed against a rough surface, but remain rigid enough not to collapse under their own weight. Spacing between the individual fibrils is also important: Too small, and adjacent fibrils can attract each other through intermolecular forces which will lead to bunching. The limits of current fabrication methods must also be taken into account [Bhushan, 2012].

CHAPTER 3. EFFECTIVE TBC ADHESION MODEL

3.1 Mechanism of Adhesion

Weiss in his elaborate deduction and journal publication [Weiss, 1995] divides the mechanism of adhesion into three major groups: mechanical interlocking, physical bonding, and chemical bonding (Figure 3-1). Adhesion between all substrate/coatings systems, in general the "joining technology" can be individually or in conjunction attributed to these mechanisms where always one has a relevant part over the other.

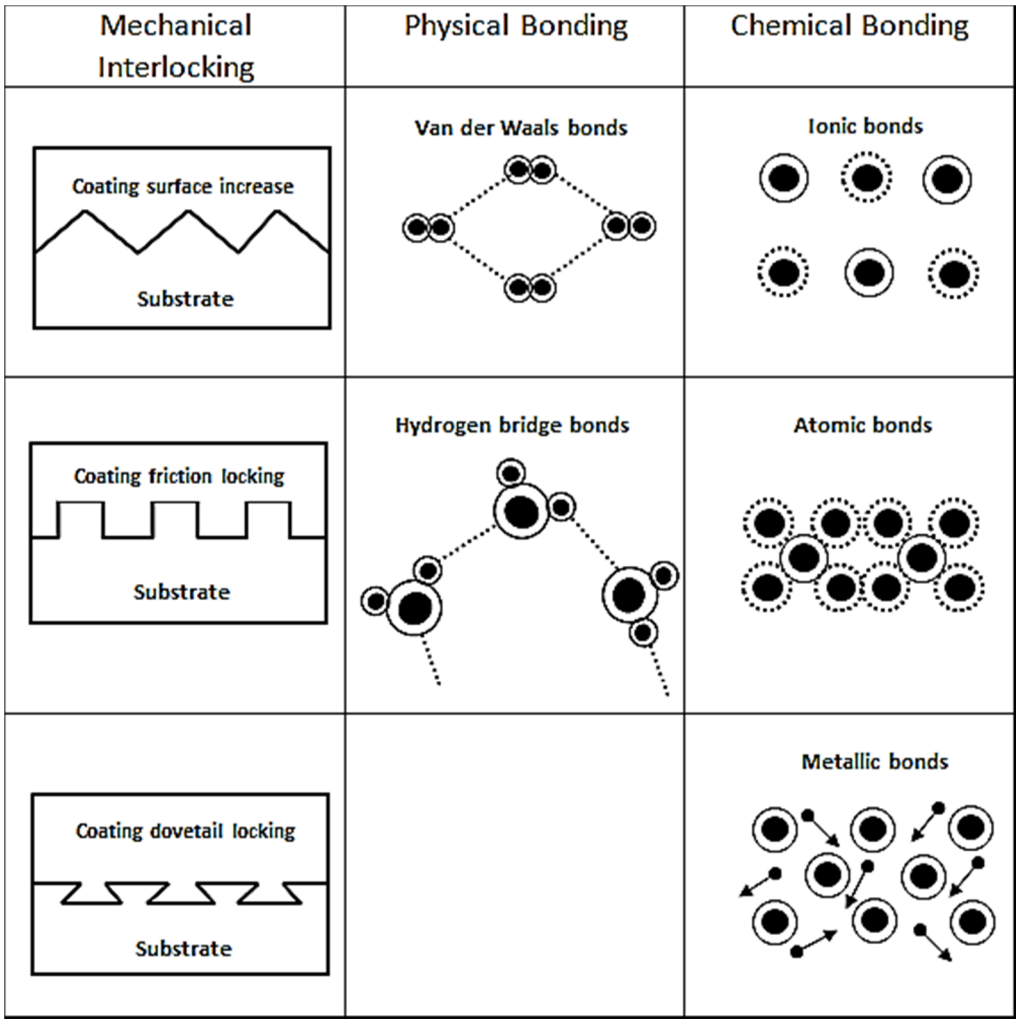

Figure 3-1 : Schematic diagram of the different bonding mechanism [Weiss, 1995]

3.1.1 Mechanical Interlocking

This form of adhesion can be sub-divided into two categories, locking by friction and locking by dovetailing. The forces that can be transmitted by mechanical interlocking depending on the size and geometry of the locking sites (Figure 3-2). These sites can vary from mechanically machined dovetails, grooves and other macroscopic shapes to undercut porosity by pickling and micro-roughness produced by grit blasting.

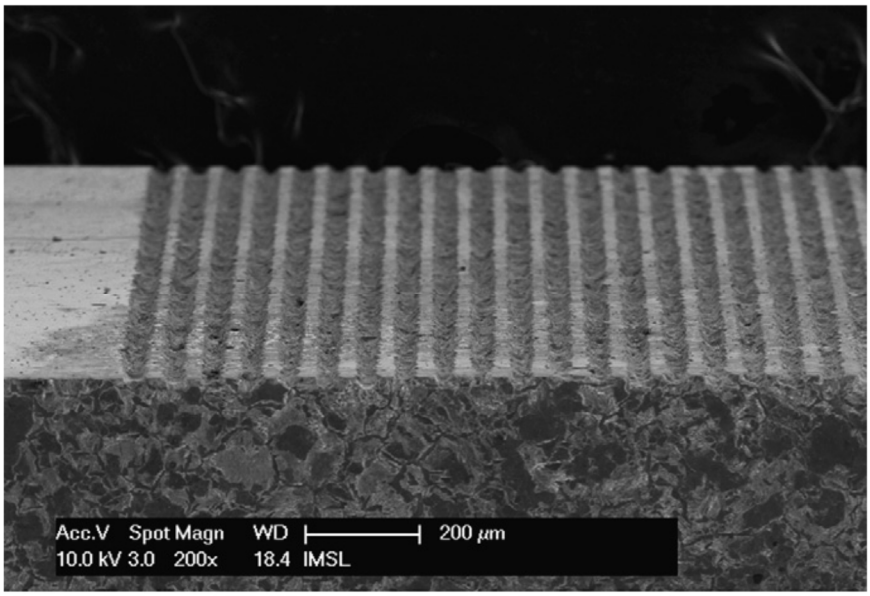

Figure 3-2 : Scanning electron micrographs of a microline-patterned steel surface. [Kim , 2010]

Depending on the topographical results, there are basically three different effects possible. The first is the increase in surface area by which any type of physical or chemical bonding will be more effective. The second consists of sites which give rise to friction between coating and substrate material which is evident when the frictional force $F_f = \mu F_N$ is high owing to a high coefficient of friction μ and high normal stresses F_N. these stresses can arise by the coating shrinking on the substrate because of high coating temperature and high coefficient of

expansion of the coating material. The third effect is true form locking with the forces to be transmitted depending on mechanical properties of materials involved. Since the magnitude of this effect is greatly influenced by the wetting properties of the coating, it is very sensitive to the type of coating technology, the materials used, and most coating parameters.

3.1.2 Physical Bonding

Physical bonds are bonding mechanism given by forces existing between atoms and molecules. This category involves two major adhesion mechanism Van Der Waals and Hydrogen Bridge bond; Van Der Waals bonds are basically a consequence of the correlations in the fluctuating polarizations of nearby particles (quantum dynamics) where these fluctuating polarizations depend on the relative orientation of the molecules (anisotropic molecules.)

Hydrogen bridge bonds, is the attractive interaction of a hydrogen atom with an electro negative atom, such as nitrogen, oxygen or fluorine, that comes from another molecule or chemical group. These bonds can occur between molecules, or within different parts of the same molecule. The hydrogen bond is stronger than Van Der Waals bonds, but weaker than any chemical bond. Physical bonds are very weak, their interaction energies are less than 50 Kj/mol over a distance of 0.3 to 0.5 nm and generally used accompanied by other adhesion mechanism [Hass, 2000].

3.1.3 Chemical Bonding

Ionic bonds, atomic bonds, and metallic bonds are considered chemical bond appropriate for effective adhesion. A chemical bond is an attraction between atoms that allows the formation of chemical substances that contain two or more atoms (Figure 3-3). The bond is caused by the

electromagnetic force of attraction between opposite charges, either between electrons and nuclei, or as a result of a dipole attraction.

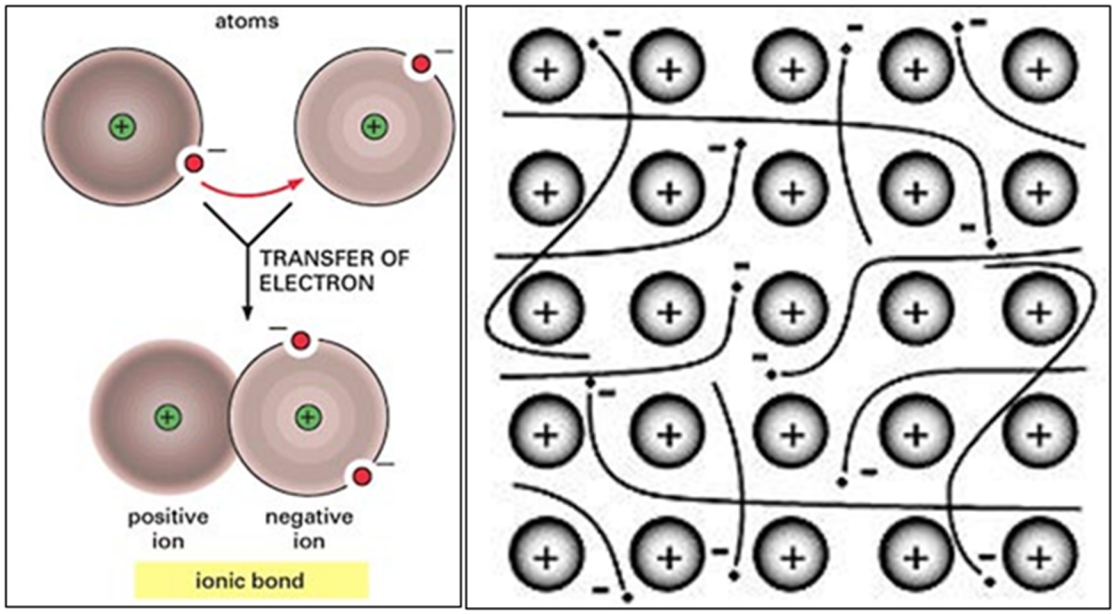

Figure 3-3 : Transfer of electrons in ionic bonds (left) and Compound of electrons sharing cations – metallic bond (right) [Peckham,1996]

Ionic bonds are formed through an electrostatic attraction between two oppositely charged ions, one metallic and other no metallic. However, pure ionic bonding cannot exist: all ionic compounds have some degree of covalent bonding. Thus, an ionic bond is considered a bond where the ionic character is greater than the covalent character. In addition, a less mentioned type of chemical bond is the metallic bond where each atom in a metal donates one or more electrons to a compound of electrons that reside between many metal atoms. In this compound, each electron is free to be associated with a great many atoms at once. The bond results because the metal atoms become somewhat positively charged due to loss of their electrons, while the electrons remain attracted to many atoms, without being part of any given atom. Chemical bonds are strong with energy levels between 110 and 260 Kj/mol with atomic and ionic bonds although these are 0.1 to 0.2 nm less far reaching. The forces of adhesion

resulting from these energies vary by at least one order of magnitude for a physical and chemical bonding .

3.2 Assessment

The quantitative determination of the adhesive strength is of vital importance for assessment of the overall performance of substrate/ coating systems in service but, depending on the adhesive strength and thickness of the coating, can be difficult or even impossible. However, certain techniques have been developed and are divided into three major groups as shown in Figure 3-4:

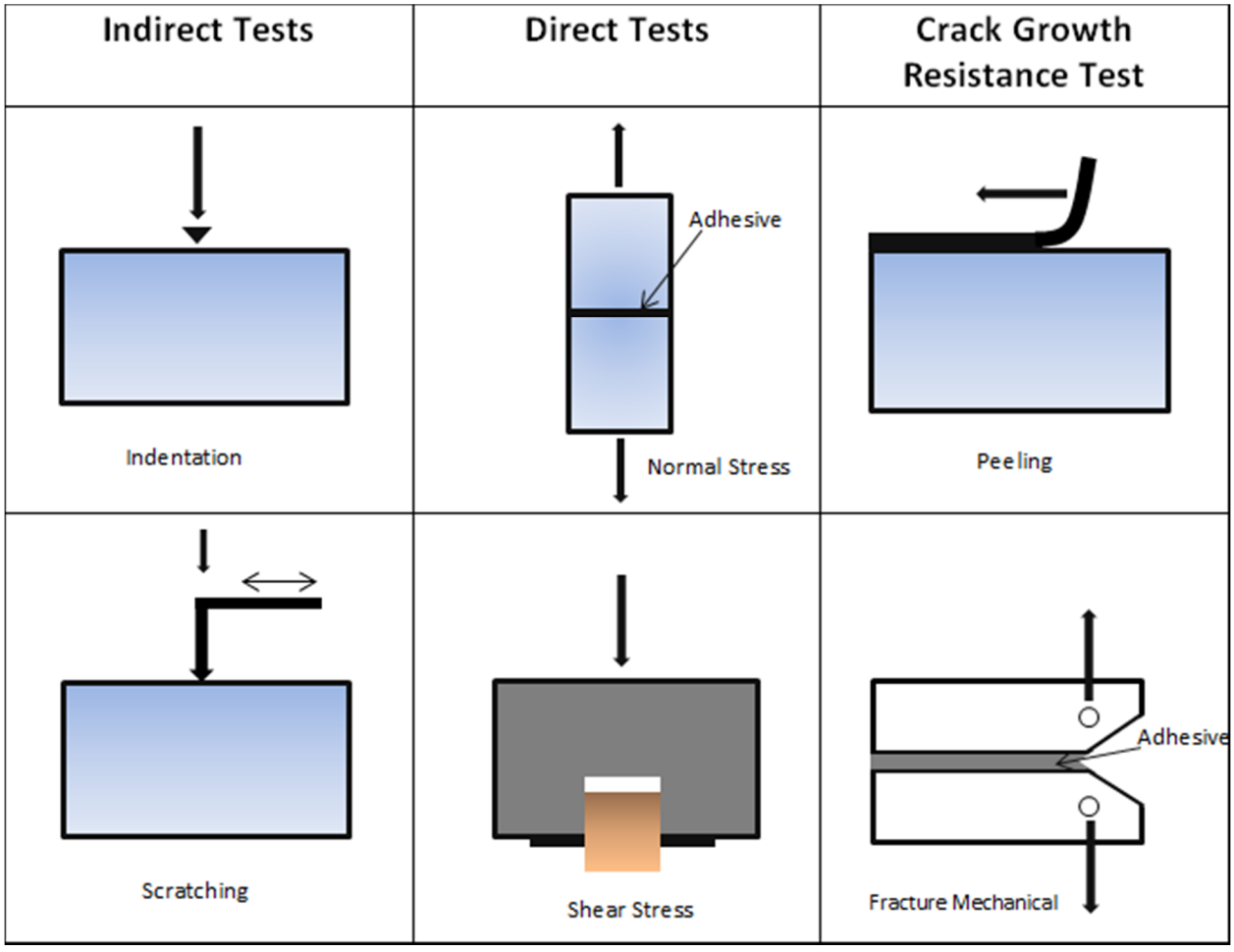

Figure 3-4 : Schematic diagram of different adhesion tests [Weiss, 1995]

3.2.1 Direct Methods by Application of Fairly Well Defined Normal Stresses or Shear Stresses

These tests require the application of loading to the coating, being pull-off and shear test the standardized and these are the most commonly used for TBC's adhesion strength testing.

Pull-off test: Pull-off testing is a quick, inexpensive method for measuring coating-substrate adhesion strength that has become widely used because it provides absolute numbers of adhesion strength, which allows for direct comparison of adhesion properties. In pull-off testing, a cylinder of substrate material is coated on its top face and adhesively bonded to an uncoated cylinder, using glue or epoxy resin, then a normal tensile force is applied to pull the cylinders apart, and the adhesion strength is defined as the applied stress at which failure of the coating-substrate bond occurs.

This test method uses a class of apparatus known as portable pull-off adhesion testers. They are capable of applying a concentric load and counter load to a single surface so that coatings can be tested even though only one side is accessible [ASTM D4541 - 09e1 Standard Test Method]. Measurements are limited by the strength of adhesion bonds between the loading fixture and the specimen surface or the cohesive strengths of the adhesive, coating layers, and substrate; however, simple mechanical hand-operated loading equipment can be used.

Although pull-off test is a standardized technique to measure the adhesion strength of thermal spray coatings, it presents various disadvantages, such as, the performing the test on coatings of thickness below 380µm , where according to ASTM C633, misleading high strength were conceived since the adhesive penetrated the coating (Figure 3-5). Furthermore, it is always important to notice that pull-off testing does not simulate real operational loading conditions.

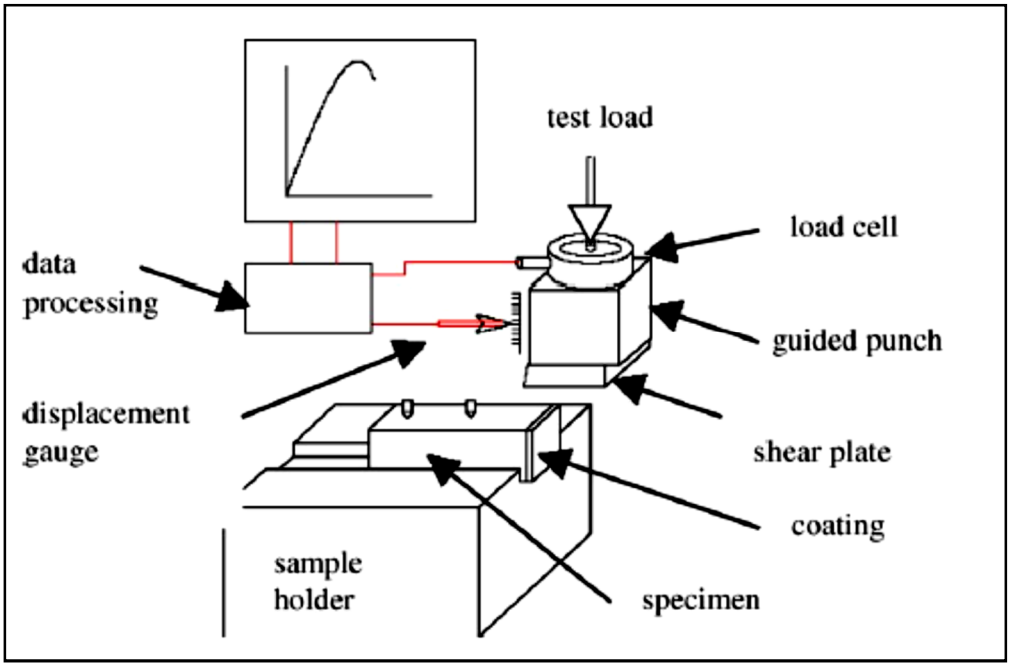

Figure 3-5 : Principles of the shear test device [Marot, 2006]

Shear test: The shear test was developed recently for a fast determination of the adhesion/cohesion of a coating on the substrate without the need of gluing, and describes better the mode of loading which is found more often in industrial applications.

3.2.2 Controlled Crack Growth Resistance Test

his special tesTt iinvolves peeling and fracture mechanical test; in both cases the adhesion strength is measured based on stable crack propagation. The following tests can be characterized under this specification:

Peeling test: When a bonded adhesive joint is gradually forced from edges inward, the tearing of the adhesive which occurs is called peeling. Experience in the field and the laboratory has shown that unbounded area in a bonded panel can become a localized source of failure which will progressively become enlarged when the panel is subjected to sufficiently high static or

alternating loads. Since these loads are usually smaller compared to the shear operational loads, peel strength of metal adhesives is a property to be considered [Heimann, 1998].

Peeling test is an adhesion test that has both, the predictive ability of the fracture mechanism test and the simplicity of the forced based test. Several standard test configurations exist, and many studies on the mechanics of the test system were undertaken because of its wide use in the adhesives industry; however, in general peeling testing consists of a few things. Adherent is pulled from its substrate. The crack propagates in a stable manner at the peel speed. The force required to continue cracking is monitored as a function of the crack position and time. The peel test produces a force versus displacement that represents the strength of adhesion of the coating.

The resulting peel strength represents the incremental energy per unit width per increment peeled and has units of N/m. The peel test essentially measures the average adhesion along the line of the crack tip; as the crack progresses, a different portion of the interface is loaded. In addition, on thin coatings the coating is peeled from the substrate, where the peel stresses and forces depend largely on the coating properties, and stable peeling is not always possible.

There are two basic forms for peeling test; they are both similar in terms of sample preparation and procedure but can generate very different crack tip stresses. The first, the compliant adherent is peeled from the substrate at a specified angle, where the most commonly used are 90° and 0◦, from the substrate plane. The shape of the adherent is controlled by its properties and the properties of the interface and substrate; therefore, the stress intensity at the crack tip and the amount of plastic work performed to bend the adherentt for a given peel load is

a function of all the material properties of the system and the peel angle. This configuration is very similar to the double cantilever configuration shown in Figure 3-6. (a)

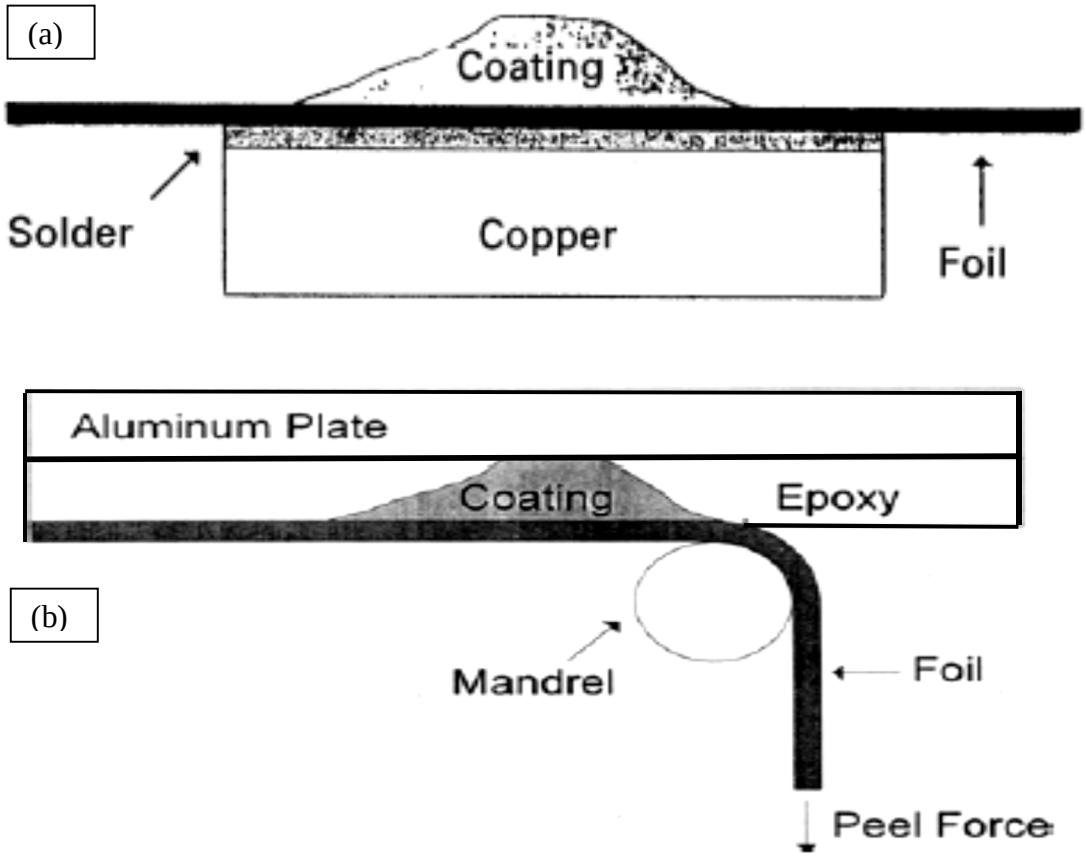

Figure 3-6 : (a) Double cantilever configuration & (b) Peeling around a mandrel configuration for controlled crack growth resistance test [Lima, 2007]

On the second form, the adherent is bent around a rotating mandrel; therefore, the shape of the deformed adherent is controlled [Figure 3-6.(b)]. The strains in the adherent conforming to a mandrel are usually much smaller than in the free peeling tests. In this case the amount of plastic work depends on the adherent properties only and can be controlled by changing the mandrel size. Moreover, the stress intensity at the crack tip depends on the properties of all of the materials involved, but because of the smaller strains, the mechanical description of the system is simpler.

Fracture mechanical test: This test, developed to calculate the adhesion energy Gc required for stable crack propagation is measured by either four points bending test or the three point sheart test. A stable crack is initiated to be propagated from a perpendicular notch along the weakest interface of a multilayer specimen (Figure 3-7), where stable crack propagations at a constant load between the two inner loading points occur. The critical strain energy release rate is derived from this stable force recorded on the load-deflection curve, without any requirement of crack length measurement [Thery, 2007].

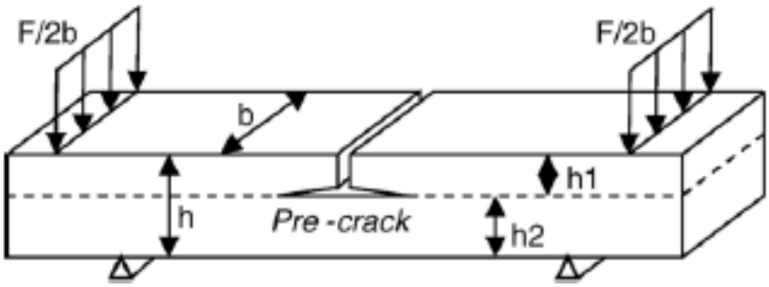

Figure 3-7 : Four point bending test. Adhesion energy of a YPSZ EB-PVD layer in two thermal barrier coating systems.

Conferring to the research by Thery [Thery, 2007]., the four point bending method adapted to the system of interest, which includes a thin and brittle columnar ceramic layer. Such adaption consisted in bonding stiffening layer to the top of the ceramic layer. The steel layer was bonded using an epoxy adhesive cured at 100° for 30 minutes. It increases the stored energy in the top layer of the adhesion test specimen and therefore also the driving force for crack propagation. Consequently, the load needed to propagate the interfacial crack becomes smaller. This prevents the ceramic layer and the bond coat from cracking and the substrate from yielding. Later on, a perpendicular notch was machined through the stiffening layer and the top coat at the center of the specimens to enable the propagation of the symmetric cracks during the test.

As mentioned before, only stable interfacial crack propagation can give a reading of adhesion energy; therefore, the introduction of a pre-crack to the system is a pre-requisite in this test. Indeed, without any preset crack, a large load would be needed to initiate the crack and the specimen could consequently be overloaded, and reliable results would not be achieved [Cheng, 1999].

3.3 Failure Mechanism

Evans on his paper Mechanism Controlling the Durability of Thermal Barrier Coatings gives some generalities regarding the most common failures mechanism attributed to TBCs and subdivided them as shown in Figure 3-8 below:

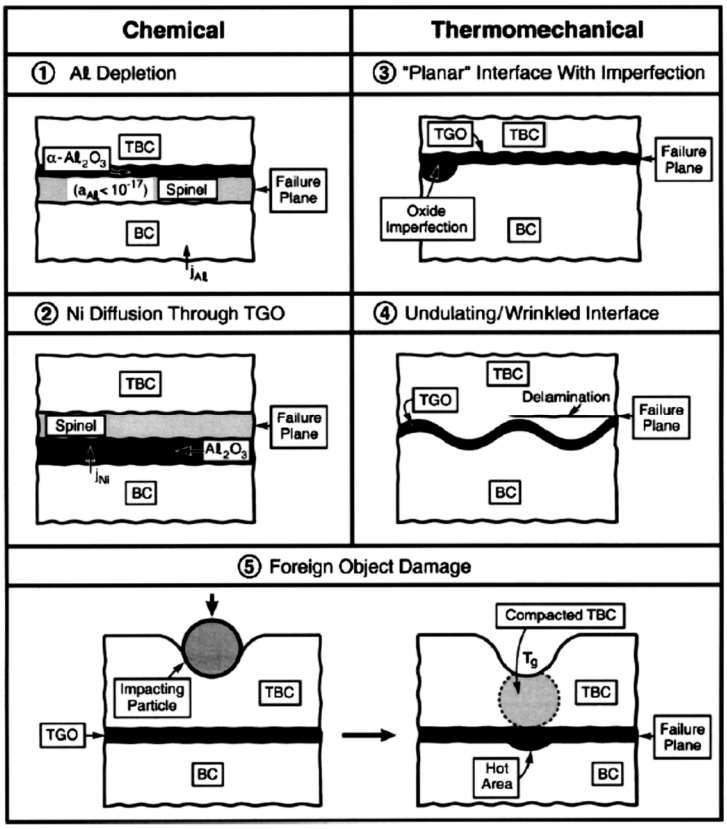

Figure 3-8 : Five major failure categories documented for TBC systems [Evans, 2003]

In addition, Evans stated that:

i) Spinel's formation can occur either between TGO and the bond coat, or the TGO and the ceramic layer. "When this happens, it is surmised (but not substantiated) that the brittleness of spinel results in delamination" [Evans, 2003]

ii) TBCs system are also exposed to particle impact and, how Evans called it, foreign object damage (FOD) that causes local compression on the TBC system creating a hot spot

iii) The energy density in the TGO and surrounding imperfections also affect TBC durability (Evan's research scope) where failure evolves through a sequence of crack nucleation, propagation, and coalescence events.

Besides Evan's work, Christensen [Christensen, 2004] on their paper Atomic-Level Properties of Thermal Barrier Coatings: Characterization of Metal-Ceramic Interfaces describes different spallation mechanism, and subcategorizes them in three major groups:

i) Buckling effect, which can result from planar compressive stresses within the ceramic layer, is formed due local conditions creating both out-of-plane and shear tensions. Recent research demonstrated that buckling failures occurs when the delamination crack is at least sixteen times the TBC thickness; however, for thick oxides buckling is not viable,

ii) Sometimes failures display surface wedging effect. This effect is based on the development of a through-thickness shear crack in the TBC due to compression.

iii) And more recently wrinkling, a mechanism depending upon a void formation under the TBC and subsequent folding effects which may lead to cracking.

Figure 3-9 shows a schematic diagram of three spallation models described by Christensen.

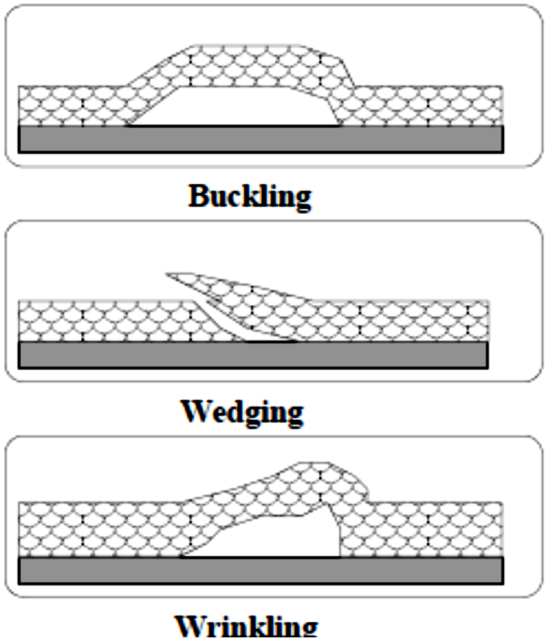

Figure 3-9 : Spallation Mechanism of the TBC [Christensen, 2004]

Composition of the substrate and bond coat effects adhesion of alumina formed during bond coat oxidation. When the alumina spalls, the zirconia layer is not maintained, so the TBC fails. In conclusion, migration, segregation, and stress generation are key areas of concern in thermally grown oxide region, where mismatch during thermal cycling and oxide formation are the major causes of spallation.

CHAPTER 4. METHODOLOGY OF ELETROLYTIC PLASMA PROCESSING

4.1 Phenomenology

In this research work the surface modification technique being proposed is known as Eletrolytic Plasma Processing or EPP for short. This cathodic electrolytic plasma process (EPP) was originally introduced as a new corrosion prevention method. It is a green, environment friendly and cost-effective method of metal surface treatment. The EPP procedure and the EPP-treated 1018 steel are being explored on detail for their novel characteristics [Liang et al., 2012]. On EPP treated surfaces, a spontaneous pattern due to localized melting and quenching could be obtained through EPP. Scanning electron microscopy and energy dispersive X-ray spectroscopy were used to characterize the special surface morphology and chemical patterns on EPP resultant features during this research. Standard corrosion tests were conducted in EPP-treated samples. The corrosion analysis indicates that the EPP treatment could effectively improve the uniform corrosion of 1018 steel in 3.5% NaCl solution [Meletis, 2002]. With longer time of EPP treatment (15 minutes), the passivation was significantly extended and hence the localized corrosion resistance was improved. Also, the higher corrosion resistance was found to be sustainable (in 48 hours corrosion test, NaCl solution) on all the EPP treated samples.

4.2 Embedded Mechanism

Electrolytic plasma processing involves two characteristic phenomena (i) electrolysis of a liquid environment by application of different electrical potentials between the workpiece material and a counter-electrode; and (ii) the production of an electrical discharge at, or in the vicinity of, the workpiece surface. Although the discharge phenomena associated with electrolysis were discovered more than a century ago by Sluginov [Sluginov, 1980], their

importance as an emerging surface engineering process were realized only very recently [Meletis, 2002]. A typical electrode current–voltage characteristic curve of the electrolytic cathodic process is shown in Figure 4-1.

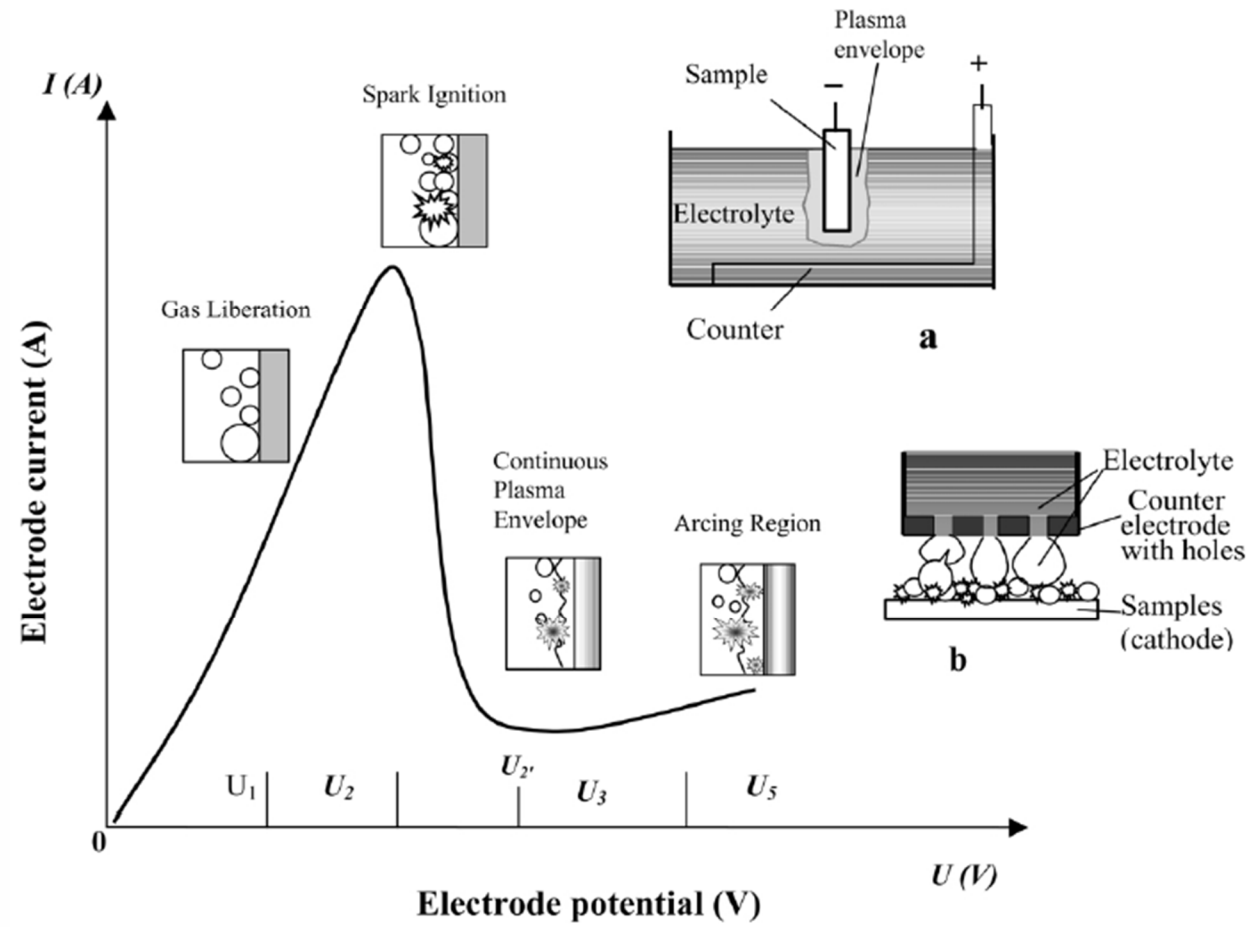

Figure 4-1 : Current-Voltage dependence in electrolytic plasma discharge

The normal glow discharge zone U_2–$U_{2'}$–U_3 is usually selected as the work region, where the electrode current decreases but plasma intensity increases when the electrode voltage increases from U_2 to $U_{2'}$. The samples (as a cathode) can be either immersed in the electrolyte [Figure 4-1. (a)] , or dripped with electrolyte [Figure 4-1.(b)]. However, the corresponding slope of the electrode Current– Voltage curves in the U_2–$U_{2'}$ segment is different in these two cases.

For the configuration shown in Figure 4-1.(a) (i.e. the workpiece is immersed in the electrolyte), the current sharply drops from the highest point to the lowest point when the electrode voltage increases from U_2 to $U_{2'}$. For the configuration in Figure 4-1. (b) (i.e. in this case, the electrolyte drips down to the workpiece through small diameter holes on the cathodic electrode plate), the slope of the U_2–$U_{2'}$ line (i.e. current reduction rate) is much smaller than that of Figure 4-1. (a). It is found that the plasma intensity increases when electrode voltage increases, and when $U_{2'}$ is reached, a continuous envelope is formed on the sample surface, which results in rapid increase of the surface temperature with increasing electrode voltage. The normal operation voltage in this work is within U_2–$U_{2'}$. Although there is heating of the substrate due to plasma action, the bulk substrate temperature remains relatively low (less than 200–300°C) due to the simultaneous cooling action by the electrolyte solution. The local surface temperature adjacent to plasma bubbles, however, is very high, which is critical to cleaning mill-scale and enhancing the metallurgical connection of the coating microstructure

The U_3 zone is determined as the working region, where the electrode current reduces but plasma intensity increases from U_2 to U_3. This rise in plasma evolution is due to the fact that almost all the voltage is reduced in this limited contact region between the gaseous hydrogen bubble and substrate surface. The sample (cathode) can be either immersed in the electrolyte or electrolyte can drip on the sample [Cionea, 2010] through a perforated anode. When dripping, the electrolyte is released onto the work piece through small holes made in the anode and forms an enveloping foam that has a stabilizing effect on the plasma formation. A plasma envelope is fully formed at U_3 characteristic voltage and this is the normal operating voltage for surface treatment. This regime was first mentioned by Kellogg [Kellogg et al., 1973] and is called Kellogg region. Although there is heating of the substrate due to plasma action, the bulk

substrate temperature remains relatively low (<100ºC) due to simultaneous cooling action by the surrounding electrolyte solution. The local surface temperature adjacent to plasma is very high, which is critical for the interactions at the near surface and the effect produced on surface characteristics. The current density was shown to depend on geometrical factors related to the electrodes (size, shape, orientation and electrode gap).

4.3 Surface Modification Process

Electrolytic plasma process is an efficient surface modification method for metallic materials, which makes it suitable for metallic bond-coat interfaces in TBC. With proper control of the process parameters Electro-Plasma Process (EPP) could generate unique surface morphology, which is suitable for effective cleaning of the metallic surfaces and inherently, good adhesion strength can be achieved for eventual coating of the surfaces. Increasing input voltage beyond the conventional Faraday region of electrolysis, luminous discharge is observed on the surface of one of the electrodes. The electrode surface must be covered by layers of bubbles before the discharge could be set in. The discharge of energy is then taken place in an explosive way with 'localized' 'high temperature'-plasma bubbles. The combination of heat and kinetic impact effectively removes the surface contaminants and produces a unique surface morphology. The conditions of process control parameters and the resultant surface conditions that could be achieved were studied in some detail during this research as well.

The electrolytic plasma phenomena was discovered and applied for many years. Early studies reported the phenomena of electrolytic plasma, also termed as "glow discharge" in many early papers, which could be induced on electrode surface under certain conditions (Figure 4-2). The yield and chemical reaction rate depend on the energy input [Gupta et al., 2007]. In the study

of anodic discharge, it was suggested to form empirical equation for the breakdown voltage shown in Eq-1

$$U_B = a_B + b_B \log \rho \quad \text{.....(1)}$$

where, U_B is the breakdown voltage, a_B and b_B is constants for a given metal and electrolyte composition respectively, and ρ is the electrolyte density. In his work temperature was not reported to have a direct effect on the threshold voltage appearing at the metal surface

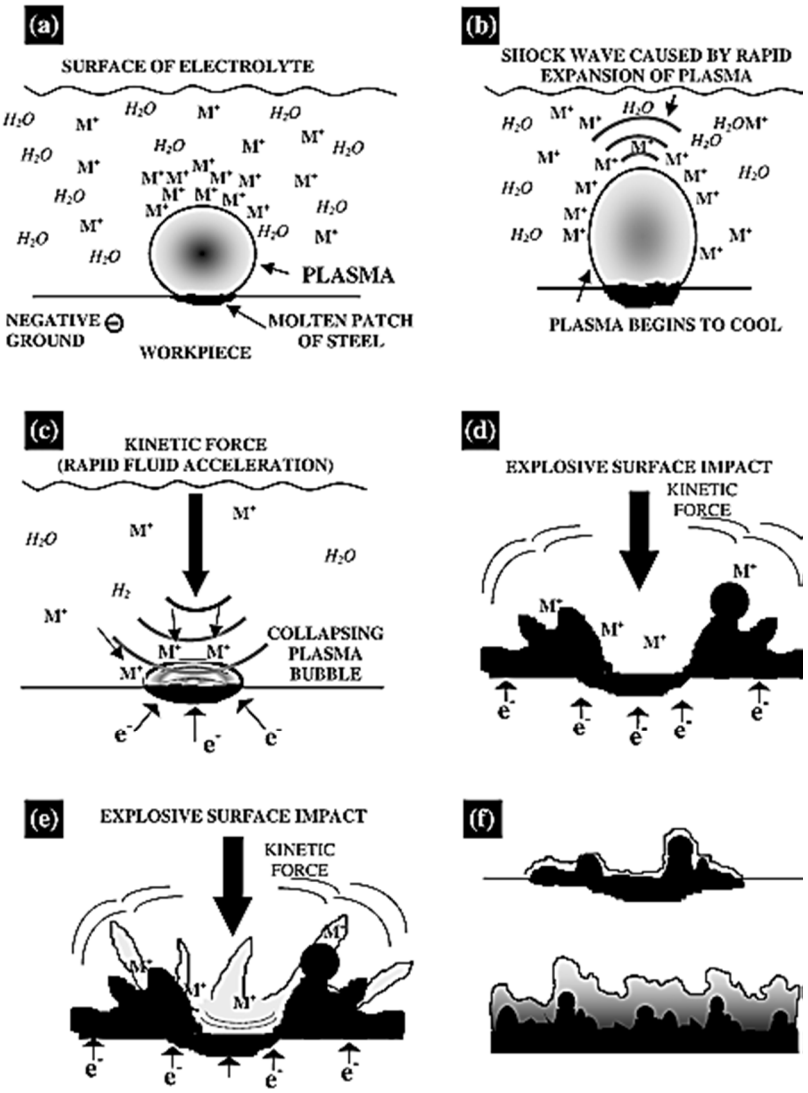

Figure 4-2 : Schematic of the EPP process and generation of desired morphology (Gupta, 2007)

Table 4-1 : Sample characteristic data of the EPP treated surfaces [Melatis 2002]

Property	**Cleaned Surface**	**Zn-Al coatings**
Thickness	-	18 µm
Deposition rate(µm/s)	-	0.56 (0.41-0.56)
Roughness(R_a)	2.5 µm (1.8-3.4 µm)	2.3 µm (0.8-3.8 µm)
Element content	1.38 wt.% O_2 (1.38-7.3 wt% O_2)	3.0 at.% Al, Zn bal. (0.2-0.3 at. % Al. Zn balanced)
Adhesion Strength (MPa)	-	> 70 (30 to >70)
Hardness (GPa)	1.9 (bulk steel)	1.30

Table 4-1 shows a sample investigation run to find out relevant characteristics data for a Zn-Al coated EPP treated sample. The roughness profile was measured with a profilometer. The EPP cleaned surfaces were characterized in density (microhardness), roughness, composition, thickness, uniformity and continuity. Table 4-1 presents the range of these characteristics and those of the best coatings (based on a statistical analysis of performance data).

In this research, we experimented with an EPP process of our own to modify the surface morphology of the metal samples. This process was carried out with a custom experimental setup and a set of lab experiments to achieve the desired morphology in the samples.

4.4 Experimental Setup

Our experimental setup consisted of an electrolysis chamber with a modified cover to insert the electrodes and hold them firmly during plasma generation. A custom pressure process chamber was also made to test the effect of the pressure on the plasma generation.

There were two different parts of this experiment, one was performed in atmospheric pressure and in the other one a custom built pressure chamber was used to pressurize the electrolytic chamber and test the effect of heightened pressure on process parameters like surface roughness and geometry. Both are shown in Figure 4-3:

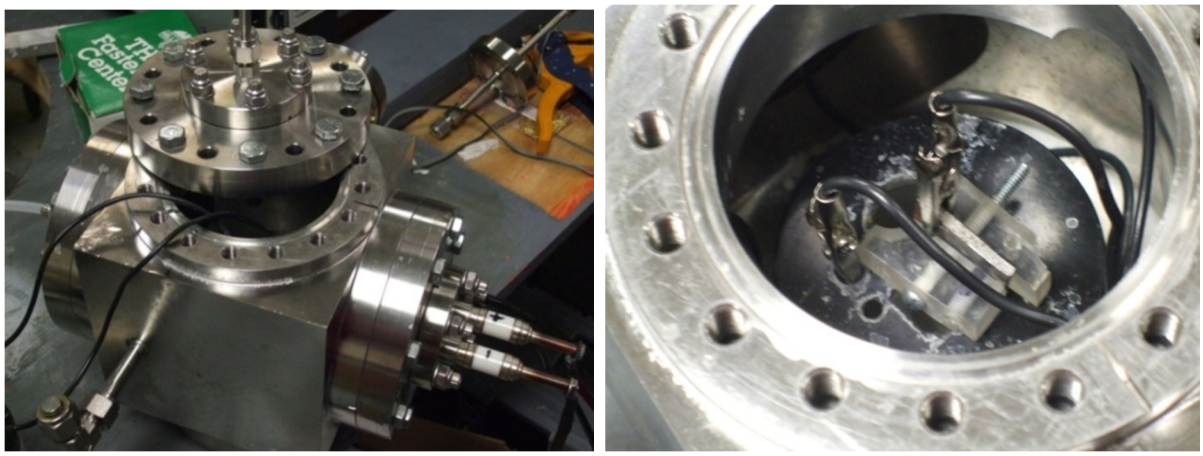

Figure 4-3 : Stainless steel pressure chamber (left) and electrolysis chamber setup inside (right).

Two sets of experiment were presented. Firstly, the electrodes were selected to be of the same material and same size (brass sheet, 0.5 mm x 3 mm x 15 mm), except the cathode was slight smaller (2 mm less in length) to ensure the plasma discharge occurs at the cathode region. Current-voltage behavior was obtained from this test.

Then for other sets of tests aluminum (Al-1100) and low carbon steel (1008/1012 carbon steel) were used as cathode material (0.3 mm x 3 mm x 12 mm) for EPP. The power supply used was a Magna-power PQA, which produces DC power with maximum capacity of 250 V and 26A(Figure 4-4). The current supply was initially set to maximum and the voltage was increased manually till the initiation of plasma.

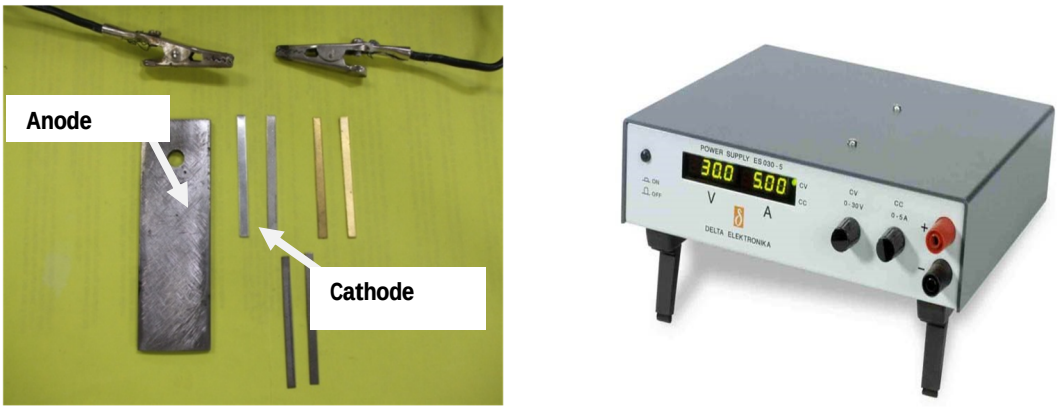

Figure 4-4 : Assortment of electrodes (left) and Magna-power PQA apparatus (right)

4.5 Procedure followed

4.5.1 Part I: Non Pressurized Test at Atmospheric Condition and Conventional Glow

The configuration for this part of the experiment is the generation of conventional glow discharge, where two electrodes are immersed in a stationary solution bath. A copper wire was used as cathode in this experiment, while a steel plate (which is larger in surface area than the cathode) was chosen as the anode in order to make sure that the plasma occurs on the cathode surface [Figure 4-5].

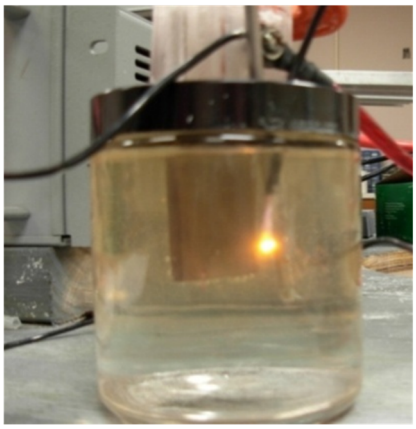

Figure 4-5 : Non pressurized test at atmospheric condition and conventional glow .

Sengupta and Singh [Gupta et al., 2007] concluded from their work that the plasma location depends on the resistivity of the electrolyte in the vicinity of the electrode. Hence, within a close circuit, the smaller electrode experiences higher power density and consequently, higher joule-heating occurs on the smaller electrode; thus the bubble layer forms earlier on the smaller electrode (cathode) than on the larger electrode, which is anode in this particular configuration. So the resistivity increases more significantly on the smaller electrode. It is consistent with our observation that the location of plasma depends on the size of the electrodes and generally, a smaller electrode often attracts the plasma.

The solute used in our experiment is sodium carbonate. Different concentrations were selected to produce different conductivity of the solution (2.5 mS/cm to 26.6 mS/cm). The distance between the immersed electrodes is kept at 10 mm within the solution. The temperature was measured by a small thermocouple probe in the vicinity of the cathode to record the environment temperature (5 mm from cathode), since the rise in temperature only occurs locally.

4.5.2 Part II: Pressurized Test with Contact Glow Discharge

For this part, the CGD configuration was adopted; hence the electrical circuit remains the same except that the solution bath was enclosed in a process chamber, which could be sealed and pressurized [Figure 4-6]. Argon gas was used to pressurize the chamber.

The pressure in the chamber could be controlled by an external pressure supply and monitored with the pressure gauge fitted with it. The maximum pressure reached was around 100 psi . The voltage and current output data coming out from the cathodic reactions and the plasma formation were recorded with the help of a ADC device and logged with “instruNet LabView” software.

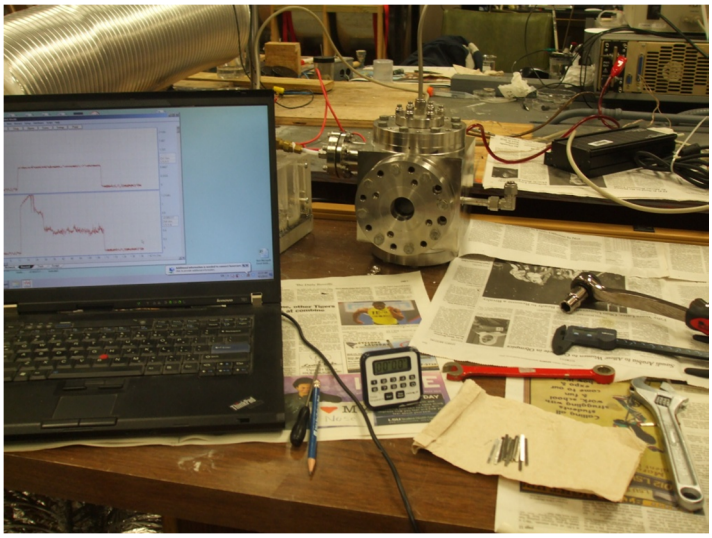

Figure 4-6 : Pressurized test at gradually increasing pressure (CGD) and monitoring.

Open-circuit potential of each groups were recorded for over 48 hours. All the tests were repeated at least 3 times. The statistical average of the value or typical curves are presented in Figure 4-7.

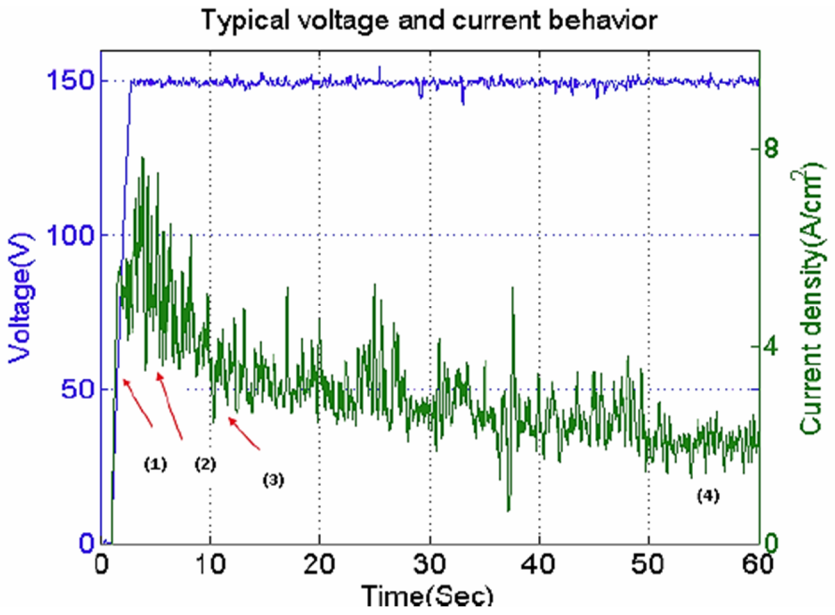

Figure 4-7 : Example of a characteristic Voltage vs Current curve.

All sample materials were grit blasted on one side, since rough surface could induce more crater and spheroid features which are desirable for stable plasma discharge. The electrodes were immersed vertically into the electrolytic solution. The resultant surface features were then investigated with Scanning Electron Microscope (SEM).

CHAPTER 5. FINITE ELEMENT ANALYSIS OF BIO-MIMETIC ADHESION MODELS

5.1 Approach

To make a connection between the mushroom shaped spheroids and the nano sized adhesion enhancing geometries appearing in nature, an algorithm was used to digitally map the contours of the shapes appearing on EPP treated surfaces. The algorithm was used to synchronize with an open source image processing workflow called "CellTracer" developed in Duke University by the research group of Quanli Wang [Wang et al., 2008]. The Matlab code uses Matlab's built in image processing toolbox and a technique called "image segmentation" to map the contour of any geometry from a raster image to an accuracy of $1x10^{-3}$. In this case the images were snapshots of SEM micrographs taken from the EPP runs on different surfaces.

The contour mapping was done to figure out the aspect ratios of the mushroom head spheroids that would be simulated virtually to test for adhesion. In this research work the finite-element (FE) method is developed to model the nano-scale adhesive contact of elastic bodies with an adhesive pressure derived from the interatomic interaction Lennard-Jones potential, which permits numerical solutions for a variety of interface geometries. By systematic comparison with the analytical results from conventional Hertz, JKR, and DMT models, the validity of the FE model is verified. For nano-scale contact, the assumption of equivalent radius adopted in the Hertz model is initially investigated and proved to be improper for nanoscale adhesive contact due to the distribution variations of interfacial force caused by local contact geometry. Then adhesive contact behaviors of four typical nano-scale contact geometries inspired by tip shapes of bio-adhesive pads and that found on EPP treated surfaces are investigated in detail, which are flat punch tip, sphere tip, mushroom tip, and empty cup tip.

5.2 Contour mapping through mathematical code

For the contour mapping, a set of image snapshots of the EPP related research done at University of Texas at Arlington [Cionea , 2010] were evaluated. The evaluation was done to find out an average aspect ratio (Height, Radius and Curvature) of the common geometric pattern appearing in an EPP treated surfaces. The images were then overlayed and their contour traced with the Matlab code and the CellTracer software to find a workable geometry. The data acquired from the superimposed geometry would later be used to run finite element analysis of the shape dependency of adhesion processes. The workflow followed by the CellTracer Matlab executable can be explained as shown in Figure 5-1:

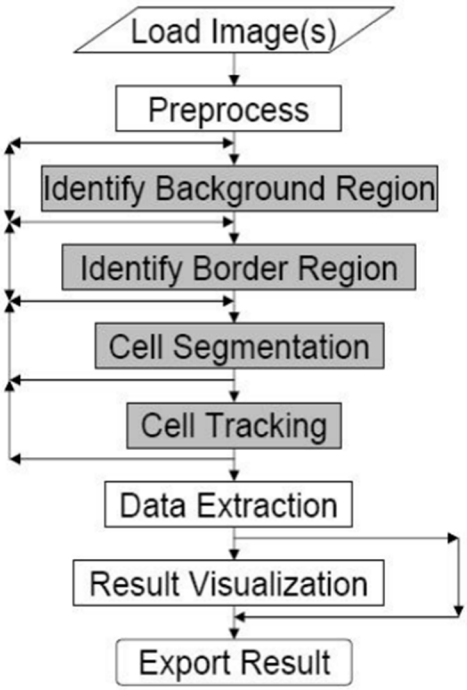

Figure 5-1 : Embedded workflow followed for data extraction from SEM images

A sample run of the superimposing and data acquisition process is given in Figure 5-2:

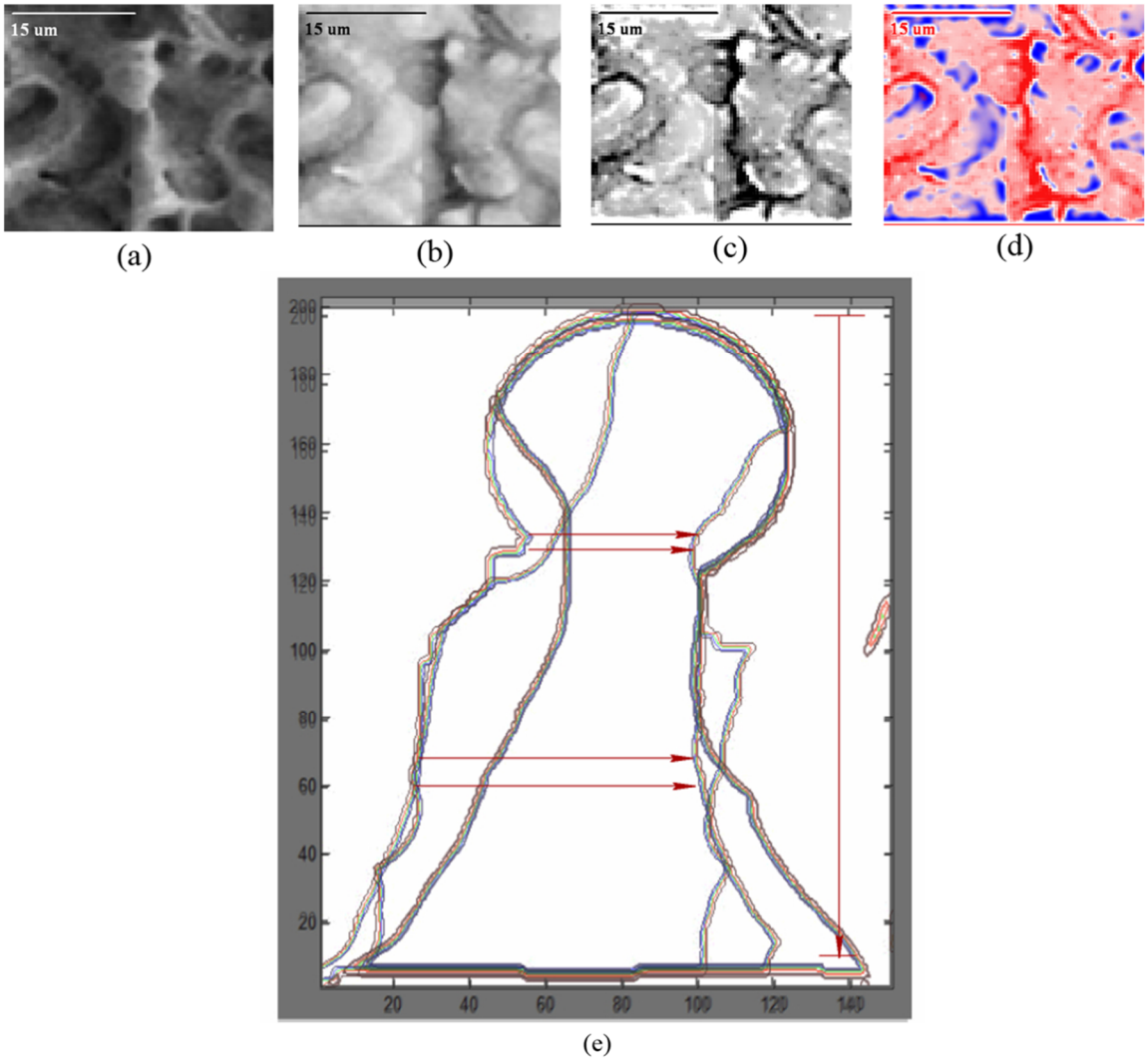

Figure 5-2: Steps of contour mapping, (a) Image acquisition , (b) Inverting the image, (c) Sharpening the outlines, (d) Feature detection, (e) Overlaying and dimensional measurement

The image acquisition was done with an open source fractal image capture software called “Fast Stone Capture”. The inversion, sharpening, feature detection and overlaying as well as coordinate tracking were done with CellTracer Matlab Code [Appendix A]. The data points acquired were averaged with an integral averaging algorithm. When combined with the works of Del Campo [Del Campo, 2007] on other tip-shapes and micro geometries, Table 5-1 can be conjured for the comparison of the size effect in adhesion process:

Table 5-1: List of aspect ratio and dimensions of the shapes and surface patterns compared

Contact geometry	Pillar radius, r (μm)	Tip dimensions (μm)	E^* (MPa)	Splitting efficiency (at P_p = 1mN) Exp (Theory)
Flat tip 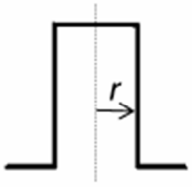	2.5		1.38	-0.48 (-0.5)
	5		1.30	
	10		0.95	
	25		0.76	
Spherical tip 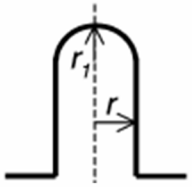	2.5	r_1 = 9.3	1.34(*)	-1.00 (-1)
	5	r_1 = 16.4	1.13(*)	
	10	r_1 = 24.1	1.02(*)	
	25	r_1 = 39.3	0.58(*)	
Flat tip with rounded edges **(Cup shape)** 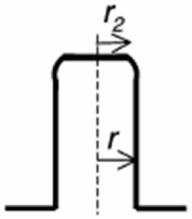	2.5	r = 2.9 r_2 = 2.7	1.38	
	5	r = 5.2 r_2 = 4.8	1.00	
	10	r = 10.0 r_2 = 9.0	1.16	
	25	r = 25.5 r_2 = 21.6	0.85	
Mushroom tip 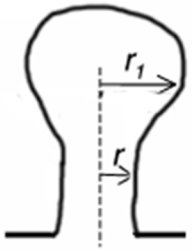	10	r_1 ~ 12.9±0.3	2.50(*)	-2.26
	25	r_1 ~ 32.1±1.5	1.81(*)	

This table presents a comparative look into the data obtained from the image acquisition and analysis software and that from established literature in this field. The parameters mentioned are the same in each case and they are the governing dimensional characteristics of the micro geometries.

5.3 Finite Element Modeling of Contact Elements

5.3.1 Formulation

To build a dynamic modeling of micro-scale adhesive contact, the interfacial force modeling is initially needed to consider the actual interfacial interaction with the varying contact area and interfacial clearance.

Theoretically, when two adjacent atoms approach in a distance of nanometer or less, various interatomic potentials have been proposed to describe the interaction. Among them Lennard-Jones potential is one of the widely used function because of its simplicity and inverse sixth-power attractive Van Der Waals term, which is usually written as the following equation

$$\omega(r) = 4\varepsilon\left[\left(\frac{\sigma}{r}\right)^{12} - \left(\frac{\sigma}{r}\right)^{6}\right] \qquad \text{.....(2)}$$

where ε is a parameter determining the depth of the potential well [Del Campo, 2007] and σ is a length scale parameter determining the minimum position of the potential. Then by triple integration of the Lennard-Jones potential, the interaction force between two surfaces can be given by the following equation:

$$p(h) = \frac{8\Delta\gamma}{3e}\left[\left(\frac{e}{h}\right)^{9} - \left(\frac{e}{h}\right)^{3}\right] \qquad \text{.....(3)}$$

Where p is the pressure exerted by one surface on the other, h is the vertical separation between the corresponding point pairs on the two interacting surfaces. $\Delta\gamma$ is the work of adhesion, or surface free energy and e is the local equilibrium separation.

5.3.2 Mathematics of Shape Effect in Adhesive Contact

Most theories in classical contact mechanics, including JKR , DMT and Maugis–Dugdale models [JKR, 1971] , are focused on contact between parabolic surfaces $r^2/2R$, in which case the pull-off force ranges between $3\pi R\Delta\gamma/2$ and $2\pi R\Delta\gamma$ depending on the Tabor number of the problem under consideration.

On the other hand, the pull-off force is strongly influenced by the surface profile of the contact bodies. To illustrate this point, a simple formula was mentioned by Gao [Gao, 2006] for a frictionless axisymmetric rigid punch having an arbitrary profile $z = f(r/a)$ in contact with an elastic halfspace. In this case, the stress distribution (tension being positive) underneath the designated shape is given by:

$$\sigma_{zz}(r,0) = -\frac{E^*}{2a}\left[\frac{\chi(1)}{\sqrt{1-r^2/a^2}} - \int_{r/a}^{1} \frac{\chi'(t)}{\sqrt{t^2-r^2/a^2}}\,dt\right] \qquad \text{.....(4)}$$

Where,

$$\chi(t) = \frac{2}{\pi}\left[\delta - t\int_0^t \frac{f'(x)}{\sqrt{t^2-x^2}}\,dx\right], \qquad E^* = \frac{E}{1-\nu^2} \qquad \text{.....(5)}$$

Here a is the radius of the contact region, δ is the penetration of the punch tip, ν is Poisson's ratio and E is Young's modulus of the substrate. It can be shown that Eqs. (4) and (5) also apply to contact between two elastic bodies if contact between two elastic bodies E^* and f (r) are generalized to:

$$f(r) = f_1(r) + f_2(r), \qquad E^* = \frac{E_1}{1-\nu_1^2} + \frac{E_2}{1-\nu_2^2}, \qquad \text{.....(6)}$$

where subscripts 1 and 2 denote quantities pertaining to the two solids. The stress distribution in Eq. (4) consists of two parts: one is compressive with vanishing value at r = a, similar to the Hertz model, and the other part has an inverse-square-root singularity at the contact periphery r = a, similar to the JKR model. Applying Griffith's energy balance [Griffith, 1921] to the singularity term at the contact edge leads to:

$$K_{\mathrm{I}} = \lim_{r \to a} \sqrt{2\pi(a-r)}\,\sigma_{zz}(r) = -\frac{E^* \chi(1)\sqrt{\pi}}{2\sqrt{a}} \qquad \text{.....(7)}$$

$$\mathcal{G} = \frac{K_{\mathrm{I}}^2}{2E^*} = \frac{E^* \pi}{8a}\chi^2(1) \qquad \text{.....(8)}$$

$$\mathcal{G} = W_{\mathrm{ad}} \qquad \text{.....(9)}$$

where W_{ad} denotes the work of adhesion which is taken to be the surface *energy* $\Delta\gamma = \gamma 1 + \gamma 2 - \gamma 12$ in the absence of bulk dissipation. Combining Eqs. (8) and (9) gives:

$$\chi(1) = -\sqrt{\frac{8\Delta\gamma a}{\pi E^*}}. \qquad \text{.....(10)}$$

Inserting Eq. (10) into Eq. (4) and integrating over the entire contact area $r \le a$ gives the applied pulling force as:

$$P = \sqrt{8\pi\,\Delta\gamma\,E^* a^3} - \frac{\pi E^*}{a}\int_0^a r \int_{r/a}^1 \frac{\chi'(t)}{\sqrt{t^2 - r^2/a^2}}\,\mathrm{d}t\,\mathrm{d}r. \qquad \text{.....(11)}$$

Equations (11) and (5) generalize the JKR model to adhesive contact between elastic bodies with arbitrary axisymmetric surface profiles. Consider the power law profile:

$$z = f(x) = \frac{r^n}{nR^{n-1}} = \frac{a^n x^n}{nR^{n-1}} \quad (n > 0) \qquad \text{.....(12)}$$

where R is the characteristic length. Different values of exponent n lead to different surface shapes shown in Figure 5-3 .

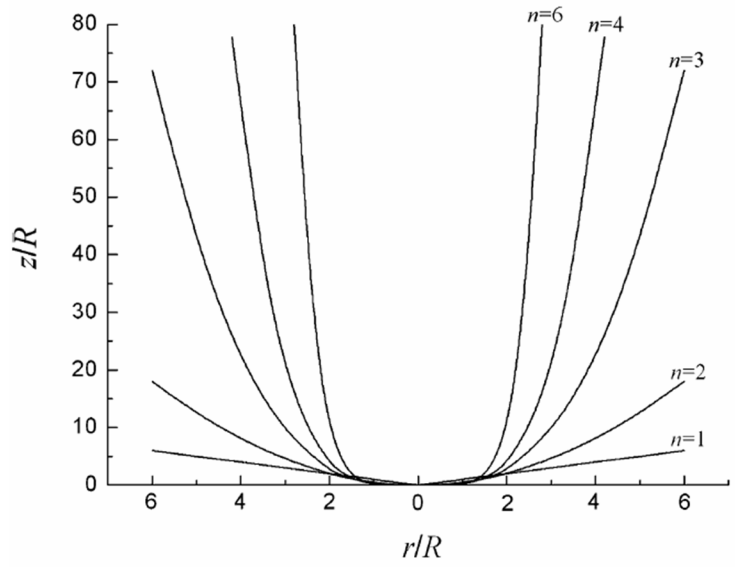

Figure 5-3 : Power law surfaces $z = r^n/nR^n$. The parabolic case n = 2 is most widely used in contact mechanics theories

The case n = 2 corresponds to the parabolic shape used in most of the classical contact mechanics models to approximate a sphere of radius R. Substituting Eq. (12) into Eq. (5) results in:

$$\chi(t) = \frac{2}{\pi}\left[\delta - \frac{\sqrt{\pi}a^n t^n \Gamma(n/2)}{2R^{n-1}\Gamma(1/2+n/2)}\right] \qquad \text{.....(13)}$$

where Γ (·) is the Gamma function. Taking derivative of Eq. (13) with respect to *t* and inserting the result in Eq. (11) yields the pulling force:

$$P = \sqrt{8\pi a^3 E^* \Delta\gamma} - \frac{2\sqrt{\pi} a^{n+1} \Gamma(1+n/2) E^*}{R^{n-1}\Gamma(1/2+n/2)} \int_0^1 s\,\mathrm{d}s \int_s^1 \frac{t^{n-1}\,\mathrm{d}t}{\sqrt{t^2-s^2}} \quad \text{.....(14)}$$

where s = r/a. Interchanging the order of integration in Eq. (14) leads to:

$$P = \sqrt{8\pi a^3 E^* \Delta\gamma} - \frac{2\sqrt{\pi} a^{n+1} \Gamma(1+n/2) E^*}{R^{n-1}\Gamma(1/2+n/2)} \int_0^1 t^{n-1}\,\mathrm{d}t \int_0^t \frac{s\,\mathrm{d}s}{\sqrt{t^2-s^2}} \quad \text{.....(15)}$$
$$= \sqrt{8\pi a^3 E^* \Delta\gamma} - \frac{2\sqrt{\pi} a^{n+1} \Gamma(1+n/2) E^*}{(n+1)R^{n-1}\Gamma(1/2+n/2)}.$$

Given E∗, Δγ and n, Eq. (15) expresses the applied pulling force as a function of the contact radius a. The maximum value of *P* occurs at the contact radius:

$$a = a_c = \left[\frac{3\Gamma(1/2+n/2)}{\sqrt{2}\Gamma(1+n/2)}\right]^{2/(2n-1)} \times R^{2(n-1)/(2n-1)} (\Delta\gamma/E^*)^{1/(2n-1)} \quad \text{.....(16)}$$

Which gives the pull-off force as

$$P_c = \sqrt{2\pi}\left(\frac{2n-1}{n+1}\right)\left[\frac{3\Gamma(1/2+n/2)}{\sqrt{2}\Gamma(1+n/2)}\right]^{3/(2n-1)} \times E^{*(n-2)/(2n-1)} R^{3(n-1)/(2n-1)} \Delta\gamma^{(n+1)/(2n-1)} \quad \text{.....(17)}$$

Equation (17) indicates that the pull-off force P_c depends on the exponent n, hence on the surface shape/contour and not the size. From Eqs. (16) and (17), one can write the average contact stress at pull-off as:

$$\bar{\sigma}_c = P_c/\pi a_c^2 = \sqrt{2/\pi}\left(\frac{2n-1}{n+1}\right)\left[\frac{\sqrt{2}\Gamma(1+n/2)}{3\Gamma(1/2+n/2)}\right]^{1/(2n-1)} \times E^{*n/(2n-1)} (\Delta\gamma/R)^{(n-1)/(2n-1)}. \quad \text{.....(18)}$$

In general, the average stress given in Eq. (18) is much smaller than the theoretical adhesion strength σ_{th} unless the characteristic size R is reduced to below a nanoscale threshold. Given the shape effect described in Eqs. (17) and (18), the research work was further advance to study whether there exist surface shapes which allow the average stress at pull-off to reach the theoretical adhesion strength.

5.3.3 Modeling

To identify the benefit of the mushroom head, stress analysis of compliant fibrils attached to a stiff substrate is carried out by the finite element method. The boundary value problems solved are illustrated in Fig. 5-4. The fibril is considered to be fully adhered to a rigid, flat surface. Since its diameter is at least 100 times the width of the shaft of the largest fibril, the sphere is modeled as flat, and the applied load considered axial.

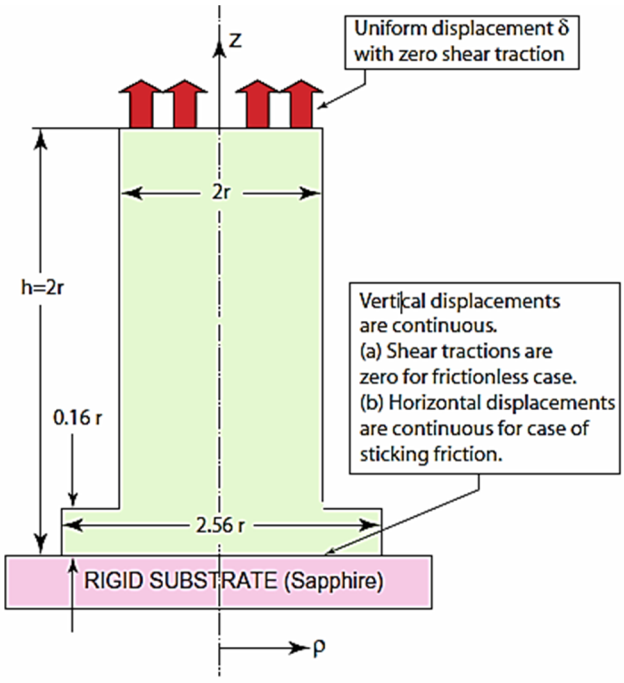

Figure 5-4 : Configuration analyzed by the finite element method. Mushroom head is absent, replaced by a disc of diameter 2r and thickness 0.16r.

Similarly, the contrast in Young's modulus, E, between the compliant fibril, at approximately 2 MPa, and the stiff surface, at almost 400 GPa, is so great that the compliance of the flat surface can be neglected. The adhesion between the fibril and the flat substrate is regarded to be friction-free for one set of computations, and under sticking friction conditions in another set. In the case of sticking friction, the fibril is considered to be stress and strain free, and with its entire end just touching the flat substrate under zero applied loads. A typical contact geometry of sphere to flat substrate is illustrated in Figure 5-5 (a)

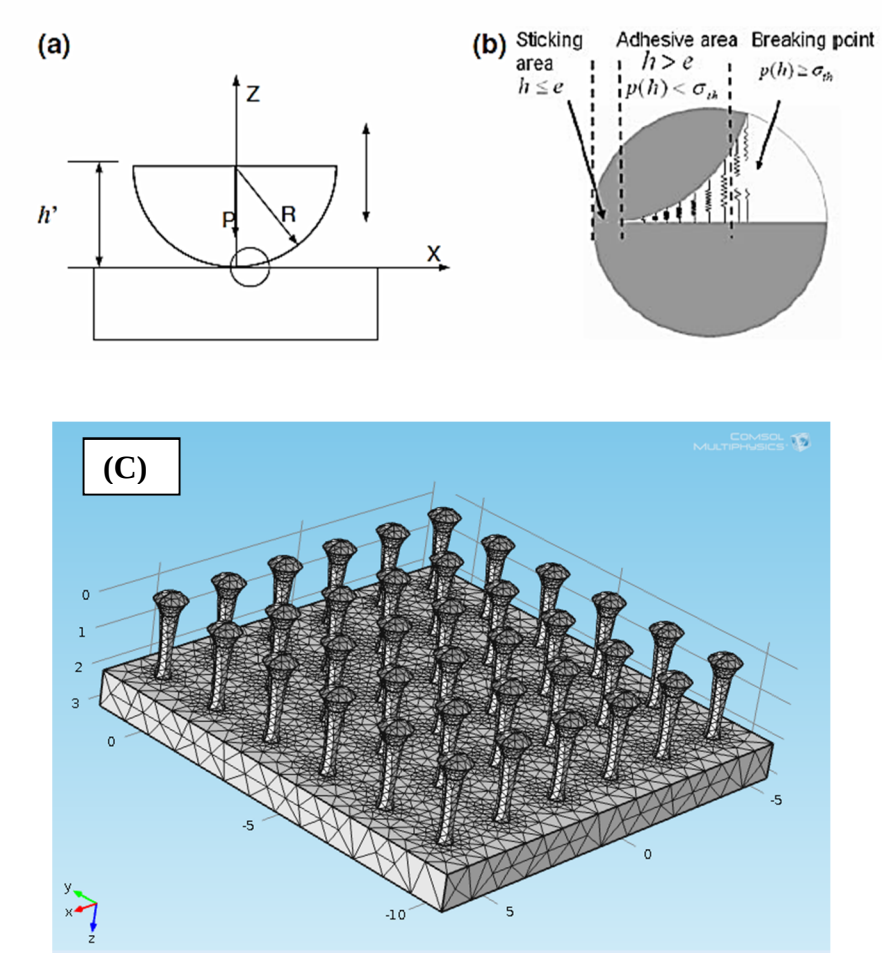

Figure 5-5: A typical contact geometry of micro-scale mushroom heads its FE modeling. (a) The center of the sphere is at a height h' above a rigid half space. (b) Contact occurs when the varying clearance $h = h' - R \le e$ and the resulting local contact area. (c) FE modeling of the contact by COMSOL.

The center of a sphere of radius R is at a height *h'* above a rigid half space. The sphere is assumed to be linearly elastic with Young's modulus *E* and Poisson's ratio *v*. Contact occurs when $h' - R \leq e$ and the resulting contact area radius is denoted as *a*.

P indicates the normal load of the contact. The varying clearance along the local geometry is denoted as variable h. For the contact geometry in Figure 5-5.(a), a finite element (FE) adhesive contact model is set up and implemented using the commercial finite element analysis software COMSOL. As shown in Figure 5-5.(c), finite element mesh for the contact pairs was constructed with 4-node free tetrahedral elements because previous studies have proven this to be the most efficient meshing algorithm for arbitrary geometries. The surface of rigid body is modeled as an infinite rigid plane. To describe the dynamic contact process (approach and separation of the two surfaces) in detail, the general FE simulation flow of the contact process is modified, and the interfacial interactions as Eq. 2 is incorporated into the contact cells. As shown in Fig. 5-5.(b), at the critical moment of the breakage of a pair contact cells (pull-off point), the critical local stress is defined as a tensile stress equal to a theoretical strength of adhesion, i.e., p(h) at r^{th}. To reveal the geometry details of the contact area, the contact area is divided into two zones in this article, namely sticking area and adhesive area according to the attractive or repulsive nature of the interfacial forces. Sticking area is located on the center of the whole contact area comprising of interacting point pairs with $h \leq e$ in Fig. 5-5.(b). Adhesive area is the round annular part comprising the point pairs with $h>e$ as well as $p(h)<\sigma^{th}$. Clearly, interfacial clearance h is a varying distribution function over the contact area depending on the local deformation and contact geometry. In the FE modeling, normal load P is defined as the reaction force from the substrate, which equals the vertical force on the substrate in the COMSOL software to keep the contact system in equilibrium. $P>0$ indicates that the

contact point pair experiences a repulsive force, while P<0 indicates an interfacial attractive force. The maximum attractive force during detaching process is defined as the pull-off force. To compare with the conventional contact models, we normalize the load P and the deformation displacement d using interfacial adhesion force $\pi\Delta\gamma R$ as in the following equations ,

$$\overline{P} = \frac{P}{\pi\Delta\gamma R} \qquad \text{.....(19)}$$

$$\overline{\delta} = \delta\left(\frac{16E^2}{9\pi^2\Delta\gamma^2 R}\right)^{\frac{1}{3}} \qquad \text{.....(20)}$$

where $\Delta\gamma$ is the work of adhesion, E is the equivalent elastic modulus, and R is the equivalent radius in Hertz contact.

5.3.4 Verification of the F.E. Modeling

To verify the FE model built in this article, elastic adhesive contact of a nano-scale sphere with a smooth semi-finite rigid body is analyzed using the FE adhesive contact modeling and compared with the results from the conventional adhesive contact models. The sphere is considered with radius R = 10 nm, Young's modulus E = 100 GPa, Poisson's ratio m = 0.3. Frictionless contact is assumed. For Van Der Waals interaction, Dc usually ranges between 10 and 50 mJ/m^2, which is assumed as 10 mJ/m^2 in this article according to literature [Zhang, 2010]. The effective equilibrium distance of Van Der Waals force is taken to be e = 0.23 nm. We also adopted σ^{th} = 20 MPa according to the work by Zhang. At each equilibrium step, the local interfacial stress is dependent on the varying clearance and deformation according to Eq. 3. To focus on the adhesion force, the modeling begins from a contact state with pure adhesive force and zero normal load. By increasing and then decreasing the interfacial deformation

displacement ‘d’ , the variations of normal load and contact area are calculated step by step based on the equilibrium as shown in Figure 5-6 below:

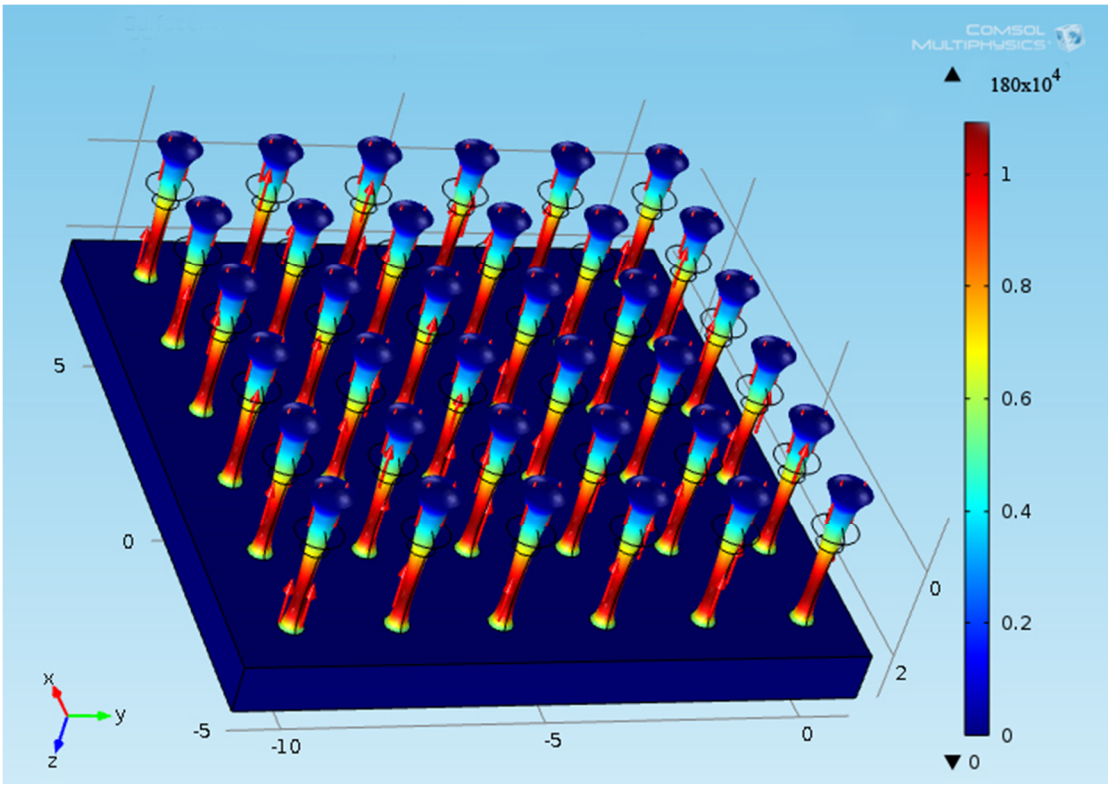

Figure 5-6 : Array of elastic, adhesive contacts, patterned on a 10x5 nm block for simulating adhesion

Within the separation step, when the deformation displacement is gradually decreased, the FE contact cells outside the contact area break when the local tensile stress increases up to the critical stress σ^{th}. The contact area is decreased step by step until the whole breakage of the contact objects. Then the deformation curve is obtained and normalized by Eqs. 19 and 20.

As shown in Figure 5-7, the deformation displacement contour indicates the points of maximum strain in the mating surfaces. The section inbetween the fibrils were modeled to have vaccume or air on different simulation runs. The modeling made sure that there were no penetration of the adhesive material into the crevices inbetween the fibrils.

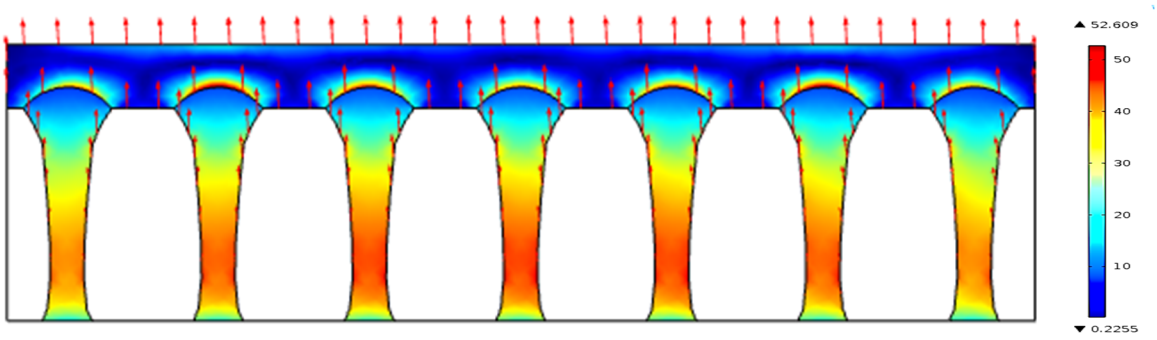

Figure 5-7 : Deformation displacement contour during approach and separation

Results are shown in Figure 5-8. The black square points indicate the theoretical results from Hertz model, in which the normal load decreases to zero as the interfacial deformation d decreases to zero. The empty circle points indicate the pull-off process based on JKR model. A pull-off force exists when d approaches to zero. It presents the same rule of DMT model indicated by triangle points. The reverse triangle points indicate the FE modeling results including both the approaching and detaching processes. Obviously, the force curve falls in the

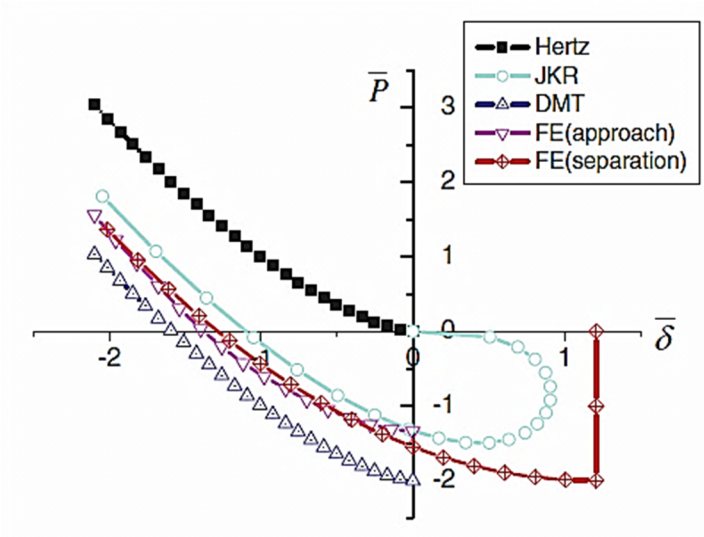

Figure 5-8 : Comparison between the FE modeling and the conventional contact models of Hertz, JKR, and DMT. The force curve of FE modeling falls in the gap between JKR model and DMT model due to the adopted interfacial force model in Eq. 3

gap between JKR model and DMT model. The main reason of the differences comes from the different interfacial force models. The JKR model considers the adhesion force only inside the contact zone, while the DMT model includes the adhesion force outside of the contact zone. As depicted in Fig. 5-5 (b), the interfacial force function in our FE modeling covers the whole contact area, so the load-deformation curve falls between those of JKR and DMT models. Obviously, the interfacial force model in Eq. 3 is dependent on the geometry and deformation of the local contact area. The obtained force curve also indicates that the numerical results of the FE contact modeling keeps quite a good agreement with that from the widely accepted conventional models (Figure 5-9).

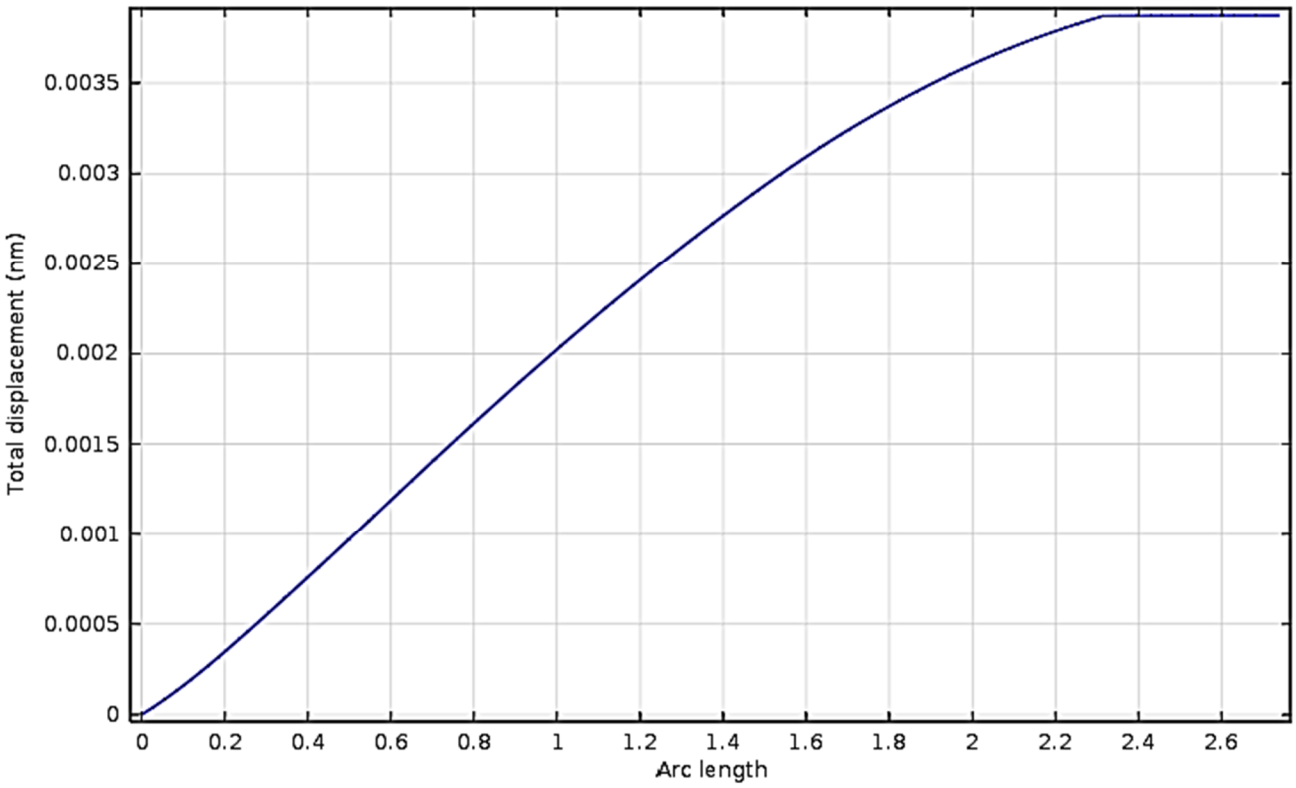

Figure 5-9 : Total displacement curve during the F.E simulation of the fibrils.

Further verification can be ensured by observing the trend of the displacement generated in the F.E interface and it's comparison with the actual case observed in the works of Crosby [Crosby, 2007]. The total displacement vs arc length graph shows the gradual increase of the displacement along the step length of the spheroids, until it reaches a stable value at around 2.2 nm.

The graph shown in Figure 5-10: **Spike in Von Mises stress values around the contact perimeter of the muhsroom head where the separation occurs.** further matches up with the prediction in the work by Jagota [Jagota et al., 2011] which says that the separation will start from the perimeter in contact with the adhesion block.

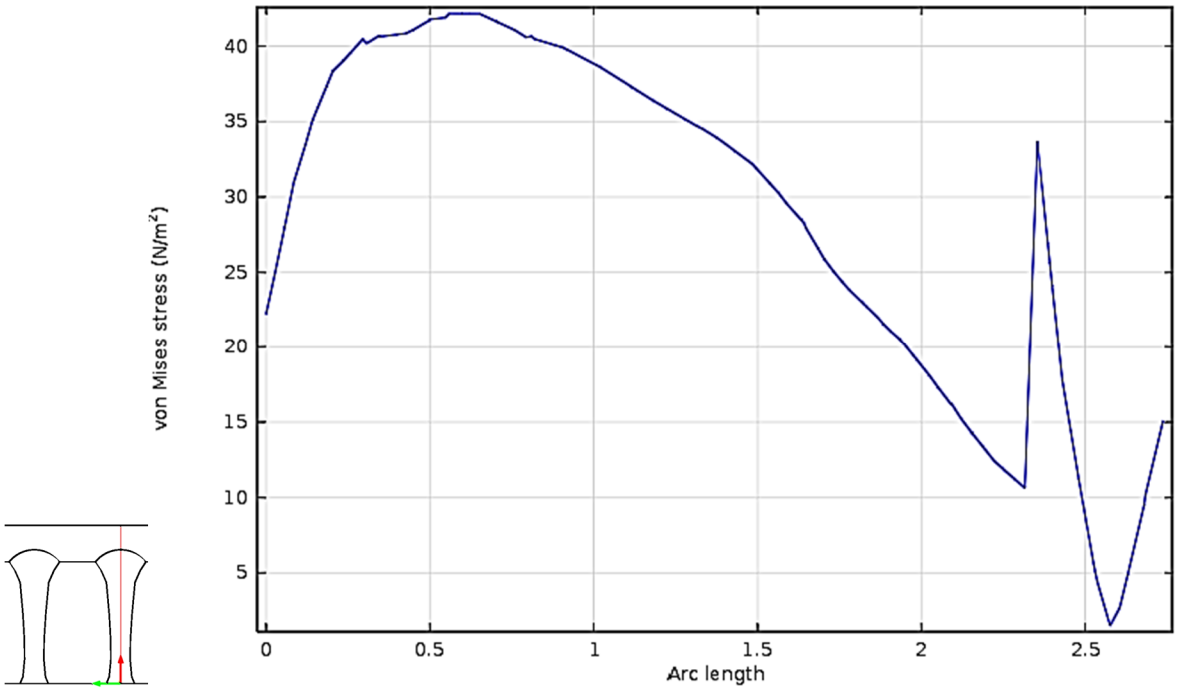

Figure 5-10: Spike in Von Mises stress values around the contact perimeter of the muhsroom head where the separation occurs.

The example of mechanism in Crossby's work only considers energy dissipation at the interface, but the three-dimensional (3D) geometry of a patterned interface also plays an

important role. The aspect ratio of the features increases conformability to the contacting surface. Higher aspect ratio features are more compliant, which improves their adaptability to rough surfaces and maintains interfacial contact. This mechanism cannot be overemphasized, as adhesion is most dependent upon the ability of two surfaces to establish contact. Additionally the aspect ratio of the fibrils structures defines the constraints at the interfaces. Less constraint leads to a decrease in the stress concentration along the interface. In other words, increasing the aspect ratio of the feature effectively “blunts” an interfacial crack during separation.

Even further validation of the finite element mesh and model was performed by doing a mesh independence study. For this the following criterions were checked independently during several, consecutive mesh refinement runs:

- Mesh and Solver
- Element Quality
- 1G Reaction Forces
- Free body checks
- Discretization error check.

The error estimation and compromise steps included:

- Stress recovery and discretization error estimation.
- Discretization error and model updating
- Reducing discretization errors
- Configuration errors and model updating
- Applying Iterative approach-Penalty function method.

The F.E model was updated using the following protocol:

- Application of the industry standard direct updating methods using modal data (reference basis methods).
- This was followed by the Lagrange multiplier method .

The mesh refinement analysis yielded the following result where it can be seen that after 2x refinement (Figure 5-11), the relative errors didn't exceed beyond a factor of 10^{-4}. This proved the mesh independence of the model and solving method adopted. So a two level refined mesh approach was adopted for the rest of the simulation.

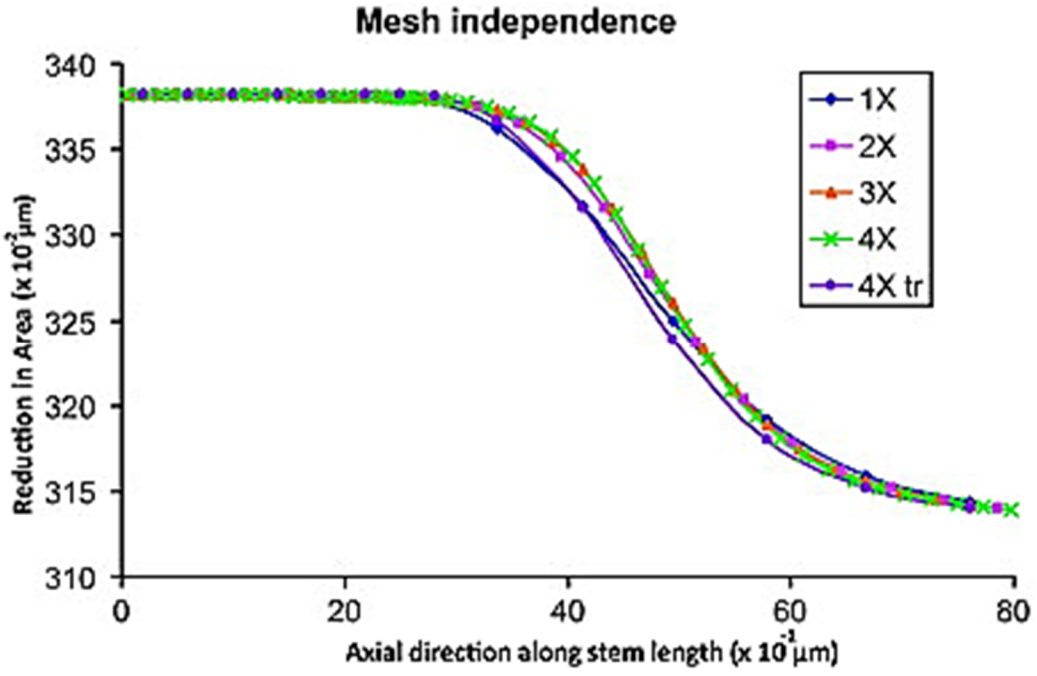

Figure 5-11: Mesh independence study on one of the parameters of interest (reduction in area along stem length)

The 2x refinement ensured that the simulation runs could be managed within a feasible time-scale while maintaining an appreciable level of accuracy in the output data. Two sample runs of the mesh independence study are given in APPENDIX C.

One limitation to the high-aspect ratio feature is the tendency for nearest neighbors to collapse because of interfeature attractive forces. Also the ultimate fracture force of the fibrils decreases as the spheroid diameter decreases, thereby limiting the smallest practical feature size.

CHAPTER 6. ANALYTIC AND NUMERICAL RESULTS AND ANALYSIS

6.1 Quantifying adhesion

For elastic material, as assumed in this research work, adhesion is often described by the critical adhesion energy, *Gc.* This descriptor basically refers to the force for moving a "crack" at an interface and has units of energy/unit area. If the applied driving force is greater than a crucial value (i.e., *Gc*) then the interfacial material will separate [Gorb, 2009]. Once the adhesion energy is known for a given material interface, then some synergetic design parameters such as the maximum sustainable force or stress for a given geometry can be determined. Researchers have used the contact probe adhesion test for patterned and nonpatterened interfaces [Crosby, 2007]. Experiments performed by Crosby quantified adhesion by using a probe testing method in conjunction with theories of contact mechanics (Figure 6-1). The results from this experiment were used to compare the patterned geometries with the simulation runs done during this research.

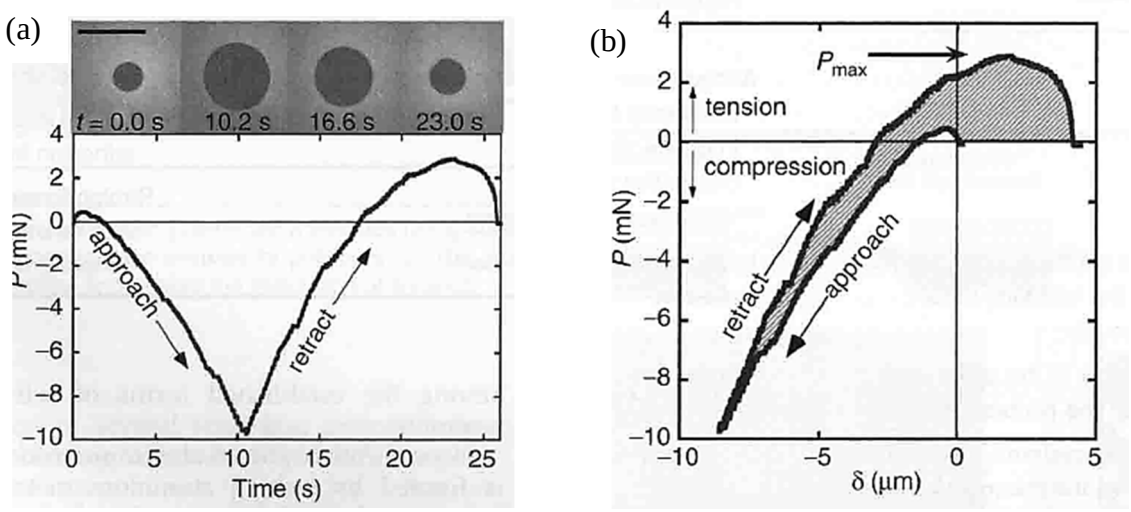

Figure 6-1 : (a) Time history (P vs t) of the adhesion test [Crosby 2007], The dark circle defines the contact area. The scale bar is 500 μm. (b) The results of experimental studies in adhesion summarized by a force-displacement (P-δ) curve

The micromechanism of adhesion in dry adhesion was taken to primarily depend on van der Waals forces between the fine structure and a substratum. When two elastic bodies [Figure 6-2.(a)] are joined together by the van der Waals adhesion and then subjected to an externally pull-off force, stress concentration is expected to occur near the edge of the joint. As the force increases, the intensity of stress concentration ultimately reaches a critical level to drive a crack to propagate and break the joint.

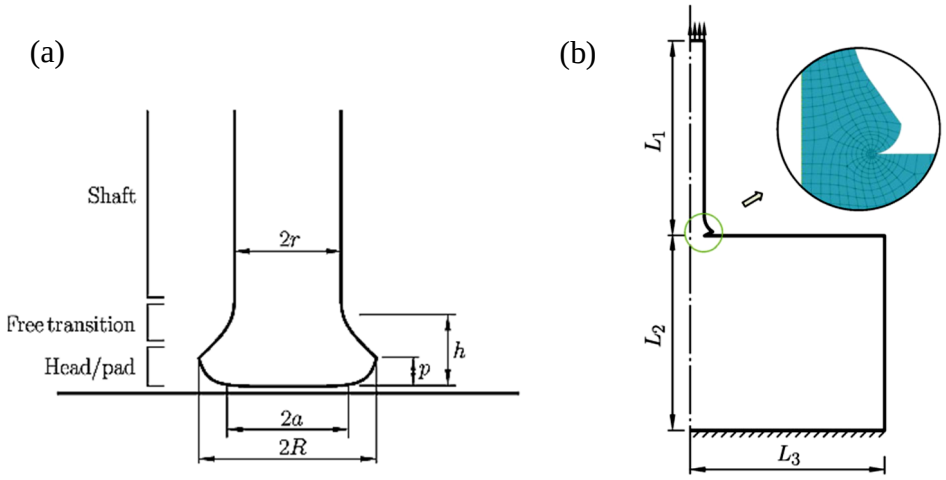

Figure 6-2 : (a) Aspect ratios and geometric features of the modeled mushroom head (b) FEA dimensions and mesh details.

The section of the specimen under inspection during the quantification of *Gc* consists of two parts, as shown in Figure 6-2.(b), the cylindrical substratum and the adhesive structure with a mushroom-like head. The height and the radius of the cylindrical substratum are, respectively, L_2 and L_3. The length of the adhesive structure is L_1. The shaft radius of the adhesive structure is ranging from 100 nm to 200 nm in our calculations. All adhesive structures [as shown in Figure 6-2.(a] have the same head radius, R = 200 nm, and *a* is fixed (equal to 0.7R, about 50% of the actual contact area [Gorb, 2009]). Note that *h* is different for each adhesive structure, and *p* is not an independent variable and linearly depends on *h* in our models. Commercial FEA software

COMSOL, is used here for the analysis. The adhesive structure is jointed with the elastic substratum. And uniform and homogeneous materials are chosen in our analysis. E_{sp} = 200 GPa (Young's modulus of common alloy materials used in TBC coating application) and E_{sub} = 50 GPa (adhesive strength of semi-melted ceramic plating) are respectively taken as the modulus of the bar and the base. Poisson's ratio is 0.3 for both. A typical finite element mesh is shown in Figure 6-2.(b). In our calculations, the smallest element length near the crack tip is about 4 nm, which is nearly 1/35 of the contact radius of 140 nm. In total, four groups of structures are analyzed here based on different thickness of head, which are 30 and 100, 60 and 200, 120 and 400 nm, for h and p, respectively. All structures are loaded by a uniform tension force of 5 nN on the top of the adhesive structure [in Figure 6-2.(b)]. The bottom of the cylindrical substratum is fixed.

A linear elastic analysis is performed in order to simplify the problem, i.e., the stress intensity factor, *K*, is used to evaluate the adhesive capability of the structure. The stress intensity factor is directly calculated by COMSOL via selecting a typical circular integral path around the crack tip. By adjusting the structural characteristic size, we can get a series of *K* to show the influence of the head shape on the adhesive capability of the structure.

6.2 Results

6.2.1 Geometry-based Pull-off Forces

In previous experiments, mushroom-shaped fibrils were often fabricated with a peeling angle $\theta=90^\circ$ to study the adhesion behaviors and to compare the adhesion force with that of other contact shapes [Chen, 2012] . Theoretical models for the adhesion of a mushroom-shaped fibril with $\theta=90^\circ$ were established to attempt to explain the experimental observations. However, the geometrical effects with various parameters of the mushroom shaped fibril on the adhesion

force were not clear so far, which has been investigated systematically in this work to explore the superior adhesion mechanism of such a structure.

The substrate is assumed to be a rigid hemisphere with uniform radius of 10 nm. The four tip shapes are selected as flat punch, spatula tip, mushroom, and sphere, as shown in Figure 6-3.

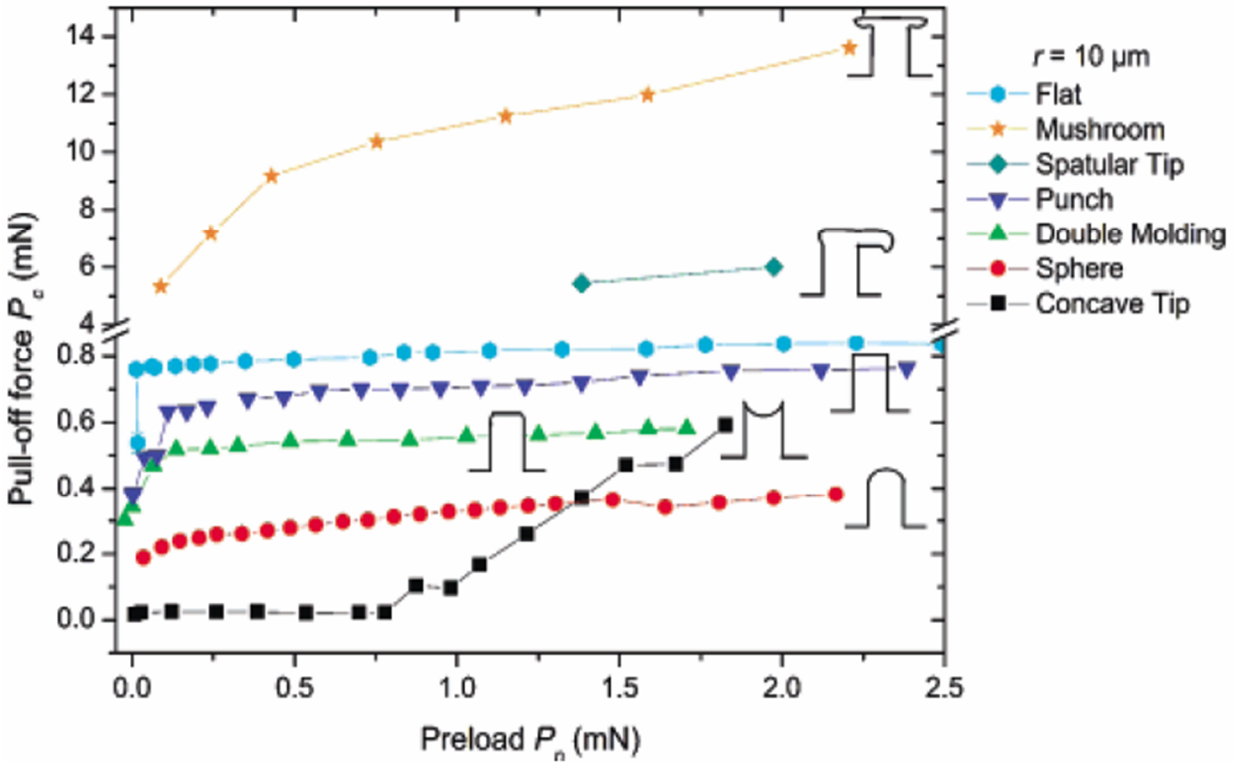

Figure 6-3 : Adhesion force comparison of the four different geometry tips versus pre applied load with experimental values from work by Del Campo [Del Campo, 2007]. Evidently the adhesion forces are dependent on the contact geometry.

Other modeling parameters remain unchanged. The projective radii of the various tips are uniformly selected as 8 nm. To concentrate on the pull-off force of the nano-scale contact, we emulate the detaching process beginning from a preloaded state and then gradually decrease the deformation displacement. The detaching process is kept in equilibrium at every step, so the response normal load, varying contact area, and the resulting pull-off forces are all

recorded step by step. Initially, it was found that the pull-off forces are dependent on the pre-applied load, as shown in Figure 6-3.

The steps involved can be laid out as follows

(i) The pull-off force increases sharply as the pre-applied load increases at a low load range, but approaches a stable value. When the preload is large enough, the pull-off forces are almost independent on the pre-load.

(ii) Different contact geometries result in different pull-off force peaks. The pull-off force of mushroom head shape increases sharply. After a proper pre-load, mushroom shape owns a maximum pull-off force, followed by spatular tip and flat punch, respectively. To reveal the geometry details of the contact area, the varying contact areas including the whole contact area, the sticking area, and the adhesive area are also recorded for the four tip shapes. Figure 6-4 shows the variations of sticking area and adhesive area as the normal load varying from 0 to 20.

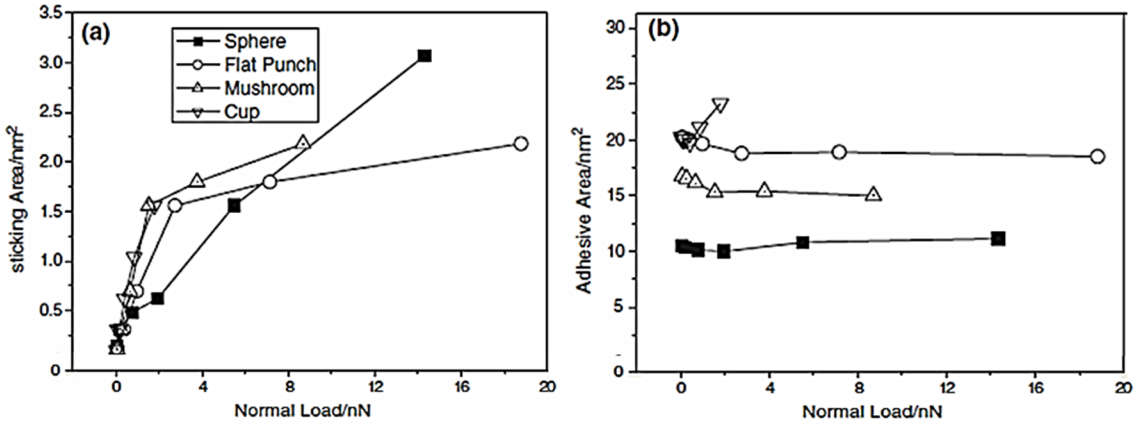

Figure 6-4: Detail of contact area for four different geometry tips. (a) Local sticking areas (b) local adhesive areas

It can be seen that,

(i) Sticking area is very small, almost one order of magnitude smaller than the adhesive area;

(ii) The adhesive area is obviously dominant in the total contact area;

(iii) Sticking area increases with normal load, while the adhesive area is almost kept constant except for the tip of cup shape.

In addition we can also notice the following interesting features:

(i) All the nano tips result in higher adhesive stress as the tip size decreasing to several nanometers.

(ii) As the tip size decreases to several nanometers, the adhesive stress is still geometry sensitive.

(iii) Among the four tip geometries, the mushroom tip has the highest adhesive stress, followed by the spatula tip shape, sphere, and then punch.

Figure 6-5 shows the measured pull-off forces, *Pc*, as functions of preload, *Pp*, for patterns with different tip geometries and radii. For comparison, the values obtained from flat samples, spatula shaped samples and sphere shaped samples are also included [Patano, 2011]. *Pc* measured on flat samples did not vary significantly with preload, as was expected from the Johnson-Kendall-Roberts (JKR) theory [JKR, 1971]. In contrast, *Pc* increased strongly with preload for all patterned surfaces except for the concave tips, until a plateau was reached. Pillars with concave tips behaved differently: starting with a very low adhesion, *Pc* increased with preload and, finally, reached a higher saturation level. The pull-off values for concave tips were significantly below the ones for the other shapes. Patterned surfaces with planar, spherical, mushroom and spatula tip geometries showed increasing *Pc* for decreasing pillar radius at any preload.

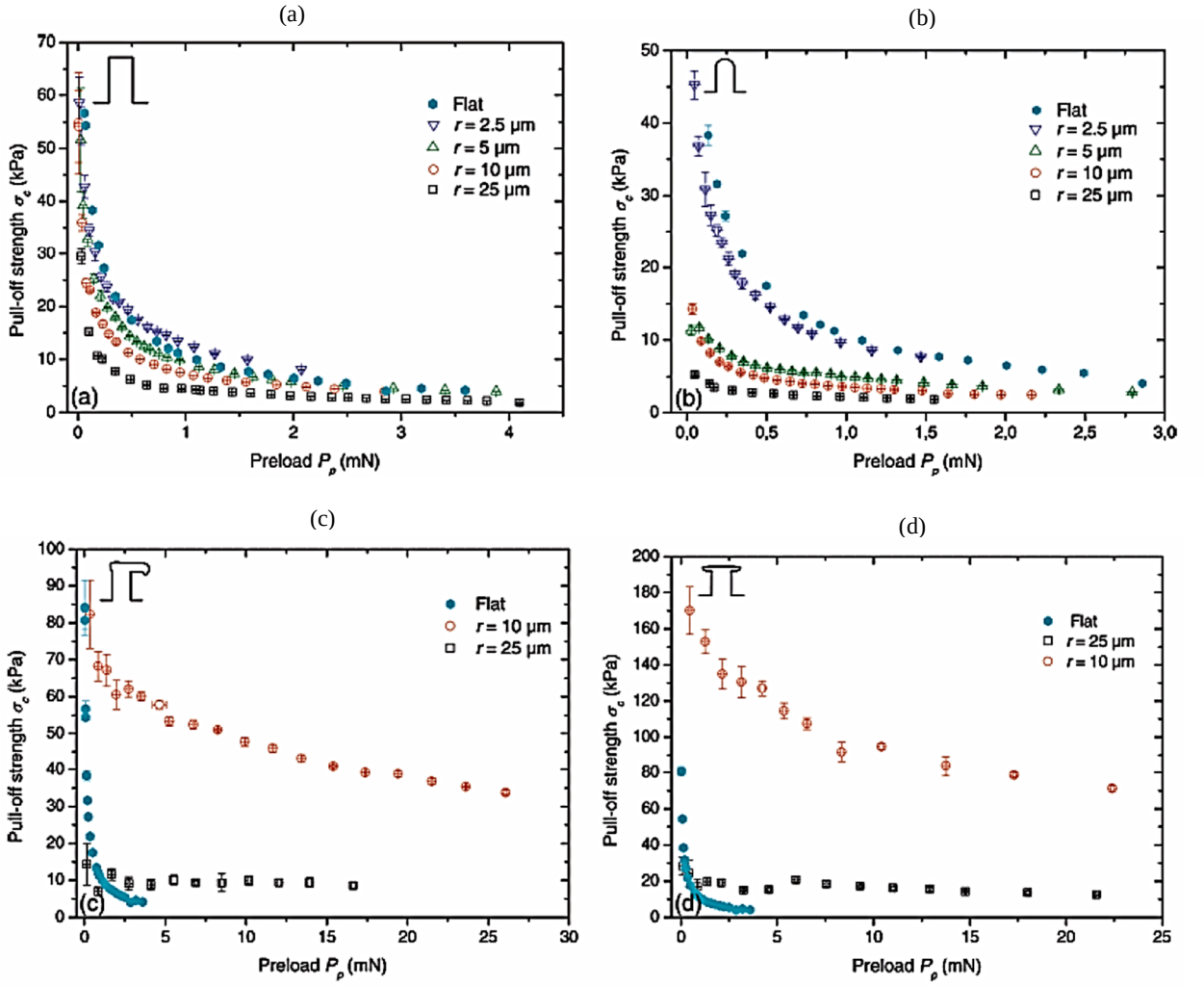

Figure 6-5 : Pull-off force vs preload for different geometries during simulation (a) flat tip (b)spherical tip, (c) spatula tip (d) mushroom like tip. The data for the first two shapes are taken from works by Del Campo [Del Campo, 2007]

This is in agreement with the contact splitting principle [Autumn, 2002]. In the case of tips with rounded edges, a similar tendency was found for pillars with radii 25, 10, and 5 µm; however, *Pc* dropped for patterns with smaller radius (2.5 µm). At low preloads, patterns with concave tip geometry showed very low adhesion independently of the radius. *Pc* started increasing at lower preloads for smaller radii, but reached similar plateau values for all radii. A split contact surface does not seem to favor adhesion for this shape. Comparison with flat controls depends on the contact shape: The pull-off force of patterned surfaces with flat tips

exceeded Pc of the flat surface for r < 5 μm. In the case of mushroom and spatular tips, Pc was much higher than for the flat surface for all measured radii. In contrast, spherical, rounded edge and concave tips showed lower Pc than the flat control substrate. This may be attributed to the loss of actual contact area in patterned cases, which does not seem to be outweighed by the adhesion enhancement due to contact splitting for these geometries. To check whether the high adhesion values of the mushroom-like pillars correlated with the diameter of the mushroom terminal, samples with the same pillar radius but different mushroom tip radii were measured.

Results for the two fabrication methods are represented in Figure 6-5 for pillar radii 25 and 10 μm. No significant difference in the adhesion performance could be detected in samples with differences in the tip diameter of up to 7 μm. A comparison of pull-off force vs preload for pillars with different tip shapes but the same radius and height is given in Figure 6-5. Large Pc values were found for mushroom and spatula tips in comparison with all other geometries (note that the Pc axis is split). The following ranking of adhesive performance for the different tip geometries can be extracted: mushroom tips are far superior, followed by spatula tips; flat tips have considerably weaker adhesion, but are stronger than flat tip with rounded edge, spherical and concave tip. A more meaningful parameter to compare adhesion performance is given by the pull-off strength, σ_c, which is obtained by dividing Pc by the apparent contact area. This area is different for each preload value and can be calculated from the experimental indentation depth by simple geometrical considerations as σa^2, where a is the radius of contact for the sphere with the substrate at maximum preload. Figure 6-5.(a-d) shows how σc decreases with increasing preload in all cases except for pillars with concave geometry, which show a small increase in σ_c with preload.

6.2.2 Compressive Behavior

The compressive parts of the L-δ curves were further analyzed by applying the Hertz theory of elastic contact, neglecting the fibrillar nature of the surfaces. An effective Young's modulus $E^*=E/(1-\nu^2)$ was assume, where $\nu=0.5$ is the Poisson's ratio was obtained by fitting the experimental data to the expression developed by Del Campo [Del Campo, 2007] :

$$P = \frac{4}{3} E^* \sqrt{R\delta^3} \qquad \text{.....(21)}$$

where P is the applied compressive force/load, R is the radius of the indenting sphere in their experiment and δ is the indentation depth. It was found that for a given radius, pillars with flat, spherical and rounded edge tips gave similar results, pillars with concave tips showed much lower E*, by up to a factor of ½ ; presumably as a consequence of the thin, flexible tip walls. Surfaces with mushroom and spatula tips had significantly higher values by a factor of 2-3.

6.2.3 Effect of Young's Modulus

It is known that when the material's Young's Modulus is below 100 kPa, the adhesive structure will achieve a high contact fraction with substratum and thus have an ideal adhesive capability [Li, 2010]. The effect of contact area division and high aspect ratio in the Gecko setae make the adhesive elastic modulus of the setae close to this limit. Here, in this research, the effect of Young's modulus on the adhesive capability of a single adhesive structure was also investigated.

It is seen from Figure 6-6.(a) that when the modulus is smaller than 2GPa, the adhesive force of the structure is reduced significantly (the corresponding K is increased) with an increase in the

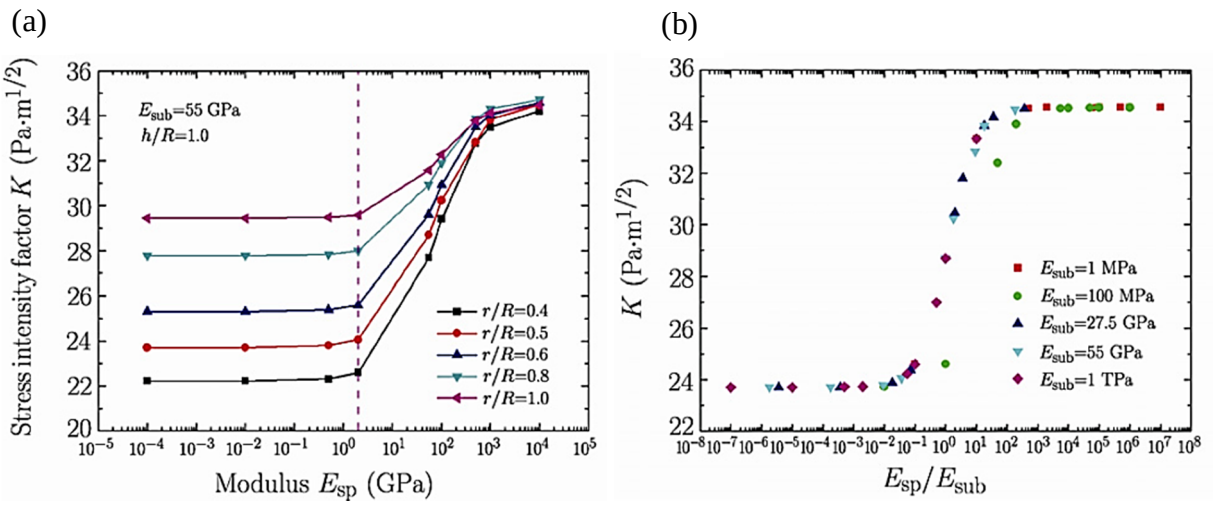

Figure 6-6 : (a) The effect of modulus of adhesive structures on the stress intensity factor vs the shaft radius, (b) The effect of the modulus ratio on the stress intensity factor for a typical r/R=0.5 and h/R=1.0.

elastic modulus when the modulus is larger than 2GPa. We also saw that the lower the elastic modulus the stronger the effect of the head shape.

It is of particular interest to see that when the elastic modulus of the adhesive structure is very large, the adhesive force is insensitive to the shape of its head. This explains why the synthetic adhesive structures of different carbon nanotubes (with an elastic modulus of about 1TPa) have almost the same normal adhesive force under the same loading condition.

To further understand the effect of elastic modulus on the adhesive capability, we show in Figure 6-6.(b) the stress intensity factor versus the head-to-substratum modulus ratio. It was found that almost all data points fall onto a unique curve, indicating the stress intenstity factor is a function of the ratio of the two moduli. Since the modulus of the substratum E^{sub} that the aforementioned animals are attached to is about several tens of GPa in general, our finding shows that an optimum modulus for the adhesive structure (E^{sp}) is about 1-2 GPa. This may explain why the modulus of almost all biological adhesion structure is approximately equal to

2GPa (the vertical dash line in Figure 6-6.(a). It is the result of natural evolution and our simulation also shows this value to be perfectly catered to our need.

CHAPTER 7. CONCLUSION AND FUTURE WORKS

7.1 Outro

Throughout this research, a comprehensive study was done on the adhesion phenomena in thermal barrier coatings. This was done using both experimental observation and numerical simulations. The process involved a segmented methodology that can be ruminated into the following workflow shown in Figure 7-1:

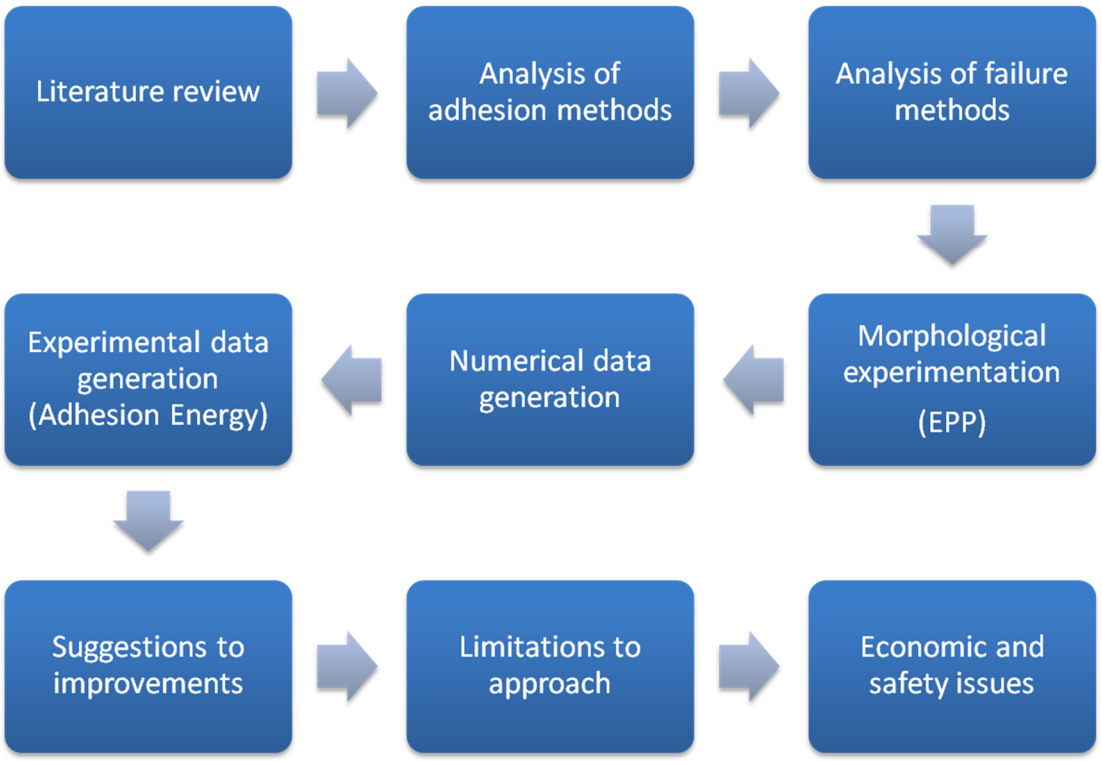

Figure 7-1 : Research workflow

It was observed that during the EPP process the chamber pressure, the pressure ratio, the substrate temperature and the YSZ evaporation rate all strongly affected the observed coating morphology. From this work several specific conclusions can be drawn:

- Adhesion is an imperative catalyst in the durability of thermal barrier coatings and mechanical adhesion mechanisms can provide a strong uplift in the protection of TBCs from spallation and debonding failures.
- TBC technologies have received very little attention in the fields of morphological changes for adhesion improvements. So much research work can be invested in strengthening this aspect.
- Morphological observations were made and the results obtained from the SEM micrographs clearly show the effect of process parameters like external pressure on the EPP process and the subsequent morphological changes in the sample. Thus it can be quantified that we can achieve desirable surface morphologies by changing the different process parameters of EPP.
- Electrolytic Plasma Processing is a novel technology that can be investigated to bring about useful morphological and micro/nano level changes to the geometry of the bond coat surface.

A numerical modeling method was proposed by drawing an analogy between biologically adhesive, fibrilar, 'mushroom head' geometries and the spheroidal micro features on an EPP treated surface. A method to quantify the adhesion strength, numerically, from this modeling was also proposed.

- Due to the lack of a physical method to measure the profiles on the EPP treated surfaces; a method based on optical contour recognition was adopted. Although this would inevitably introduce some level of scaling error, the literature [Celltracer manual, Wang 2008] suggested that this method should be good enough for a first order approximation.

- The cell tracer algorithm was used to model the unique geometry observed in EPP treated surfaces. The generated geometry was then used to run adhesion energy tests on a software based OSE (Operational Simulation Environment). The final stage of the work involved comparison between the virtual adhesion tests performed on the different geometries.

From the simulation results obtained, it can be deduced that the unique geometry generated by EPP process was indeed beneficial for adhesion. The improvement in pull off force in case of 'mushroom heads' as compared to other patterns was almost 10 folds. Atleast, as long as the congruity of the aspect ratio of these mushroom heads can be maintained, the adhesion improvement should persist.

It can also be commented from literatures on Bio-Mimetics and Bio-Adhesion that the effect of geometry, not surface chemistry, is the central design principle in the evolution of adhesive setae [Autumn, 2002]. There is a striking semblance between the JKR theory of dry, Van Der Waahls adhesion in close proximity of micro/nano structures and the geometrically complex structures evolved by Gecko like animals. It is remarkable however that this research work was able to somewhat approximated the function of the setae tip and tie it to a process of artificial synthesis. This indicates that the simple, underlying design principles and not the actual setae themselves are the empowering factors behind enhanced adhesion.

7.2 Future Works

Although extreme care was taken to ensure the validity and applicability of the findings of this research, it would be absurd to imagine that all the findings can be adopted into a real life scenario verbatim et literatim. For example, significant simplification assumptions were made to

ensure convergence of simulation runs and to obtain a congruent result with acceptable levels of error. The calculations were based on a linear elastic analysis. So any future work that wants to build upon the findings of this research should take into consideration the viscoelastic nature of biomaterials. Furthermore the linear elastic model does not take into consideration the adhesion parameters that are governed by a non-linear, power law relation.

Also, it was investigated the Young's modulus might have a significant effect on the adhesion capability of the structures when the ratio of the modulus of the adhesive structure to the modulus of the substratum is ranging from 0.03 to 20. However, an inquiry wasn't made about the effect of other modulus of materials (like the Poisson's ratio) and the extensive properties that sometimes affect the material behavior in micro/nano scale.

Although the Lennadrd-Jones potential based FE modeling was employed for the analysis, some literature suggests [Zhang, 2010] that the assumption of equivalent radius may only be valid for Hertz contact without interfacial forces and becomes invalid for nano-scale adhesive contact when the distribution variation of surfaces forces caused by the varying clearance and deformation becomes prominent. However, local geometry was not deemed that important in this research work. Any future work would have to take into account this fact and build on it accordingly.

In relevant research in the fields of Bio-Adhesion, contact splitting and lithograph patterning play an important role. Patterned elastomeric attachment surfaces with widely different tip shapes can be produced reproducibly using variations of lithography and soft-molding methods for industrial application. The same is applicable in case of contact splitting, where adhesion is interdependent on a term called "splitting efficiency" where the newly split

surfaces resemble their mother shapes even after the split. So it is evident that further research is needed to explain the outstanding performance of the mushroom shaped ends on adhesion. Perhaps integration of ideas such as capillary forces is a good way to reproach the problem. Such effects should be the focus of future studies.

REFERENCES

Autumn, K., M. Sitti, Y. A. Liang, A. M. Peattie, W. R. Hansen, S. Sponberg, T. W. Kenny, *et al.* "Evidence for Van Der Waals Adhesion in Gecko Setae." [In eng]. *Proc Natl Acad Sci U S A* 99, no. 19 (Sep 17 2002): 12252-6.

Bhushan, Bharat. "Nature's Nanotechnology: As Engineers Uncover the Secrets of Some of Nature's Most Amazing Materials, They've Found Some Startling Similarities between Surfaces That Act Radically Different." *Mechanical Engineering-CIME*, 2012/12// 2012, 28+.

Chan, E. P., C. Greiner, E. Arzt, and A. J. Crosby. "Designing Model Systems for Enhanced Adhesion." [In English]. *MRS Bulletin* 32, no. 6 (Jun 2007): 496-503.

Cionea, Cristian. "Microstructural of Surface Layers During Eletrolyti Plasma Processing." *Dissertation in Defence of Doctoral Degree in University of Texas at Arlington* (2010).

Dai, ZhenDong, and Stanislav Gorb. "Contact Mechanics of Pad of Grasshopper (Insecta: Orthoptera) by Finite Element Methods." *Chinese Science Bulletin* 54, no. 4 (2009): 549-55.

Del Campo, A., C. Greiner, and E. Arzt. "Contact Shape Controls Adhesion of Bioinspired Fibrillar Surfaces." [In eng]. *Langmuir* 23, no. 20 (Sep 25 2007): 10235-43.

E.I. Meletis, X. Nie, , F.L. Wang, J.C. Jiang. "Electrolytic Plasma Processing for Cleaning and Metal-Coating of Steel Surfaces." *Surface and Coatings Technology* (2002): 246-56.

Ensikat, Hans J., Petra Ditsche-Kuru, Christoph Neinhuis, and Wilhelm Barthlott. "Superhydrophobicity in Perfection: The Outstanding Properties of the Lotus Leaf." *Beilstein Journal of Nanotechnology* 2 (2011): 152-61.

Guilin Li, Tienchong Chang. "Effect of Head Shape on the Adhesion Capability of Mushroom-Like Biological Adhesive Structures." *Acta Mechanica Solida Sinica* 24, no. 4 (2011): 320-25.

H. Kurzwez, R. B. Heimann. "Adhesion of Thermally Sprayed Hyrdoxyapatite Bond Coat Systems." *Journnal of Material Science: Materials in Medicine* (1998): 9-16.

Hu, S., H. Jiang, Z. Xia, and X. Gao. "Friction and Adhesion of Hierarchical Carbon Nanotube Structures for Biomimetic Dry Adhesives: Multiscale Modeling." [In eng]. *ACS Appl Mater Interfaces* 2, no. 9 (Sep 2010): 2570-8.

Jagota, Anand, and Chung-Yuen Hui. "Adhesion, Friction, and Compliance of Bio-Mimetic and Bio-Inspired Structured Interfaces." *Materials Science and Engineering: R: Reports* (2011).

K. L. Johnson, K. Kendall, A. D. Roberts. "Surface Energy and the Contact of Elastic Solids." *Proceedings of The Royal Society A: Mathematical, Physical and Engineering Sciences* 324 (1971): 301-13.

Kang, K. J., J. W. Hutchinson, and A. G. Evans. "Measurement of the Strains Induced Upon Thermal Oxidation of an Alumina-Forming Alloy." *Acta Materialia* 51, no. 5 (2003): 1283-91.

Kim, Won-Seock, Il-Han Yun, Jung-Ju Lee, and Hee-Tae Jung. "Evaluation of Mechanical Interlock Effect on Adhesion Strength of Polymer–Metal Interfaces Using Micro-Patterned Surface Topography." *International Journal of Adhesion and Adhesives* 30, no. 6 (2010): 408-17.

Pantano, Antonio, Nicola M. Pugno, and Stanislav N. Gorb. "Numerical Simulations Demonstrate That the Double Tapering of the Spatualae of Lizards and Insects Maximize Both Detachment Resistance and Stability." *International Journal of Fracture* 171, no. 2 (2011): 169-75.

Peng, Zhilong, and Shaohua Chen. "The Effect of Geometry on the Adhesive Behavior of Bio-Inspired Fibrils." *Soft Matter* 8, no. 38 (2012): 9864.

Théry, P. Y., M. Poulain, M. Dupeux, and M. Braccini. "Adhesion Energy of a Ypsz Eb-Pvd Layer in Two Thermal Barrier Coating Systems." *Surface and Coatings Technology* 202, no. 4-7 (2007): 648-52.

Varenberg, M., A. Peressadko, S. Gorb, and E. Arzt. "Effect of Real Contact Geometry on Adhesion." *Applied Physics Letters* 89, no. 12 (2006): 121905.

S. Bose and J. DeMasi-Marcin, , ―*Thermal Barrier Coating Experience in Gas Turbine Engines* at Pratt & Whitney, Journal of Thermal Spray Technology, 6(1) (1997) pp. 99-104

Marot, G., J. Lesage, P. Demarecaux, M. Hadad, S. Siegmann, and M. Staia. "Interfacial Indentation and Shear Tests to Determine the Adhesion of Thermal Spray Coatings." *Surface and Coatings Technology* 201.5 (2006): 2080-085

Packham, D. "Work of Adhesion: Contact Angles and Contact Mechanics." *International Journal of Adhesion and Adhesives* 16.2 (1996): 121-28.

Weiss, H. "Adhesion of Advanced Overlay Coatings: Mechanisms and Quantitative Assessment." Surface and Coatings Technology 71.2 (1995): 201-07.

The United States of America. National Aeronautics and Space Administration NASA. *Thermal Barrier Coatings for Gas Turbine and Diesel Engines*. By Robert A. Miller, William J. Brindley, and Murray M. Bailey. Springfield: National Technical Information, 1989. Print.

The United States of America. National Aeronautics and Space Administration. *History of Thermal Barrier Coatings for Gas Turbine Engines*. By Robert A. Miller. Cleveland: National Technical Information Service, 2007. Print.

Cheng, Y. S., W. H. Doglas, A. Versluis, and D. Tantbirojn. "Analytical Study on a New Bond Test Method for Measuring Adhesion." *Engineering Fracture Mechanics* 64 (1999): 117-23.

Barnes, Dunstan, Scott Johnson, Robert Snell, and Serena Best. "Using Scratch Testing to Measure the Adhesion Strength of Calcium Phosphate Coatings Applied to Poly(carbonate

Urethane) Substrates." *Journal of the Mechanical Behavior of Biomedical Materials"*(2012): 128-38.

Meletis EI, Nie X,Wang FL,Jiang JC. Electrolytic plasma processing for cleaning and metal-coating of steel surfaces. Surface and Coatings Technology 2002, 150, 246–256.

Kenny, Thomas. "The Science of Motion." *PolyPEDAL Lab.* UC Berkeley, n.d. Web. Fall 2012.

Yerokhin, A.L., Nie, X., Leyland, A., Matthews, D.S.J., 1999, 'Plasma electrolysis for surface engineering', Surface & Coatings Technology, vol. 122, no. 2-3, pp 73-93.

Sengupta, S.K., Singh, O.P., 1991, 'Contact glow discharge electrolysis: a study of its onset and location',Journal of Electroanalytical Chemistry, vol. 301, no. 1-2, pp 189-197.

Liang, Jiandong, and Hossain I. Naser. "Improvement of Corrosion Resistance on a Low Carbon Steel 1018 in 3.5% NaCl Solution by Electrolytic-Plasma-Process (EPP)."*ASME 2012 International Mechanical Engineering Congress & Exposition 2012, Houston, Texas, USA* (2012): 145-60.

Wang, Quanli. "*CellTracer: Software for Image Segmentation and Lineage Mapping for Single-cell Studies Modelling.*" Duke University & NSF, June-July 2008. Web.

A.A. Griffith, Phil. Trans. R. Soc. London A 221 (1921) 163.

Packham, D. "Work of Adhesion: Contact Angles and Contact Mechanics." International Journal of Adhesion and Adhesives 16.2 (1996): 121-28.

Christensen, Asbjorn, Emily A. Asche, and Emily A. Carter. "Atomic-Level Properties of Thermal Barrier Coatings: Characterization of Metal Ceramic Interfaces." (1998): 101-60.

Jones, T. W., and P. J. Kellogg. "Plasma Waves Artificially Induced in the Ionosphere." Journal of Geophysical Research 78.13 (1973): 2166-175.

Kurzweg, H., R. B. Heimann, and T. Troczynski. "Adhesion of Thermally Sprayed Hydroxyapatite-bond-coat Systems Measured by a Novel Peel Test." Journal of Materials Science: Materials in Medicine 9.1998 (1998): 9-16. Print.

Lima, C., and J. Guilemany. "Adhesion Improvements of Thermal Barrier Coatings with HVOF Thermally Sprayed Bond Coats." Surface and Coatings Technology 201.8 (2007): 4694-701.

Shull, Kenneth R. "Contact Mechanics and the Adhesion of Soft Solids." Materials Science and Engineering: Reports 36.1 (2002): 1-45.

Vasimonta, A., and J. L. Beuth. "Measurement of Interfacial Toughness in Thermal Barrier Coating Systems by Indentation." Engineering Fracture Mechanics 68 (2001): 843-60.

Sluginov NP. Electric discharges in water. J Russ Phys Chem Soc. 1980;12(12):193.

APPENDIX A: CELL TRACER EDGE CONTOURING ALGORITHM

getImages.m

```
function [numframes statustext] =
getImages(filename,pathname,outputpath,h)
    ghandles = guidata(h);
    if iscell(filename)
        frames  = length(filename);
    else
        frames = 1;
        filename = cellstr(filename);
    end
    channel = 0;
    ax1 = subplot('position',[0.005, 0.20, 0.375 0.9]);
    ax2 = subplot('position',[0.385, 0.20, 0.375 0.9]);
    try
        img = imread([pathname,char(filename)]);
        if length(size(img)) == 3
            ax1 = getAxes(gcf,1);subplot(ax1);
            imshow(img,[]);
            channel = selectChannel();
        end
    catch
        im = {};
        statustext = ['Reading image files ... failed'];
    end
    if ~exist(outputpath,'dir')
        mkdir(outputpath);
    end
    mmin = []; mmax = [];
    currentpath = pwd;
    try
        for frame = 1: frames
            img = imread([pathname,char(filename{frame})]);
            if channel == 0 %single channel
                %do nothing
            elseif channel >3 %rgb to grey
                img = rgb2gray(img);
            else
                img = img(:,:,channel);
            end
            if isempty(mmin)
                mmin = min(img(:)); mmax = max(img(:));
            else
                mmin = min(mmin,min(img(:)));
                mmax = max(mmax,max(img(:)));
```

```
            end
            ax1 = getAxes(gcf,1);subplot(ax1);
            imshow(img,[]); pause(0.1);
            ax2 = getAxes(gcf, 2);subplot(ax2);
            temp = uint8(img(:,:,1)<0)*255;
            imshow(temp);
            linkaxes([ax1 ax2]);
            data.source = char(filename{frame});
            data.tag = 'input';
            data.im = img;
            data.mask = [];
            cd(outputpath);
            matfile = [data.source,'.mat'];
            views{1} = data;
            save(matfile, 'views');
            cd(currentpath);
        end
        cd(outputpath);
        for frame = 1: frames
            matfile = [char(filename{frame}),'.mat'];
            load(matfile);
            data = views{1};
            temp = uint8((double(data.im) - double(mmin)) /
double(mmax - mmin) * 255.0); temp(temp==0) = 1;
            data.im = temp;
            views{1} = data;
            save(matfile, 'views');
            %im{frame}.raw = temp;
        end
        cd(currentpath);
        statustext = ['Reading image files ... done. Total number of
images: ', num2str(frames)];
        numframes = frames;
    catch
        %im = {};
        numframes = 0;
        cd(currentpath);
        filename(frame,:);
        statustext = ['Reading image files ... failed to read file:
',filename{frame}];
    end
    guidata(h,ghandles);
function result = selectChannel()
    str = {'Red','Green','Blue','Gray'};
    [s,v] = listdlg('PromptString','Select a channel:',...
                'SelectionMode','single',...
                'ListString',str,...
                'InitialValue',1,...
                'Name', 'Channel Selection',...
                'ListSize',[200 80]);
    if isempty(s)
        s = 1;
```

```
    end
result = s;
```

CTTracking.m

```
function [forwardscores,backwardscores] = CTTracking(labels1,
labels2,alignment, para)
n1 = para{1};n2 = para{2};n3 = para{3};t1 = para{4};

[r1 c1] = find(labels1>0);
rmax= max(r1); rmin = min(r1);
cmax= max(c1); cmin = min(c1);
a = labels1; a = a(rmin:rmax,cmin:cmax);
neighbours{1} = GetNeighbours(a,n1,n2,3);

[r2 c2] = find(labels2>0);
rmax= max(r2); rmin = min(r2);
cmax= max(c2); cmin = min(c2);
a = labels2; a = a(rmin:rmax,cmin:cmax);
neighbours{2} = GetNeighbours(a,n1,n2,3);
rmax= max([max(r1) max(r2)]); rmin = min([min(r1) min(r2)]);
cmax= max([max(c1) max(c2)]); cmin = min([min(c1) min(c2)]);
a = labels1; a = a(rmin:rmax,cmin:cmax);
b = labels2; b = b(rmin:rmax,cmin:cmax);
if ~isempty(alignment)
    [a b] = CTshowGlobalAlignment(a,b,alignment,0);
end
method = -3; %back compatibility, all dataanalysis prior to March
21st, 2008 use default value -3
links =
CTcorrespondence(method,a,b,neighbours{1},neighbours{2},n3,1,t1,0);
[newf newb] = CTresolveCorrespondence(links(:,:,1),links(:,:,2)');
forwardscores = newf;
backwardscores = newb;
```

CTAutopartion.m

```
function CTautoPartition()
h = gcf;
handles = guidata(h);
%frame= get(handles.FrameIndex,'String'); frame = str2num(frame);
[im mask] = getCurrentImage(h,[]);

if 0> 1
    minsize = 50; maxsize = minsize * 1000; disk = 1; conn = 4;limit =
[30 200];
    if isempty(mask)
```

```
        %msgbox('Manually select some objects first');
    else
        cells = mask(:,:,3);
        temp = CTiterativeApply(double(cells),0, 4,{@(x) double(x>0).*
length(x(x>0))}, []);
        temp = unique(temp(:)); temp = temp(temp>0);
        if isempty(temp)
             %msgbox('Manually select some cells first');

        else
            minsize = temp(1) * 0.5;
            maxsize = temp(end) * 10;
        end

    end
else
    para = CTgetParameters;
    maxsize = para.maxcellvolume;
    minsize = para.mincellvolume;
    disk = para.diskradius;
    conn = 4;
    limit(1) = para.minintensity;
    limit(2) = para.cellentranceintensity;
    limit(3) = para.cellexitintensity;
    limit(4) = para.maxintensity;
end
updateMenuStatus();
a = CTScreen(im,maxsize,minsize,disk,conn,limit,[],[],[]);
guidata(gcf,handles);
```

CTborder.m

```
function bordermask = CTborder1(im,mask,para,debug)
cminmax = ones(size(im));
cmaxmin = zeros(size(im));
for ballsize = 1:para{4}
    se = strel('disk',ballsize);
    erange(:,:,1) = imdilate(im,se);
    erange(:,:,2) = imerode(im,se);
    temp = double(erange(:,:,1) - erange(:,:,2));

    temp2 = double(im - erange(:,:,2));
    temp2(temp>0) = temp2(temp>0) ./ temp(temp>0);
    cminmax = min(cminmax,temp2);

     temp2 = double(erange(:,:,1)-im);
     temp2(temp>0) = temp2(temp>0) ./ temp(temp>0);
     cmaxmin = max(temp2,cmaxmin);
end
```

```
%deal with the flat regions
temp = cmaxmin + cminmax;
temp1 = cminmax == 1 | temp == 0;
temp2 = temp ==0;
temp = imreconstruct(temp2,temp1,8);
cminmax(temp>0) = 1.0;

if debug > 0
    figure(100),imshow(cminmax,[]);
    %figure(101),imshow(cmaxmin,[]);
end

bordermask  = cminmax>=para{1};
highbordermask = cminmax >= max(para{3},para{1});
if ~isempty(mask)
    bordermask(mask(:,:,1) > 0) = 1;
    bordermask(mask(:,:,2) > 0) = 0;
    bordermask(mask(:,:,3) > 0) = 0;
    highbordermask(mask(:,:,1) > 0) = 1;
    highbordermask(mask(:,:,2) > 0) = 0;
    highbordermask(mask(:,:,3) > 0) = 0;
end
if para{2} >1
    highbordermask = bwareaopen(highbordermask,para{2});
end
bordermask = imreconstruct(highbordermask, bordermask,8);
```

CTCount.m

```
function result = CTcounts(x,v,para)
t1 = length(find(x<para{1}));
t2 = length(find(x>para{2}));
if t2 ==0
    result = -1;
else
    result = t1 / t2;
end
result(result == -1) = max(result(:));
```

CTSplit,m

```
function [result,newborder] = CTsplit1(im)
im_backup = im;
D = bwdist(~im);
maxsize = max(D(:));
temp=D(D>0);minsize= min(temp);
split = 1;
while split<2 && minsize < maxsize
    im = im_backup;
```

```
    im(D <= minsize) = 0;
    [L split] = bwlabel(im);
    temp = temp(temp>minsize);
    if length(temp) > 0
        temp = temp(temp>minsize);
        minsize =min(temp);
    else
        minsize = maxsize;
    end
end
im = uint8(bwmorph(im,'thicken',Inf));
im(im_backup == 0) = 0;
result = im;
newborder = im_backup; newborder(im>0) = 0;
```

Getflag.m

```
function flag = GetFlag(center,deg)
try
    [x y] = find(center == 1);

    if deg == 1
        X = [ones(length(x),1) x];
        Y = [ones(length(y),1) y];
    elseif deg==2
        X = [ones(length(x),1) x x.*x];
        Y = [ones(length(y),1) y y.*y];
    else
        %flag/score the current object
        X = [ones(length(x),1) x x.*x x.*x.*x];
        Y = [ones(length(y),1) y y.*y y.*y.*y];
    end
    [yb,bint,yr,yrint,ystats] = regress(y,X);
    [xb,xbint,xr,xrint,xstats] = regress(x,Y);

    flag = min(xstats(4),ystats(4));
catch
    flag = 0.1;
end
```

CTiterativeApply.m

```
function result = CTiterativeApply(im,ballsize,connection,method,para)
mask = im > 0; L = bwlabel(mask,connection); s = regionprops(L,
'Image','BoundingBox');
for k = 1:numel(s)
    bb = uint32(s(k).BoundingBox);
    a = im(bb(2):bb(2)+bb(4)-1,bb(1):bb(1)+bb(3)-1); img = a;
    a(~s(k).Image) = 0; img(a>0) = 0;
    %figure(101),imshow(a);
```

```
    b = a;
    if ballsize > 0
        t = CTblock(b,[],[],ballsize,method,para);
        t = uint8(t * 255);
        t(t==0 & b>0) = 1;
    else
        if ~isempty(para)
            t = method{1}(b,para);
        else
            t = method{1}(b);
        end
    end
    img = img+t;
    im(bb(2):bb(2)+bb(4)-1,bb(1):bb(1)+bb(3)-1) = img;
end

result = im;
```

CTiterativeSelectiveSegementation.m

```
function result =
CTiterativeSelectiveSegmentation(im,inputmask,para,debug)
cellscore = para{1};
minvolume = para{2};
disk = para{3};
distancepercentile = para{4};
imold = im;
if ~isempty(inputmask)
    im(inputmask(:,:,1) > 0) = 0;
    im(inputmask(:,:,2) > 0) = 0;
    im(inputmask(:,:,3) > 0) = 0;
end
mask = im > 0;
if disk > 0
   mask = imopen(mask,strel('disk',disk));
end
if minvolume > 0
    mask = bwareaopen(mask,minvolume);
    result(mask==0) = 0;
end
mask = imfill(mask,'holes');
im(mask==0) = 0;

L = bwlabel(mask); s = regionprops(L,
'Image','BoundingBox','Solidity','ConvexArea','Area','perimeter');
for k = 1:numel(s)
    k;
```

```
    bb = uint16(s(k).BoundingBox);
    a = im(bb(2):bb(2)+bb(4)-1,bb(1):bb(1)+bb(3)-1); img = a;
    a(~s(k).Image) = 0; img(a>0) = 0;
    temp = (s(k).ConvexArea - s(k).Area) / s(k).Perimeter;
    flag = temp;

    if flag > cellscore
        if debug > 0
            figure(101),imshow(a); title([num2str(flag),'     ',
num2str(temp)]);
            %pause
        end
        b = a;
        abackup =a;
        if minvolume >0
            [dummy newborder]=CTsplit3(b,disk,minvolume);
        elseif minvolume <0
            [dummy newborder]=CTsplit1(b);
        else
            [dummy newborder]=CTsplit2(b);
        end
        b(newborder>0) = 0;
        if disk >0
            smoothed = CTiterativeOpen(b, disk,1);
            smoothed =
CTdistanceSmooth(smoothed,disk,distancepercentile,debug);
        else
            smoothed = b;
        end
        b(a>0 & smoothed == 0) = 0;
        %restore
        c = b; c(c>0) = 255;
        if disk >0
            c = uint8(bwmorph(c,'thicken',disk * 2)); c(c>0) = 255;
        end
        a(a>0 & c==0) = 0;

        if sum(sum(abackup-a))>0
            a =CTiterativeSelectiveSegmentation(a,[],para,debug);
        end


        img = img+a;
        im(bb(2):bb(2)+bb(4)-1,bb(1):bb(1)+bb(3)-1) = img;
    end
end

result = im;
if ~isempty(inputmask)
    temp = inputmask(:,:,3);
    if any(temp>0)
        temp = imdilate(temp,strel('disk',1));
```

```
        result(temp>0) = 0;
        result(inputmask(:,:,3)>0) = imold(inputmask(:,:,3)>0);
    end
end
if debug > 0
    figure(101),imshow(result)
end
```

CTAssignlinkcolor.m

```
function result = CTassignLinkColor(clink, ccolor)
[ti tj] = find(clink ~= 0);
uti = unique(ti);
count = 0;
result = [];
for i = 1 : length(uti)
    if isempty(ccolor)
        c = uint8(rand(1,3)*255);
    else
        iindex = find(ccolor{1}(:,1) == uti(i));
        if isempty(iindex)
            c = uint8(rand(1,3)*255);
        else
            c = ccolor{1}(iindex(1),2:4);
        end
    end
    result{1}(i,:) = [uti(i) c];
    jindex = find(ti == uti(i));
    for j = 1: length(jindex)
        count = count + 1;
        result{2}(count,:) = [tj(jindex(j)) c];
    end
end
```

APPENDIX B: MECHANICAL AND THERMAL PROPERTIES OF SOME TBCS

Mechanical & Thermal Properties	Units	Al_2O_3 (Coors AD-99.5)	MSZ (3 wt.% MgO)	YSZ (~ 8 wt.% Y_2O_3)	YSZ (>12 wt.% Y_2O_3)
Density	g/cm^3	3.89	5.75	6.02	5.6
Elastic Mod.	GPa	372	200	200	173
Compressive Strength	MPa	2620	1750	N/A	N/A
Thermal Conductivity	W/m-°K	35.6	2.2	2.2	2.2
CTE	10^{-6}/°C	8.2	10.1	10.3	10.5
Specific Heat	J/kg-°K	880	486		
Thermal Shock Resistance	°C	200	350	350	150
Max. Use Temp.	°C	1750	500	2400	2400

APPENDIX C: MESH REFINEMENT AND VALIDATION

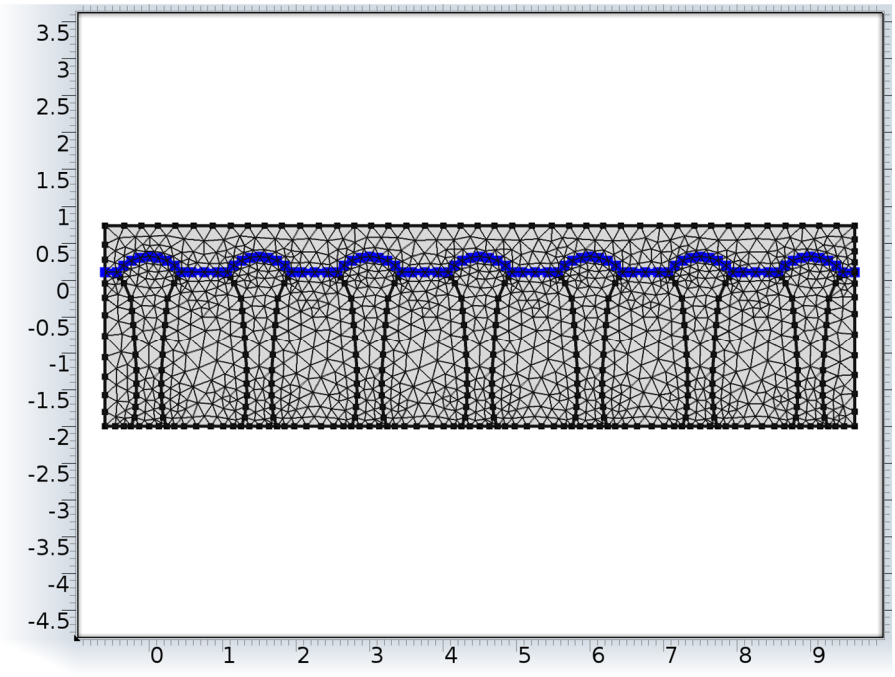

Name	Value
Maximum element size	0.377
Minimum element size	0.00128
Resolution of curvature	0.25
Maximum element growth rate	1.25
Predefined size	Finer

1x Refinement

COMSOL™

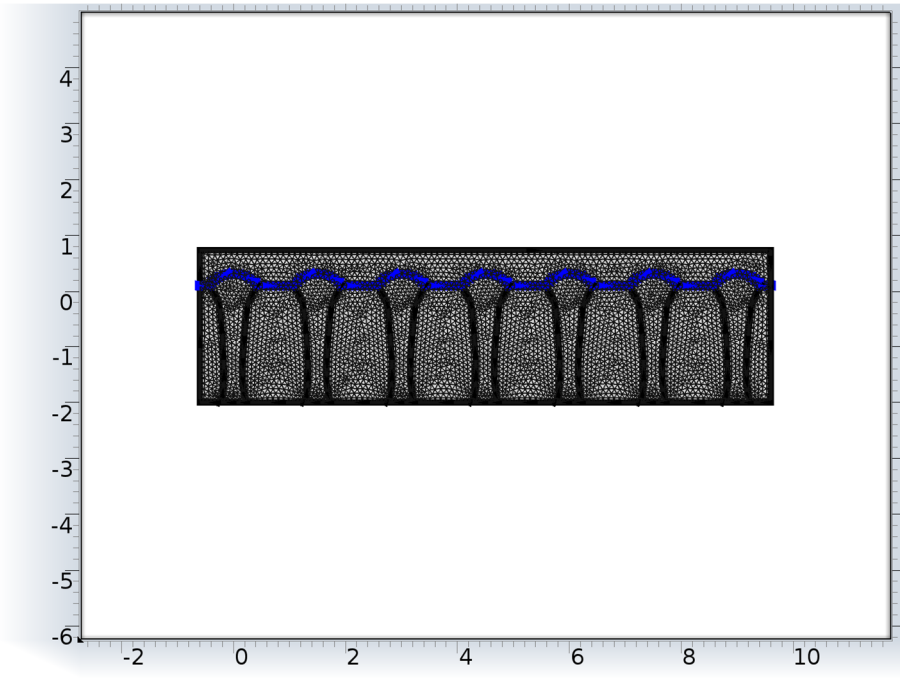

Name	Value
Maximum element size	0.102
Minimum element size	2.04E4
Resolution of curvature	0.2
Predefined size	Extremely fine

2x Refinement

COMSOL™

VITA

Naser Imran Hossain was born in the capital city of Dhaka, in the South-Asian country of Bangladesh in November, 1988. He completed primary and secondary education in the capital city. Following his father's footsteps, he went onto study engineering science in the most prestigious engineering institution of the country, Bangladesh University of Engineering and Technology (BUET) as an undergraduate student of Mechanical Engineering. He graduated within the top 20% of his class with distinctions on co-curricular and academic activities. After graduation he worked for a short while for Bangladesh University of Engineering Technology as a technical consultant for the Center for Energy Studies. Finally, he decided to attend graduate school in Louisiana State University, Baton Rouge from January, 2012. He has worked on several NASA and state funded projects during his tenure at LSU. He is a candidate for the degree of Master of Science in Mechanical Engineering to be awarded at the commencement of Summer, 2013. After completing his master's degree he hopes to join Cameron International as a design engineer from September, 2013.